Eedann McCord

Broadband Tuning the Voltage Dependence of a Sodium Channel

Eedann McCord

A dissertation
submitted in partial fulfillment of the
requirements for the degree of

Doctor of Philosophy

University of Washington
2019

Reading Committee:
William Catterall, Chair
William Zagotta
Ning Zheng

Program Authorized to Offer Degree:
Pharmacology

University of Washington

Abstract

Broadband Tuning the Voltage Dependence of a Sodium Channel

Eedann McCord

Chair of the Supervisory Committee:
Professor William A. Catterall
Pharmacology

Mammalian voltage-gated sodium channels are comprised of four homologous domains, each containing a functionally distinct voltage-sensing domain (VSD). In contrast, the bacterial sodium channel Na_VAb is a homotetramer, which enables investigation into the voltage-dependent gating mechanism without needing to account for heterogenic VSD contributions to the total signal. We endeavored to alter the properties of the VSD such that it moves in response to voltage changes over a wide range of voltages. By shifting the voltage dependence of activation in this manner, the channels can be used a means to better understand the structural features that control voltage sensing. We hypothesized that a VSD that activates only at voltages above 0 mV could be used as a tool to study the resting state with structural biology and further our understanding of the structural basis of voltage sensation. Human $Na_V1.7$ has been identified as a drug target for the treatment of a multitude of pain disorders, thus we created several chimeric channels with human $Na_V1.7$ DII residues comprising the extracellular portion of the VSD and Na_VAb residues in the S0, S4-S5 linker, and pore domain. Channels with entirely human VSDs and ones wherein the human residues extended to the level of the intracellular negative cluster did not show measurable sodium current when transiently transfected into Sf9 cells with a GFP-P2A stoichiometric fluorescent indicator. Less humanized VSDs were functional and displayed a range of voltage-dependencies of activation $V_{1/2}$ values and opening rates. Several single amino-acid substitutions whose effects were studied in other sodium and potassium channels further modified the voltage-dependence of gating in these chimeras. The combinatorial effect of these substitutions on activation was examined, and it was found that by combining mutations that produce strong effects on their own, drastic shifts in the voltage dependence of channel opening could be seen. In several cases, this did not translate to a substantial change in the voltage dependence of the gating charge movement itself, but it is possible that intermediate states were stabilized and impeded the fast movement of the voltage sensor. One combination of triple mutations, however, shifted channel opening and charge movement to more positive potentials, and this was used in combination with intersubunit disulfide crosslinking to stabilize a resting state of the voltage sensor in a cryo-EM structure at a resolution of 3.9 Å. This structure showed an 11 Å downward movement of the of the gating charges which is consistent with the sliding helix model of voltage sensor activation. The S4-S5 linker moves 9.6 Å in the gating process as it constricts around the base of the pore and sterically prevents its opening. These findings enhance our understanding of the voltage sensation process and its translation to the opening of the pore of sodium channels.

TABLE OF CONTENTS

LIST OF FIGURES

LIST OF TABLES

ACKNOWLEDGEMENTS

I was fortunate to have the support of my family, both in Texas and elsewhere in the world, throughout this journey. They have been an anchor in the storm and a limitless source of encouragement whenever I needed it. I am especially grateful for my Mom, who has always helped to find my own path without telling me where to go or how to travel.

I couldn’t have made it through this journey without my cohort in the Pharmacology department and the other graduate students there with us. I am eternally grateful to the past and present members of my lab, especially Ruth, Jin, Evanthia, Todd, and Moran, who taught me how to do everything that I needed to and more. Professors in my department and in others who have always been a source of support and guidance, Rich, Sharona, Bill, Chris, Sandy, and John, showed me how to make a difference and the power of speaking for myself. Former lab members from UT: Nick, Kelly, Jenni, Randy, Rick, Brian, Darrin and Dan, thank you so much for teaching me what to strive for. I wouldn’t be here without you.

Old friends from Texas and new friends I’ve met here have been a blessing to be around and a joy to visit. To the Tex-Pats who all made their way here over the years, you are everything that makes this world a good place. I will always be grateful for Jon, who started this journey with me. To my cat, Alcatraz, who has never done anything but give me love and laughter and cuddles, I hope you know you’re a good boy. And I wouldn’t have gotten this far with my sanity intact without Kelsey, who has been my role model, my distraction, and an amazing partner.

DEDICATION

For Wallace Herman Dahmann
January 29, 1935 – January 11, 2019

Chapter 1. INTRODUCTION

Animal life depends on electrical signaling. The swift communication of electrical signals between cells confers the ability to coordinate rapid events – allowing animals to breathe, move, and think. These signals are carried by waves of ionic current flowing in neurons, myocytes, and other excitable cells, and voltage-gated sodium channels initiate and propagate these waves (Hille, 2001).

A typical cell maintains a negative membrane potential at rest by expending energy to create ionic concentrations gradients using pumps that move sodium and potassium ions across the membrane against their respective electrochemical gradients (Caldwell et al., 1960). The hydrophobic inside of the phospholipid bilayer separates the charge difference like a capacitor, and in so doing it allows for the generation of a membrane potential which is typically in the range of -100 to -40 mV. The very small thickness of the hydrophobic center of the bilayer concentrates the force of the membrane potential into a very strong electric field that exists continuously throughout the cell and increases in strength as the distance between the external and internal aqueous environments grows smaller (Hodgkin and Huxley, 1952a, b).

When excitable membranes are chemically or mechanically stimulated, the movement of small amounts of ions across the membrane causes small transient increases (depolarizations) in this negative resting membrane potential. Voltage-gated Na^+ channels are primed to respond by very rapidly opening a highly selective pore which allows rapid Na^+ influx into the cell. In neurons, this triggers an action potential that propagates like a wave across the membrane (Armstrong and Bezanilla, 1973).

This phenomenon was first described by Hodgkin and Huxley in the squid axon, wherein they observed a large and rapid sodium conductance across the membrane upon depolarization. They theorized that the large current was controlled by the response of only a small number of charged particles which move in response to membrane voltage changes (Keynes and Rojas, 1974). The movement of the voltage-dependent gates was first directly measured in the early 1970s in the form of gating currents, which were nonlinear capacitive currents observed when permeant ions were prevented from moving through the pore (Armstrong and Bezanilla, 1977; Bezanilla and Armstrong, 1977). A fast outward movement of the gating charges is seen when the membrane is depolarized (On gating currents), and a related inward (Off) gating current was observed upon hyperpolarization of the membrane. The voltage dependence and kinetics of the gating currents were studied and found to have a distinct components that could be attributed to different voltage sensitive processes involved in conformational changes that underly sodium channel gating (Bezanilla et al., 1982; Hille, 2001).

Voltage gated sodium channels cycle through three functional states during the process of an action potential; resting (closed), open, and inactivated (closed). In the absence of depolarization, the channel is in the resting state, and once membrane depolarization occurs the channel opens and subsequently enters an inactivated state from which it cannot open again until the membrane hyperpolarizes and the channel returns to the resting state (Catterall, 1984). Once the channel enters into this inactivated state, the gating currents require greater voltage stimuli to be pulled back inward in Off measurements, which suggests that the conformation of the inactivated state of the pore stabilizes the gating charges in their outward, activated state (Noda et al., 1984).

Sodium channel alpha and beta subunits were identified by photolabeling studies using scorpion toxins which indicated that a large and a small subunit bound to the toxin (Beneski & Catterall, 1980). They were then purified from electric eels (Agnew et al 1980), skeletal muscle (Barchi, 1983), and solubilized brain tissue (Hartshorne & Catterall, 1981, 1984, Hartshorne et al, 1982) and the latter was reconstituted into phospholipid bilayers and vesicles where pharmacological and single channel electrophysiological studies verified that these purified proteins were in fact the sodium conducting channels that had been so extensively studied in their native membrane environment for decades (Talvenheimo et al, 1982; Tamkun et al. 1984; Hartshorne et al. 1985).

The theories of voltage sensor function that were formed from these observations of sodium current behavior were put into perspective when the DNA sequences encoding the channels were first identified (Tanabe et al., 1987; Timpe et al., 1988). The analysis of the cDNA sequences and those of other ion channels (Bezanilla, 2000; Payandeh et al., 2011; Takahashi et al., 1987) revealed that sodium channels share a basic overall structure with voltage gated calcium and potassium channels (Long et al., 2005), and recent advances in the field of structural biology have reinforced and expanded on that knowledge with structural models of these channels at sub-atomic resolution (Catterall, 2000; Shen et al., 2017; Stuhmer et al., 1989; Wu et al., 2016).

The channels are homo- or pseudohomotetramers, each containing six transmembrane helices. The first four helices (S1-S4) of each subunit comprise the voltage sensing domain (VSD), while the fifth and sixth (S5-S6) transmembrane helices from all four subunits come together to form the central pore with each VSD connected to the pore via an amphipathic helix called the S4-S5 linker (Papazian et al., 1995). The S4 segment contains an array of positively charged residues flanked by hydrophobic ones in a pattern wherein each arginine and/or lysine is spaced exactly three amino acids from the next, roughly one helical turn apart. Mutagenesis studies confirmed that these charged residues on the S4 enable the VSD to sense fluctuations in membrane potential and respond by opening the pore (Aggarwal and MacKinnon, 1996; Catterall, 1986; Guy and Seetharamulu, 1986).

Three main models have been proposed to explain the experimental data it terms of specific structural changes that occur during VSD activation: the sliding helix/helical screw model, the transporter model, and the paddle model.

The first model suggests that outward movement of the S4 segment through the membrane in response to voltage is the direct result of membrane depolarization and the source of gating currents (Campos et al., 2007b; Ramírez-SanJuan et al., 2013). This model suggests that at the resting membrane potential, the positively charged S4 segment is pulled inward by the electrostatic force of the membrane electric field. When the S4 segment is pushed outward in response to depolarization, the positive S4 gating charges interact sequentially with negatively charged residues on the S1-S3, termed the intracellular and extracellular negative clusters (INC and ENC, respectively), as they pass through a hydrophobic constriction site (HCS) that separates the aqueous environments and focuses the membrane electric field (Fig. 1.1; (Tao et al., 2010)). This area has also been referred to as the "hydrophobic plug" (Stuhmer et al., 1989) and the "gating charge transfer center" (Cestèle et al., 1998).

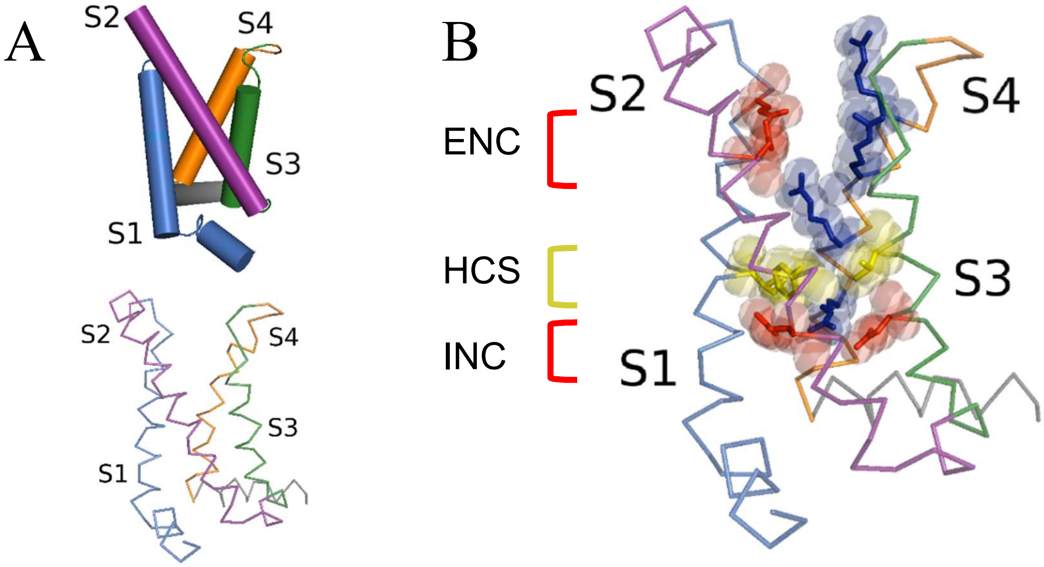

Figure 1.1. Anatomy of an activated voltage-sensing domain.

A) E Cylindrical (top) and ribbon (bottom) diagram of the 4 transmembrane helices of the VSD. Each transmembrane segment S1-S4 is a different color: S1 blue; S2 purple; S3 green; S4 orange.

B) A view of the VSD with functionally important residues shown as sticks with spherical atomic shells. The intracellular and extracellular negative cluster residues are indicated in red, the hydrophobic constriction site in yellow, and the gating charges in blue.

Many experimental results support the sliding helix/helical screw model of voltage sensation. The effects of neutralization of S4 arginines caused a decrease in the total charge moved over wide stretches of the S4, establishing that these residues are the gating charges. (Rogers et al., 1996). Gating modifier toxins that trap the activated and resting states of the VSD illustrate that the S4 is in a transmembrane orientation in both the resting and activated states (Yang et al., 1996, 1997). S4 cysteine scanning and modification studies showed that gating charges move from and intracellularly accessible to an extracellularly accessible position upon depolarization and vice versa (DeCaen et al., 2009; Yarov-Yarovoy et al., 2012). Lastly, disulfide locking experiments demonstrated that gating charges interact with the INC and ENC positions during the path of S4 movement (Bezanilla, 2000; Papazian et al., 1995).

The second and third models do not have as much support from the findings of the field. The transporter model suggests that the S4 need not move very far to a rearrangement of the vestibules such that the membrane electric field shifts from one side of the voltage sensor to the other (Jiang et al., 2003a). Structural studies have shown that the activated VSD has inner and outer aqueous vestibules which concentrate the membrane electric field across a narrow band of hydrophobic proteins (the HCS), a requirement for the model to function (Jiang et al., 2003b).

The paddle theory arises from the first crystal structure of a voltage-gated ion channel, for which an antibody FAB was used to stabilize the KvAP potassium channel in detergent. In this model, the outer portion of the S3 and the S3-S4 linker associate tightly with the S4 and moved through the membrane in a hinge fashion (Lee et al., 2005). Further labeling studies aimed to justify the findings (Payandeh and Minor, 2015), but eventually a second structure of the KvAP in the presence of lipid showed that the VSD of the initial structure was likely contorted by the FAB without the support of a lipid bilayer (Catterall et al., 2017).

The mechanism of electromechanical coupling of the VSD to the pore is the basis for all electrical signaling in cells, but high-resolution structural information of different stages of the voltage sensor activation sequence has been difficult to achieve. This is due to the nature of the voltage sensors themselves and the limitations of current structural biology techniques. Without modification, VSDs will activate at 0 mV, the potential that channels experience when purified, and the energetics will not favor a stabilization of a resting or intermediate state of the VSD (Payandeh et al., 2011; Shen et al., 2017).

Initial structures of sodium channels focused on the simple prokaryotic channels that more closely resemble an ancestor of sodium and calcium channels than the complex eukaryotic channels that have evolved (Chanda and Bezanilla, 2002). Eukaryotic sodium channels have four homologous domains that are connected to each other by long disordered intracellular loops, but the basic tetrameric structure is maintained (Goldschen-Ohm et al., 2013). The number and identity of the gating charges on the S4 segment of each subunit of these channels is different from the next (Fig 1.2). In eukaryotic sodium channels, the DI S4 has the least number of gating charges (4), while the DIV S4 has twice that amount (8) (Fig 1.2).

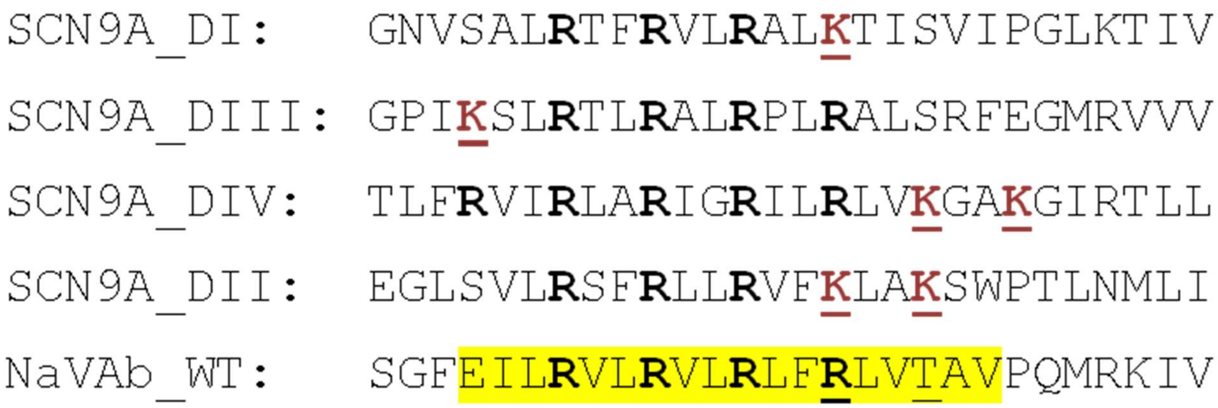

SCN9A_DI: GNVSAL**R**TF**R**VL**R**AL**K**TISVIPGLKTIV
SCN9A_DIII: GPI**K**SL**R**TL**R**AL**R**PL**R**ALSRFEGMRVVV
SCN9A_DIV: TLF**R**VI**R**LA**R**IG**R**IL**R**LV**K**GA**K**GIRTLL
SCN9A_DII: EGLSVL**R**SF**R**LL**R**VF**K**LA**K**SWPTLNMLI
NaVAb_WT: SGFEIL**R**VL**R**VL**R**LF**R**LVTAVPQMRKIV

Figure 1.2 Sequence alignment of the S4 of Na$_V$Ab and D1-IV of Na$_V$1.7
Charged residues are shown in color, arginine in red and lysine in green. The S4 alpha helical extent of the activated VSD is highlighted in yellow for each subunit, based on the structures 4EKW (Payandeh et al., 2011). Gating charge residues on the S4 are shown in bold.

Because of the diversity of S4 gating charge makeups, the four voltage sensors do not all respond to voltage in the same way. Gating charge and fluorescence signals of rat Na$_V$1.4 show the gating charge movement of the first three VSDs is fast, and the translocation of one gating charge in each of these three S4 segments is sufficient to open the pore of the channel (Chanda and Bezanilla, 2002). The DIV S4 movement is slower, but its movement is necessary for fast inactivation of the channel to occur (Payandeh and Minor, 2015). The fast inactivation gate cannot move to close the pore until DIV is activated, providing a temporal window in which current can flow through the open channel before it inactivates. A further difference between the VSDs is that the DI and DII S4 segments move at more depolarized voltages than DIII and DIV, which leads to a channel that is primed to quickly activate (when DIII moves) and subsequently inactivate (Gamal El-Din et al., 2013).

Bacterial sodium channels are homotetrameric, and they do not contain a fast inactivation gate. All four voltage sensors are identical, and thus they all respond to voltage the same way upon depolarization (Payandeh et al., 2012). After quickly opening in response to depolarization, the channel undergoes a type of inactivation that results from conformational changes near the pore instead. It is thought that there are two inactivated states of these channels. The first occurs immediately after the channel has opened and can be visualized as the decay of the current amplitude after it reaches peak (McCormack et al., 2013). This type of inactivation can be recovered from quickly after hyperpolarization. The second type takes longer to develop and for complete recovery to occur (Palovcak et al., 2014).

Since a fast-inactivated conformation similar to eukaryotic sodium channels does not exist for bacterial channels, the information we glean from structures of the activated VSD and inactivated pore may have limits in usefulness for the purposes of structure-based drug design of highly specific human sodium channel modifiers. Without a doubt, structures of alternative VSD conformations will shed much light onto our understanding of the biophysics of electromechanical coupling, but the potential for additional applications of the structural information to human pharmacological studies motivated our initial approach to achieving this goal.

To produce a high-resolution structure of an intact sodium channel in the resting state, we created chimeric human-bacterial channels containing human residues on the extracellular surface of the VSD, and we used mutagenesis to impair VSD movement at depolarized membrane potentials in these chimeras as well the fully bacterial sodium channel NavAb.

While many mutations have been studied that alter voltage-dependent properties of sodium channels, it wasn't yet known how much one could shift the voltage dependence of gating in a bacterial sodium channel that has evolved to function at very negative membrane potentials. In this study, we devised a mechanism to control the voltage dependence with combinations of point mutations previously found to alter voltage dependence on their own in the *Shaker B* potassium channel, NaChBac bacterial sodium channel, and a rat neuronal sodium channel. Combinations of these mutations were then used to maximize the positive shifts of the voltage dependence of activation and to probe the limits of such positive shifts. The additive effects of these combinations were used to identify intersubunit interactions that occur in the resting state which could create a disulfide bond to stabilize it further in soluble protein for structural determination. The outcome was successful broadband tuning of the voltage sensitivity of the voltage sensors of a bacterial and a mammalian sodium channel nearly 250 mV. This dramatic positive shift of the voltage dependence of a sodium channel was unprecedented and allowed us to stabilize the resting state of the sodium channel for structural studies.

Chapter 2. HUMAN NAV1.7 DOMAIN II CHIMERAS

2.1 BACKGROUND

Over millennia, the diversity of eukaryotic voltage gated ion channels has evolved alongside other proteins and metabolites in the environment which alter their function. Plants produce alkaloids that activate several sodium channel subtypes, the pufferfish secretes a small molecule which blocks many of them, and the binding sites for these drugs are located in parts of the protein that are structurally similar in many subtypes of sodium channels (George, 2005). These conserved areas are generally critical for the proper functioning of the basic elements of the channel (Palovcak et al., 2014). Voltage-gated sodium channels have only one pore, and as such, any mutation in that region carries with it a high likelihood of causing complete loss or gain of function. Many diseases are caused by such mutations in ion channels, and often they are fatal or confer a significant handicap to the reproductive success of the organism (Palovcak et al., 2014).

The most conserved residues of prokaryotic bacterial channels are located on the transmembrane segments of the protein, including the VSD and the pore. (Figure 2.1, green). These are functionally critical areas of the protein and the residues are more likely to contribute to necessary functions of the channel (Trimmer and Agnew, 1989). The residues on the external faces of the protein, however, have low sequence conservation scores overall (Fig 2.1, orange), including the extracellular face of the VSD. Since variations in these areas are common, they may contribute to the unique properties seen across individual voltage sensors.

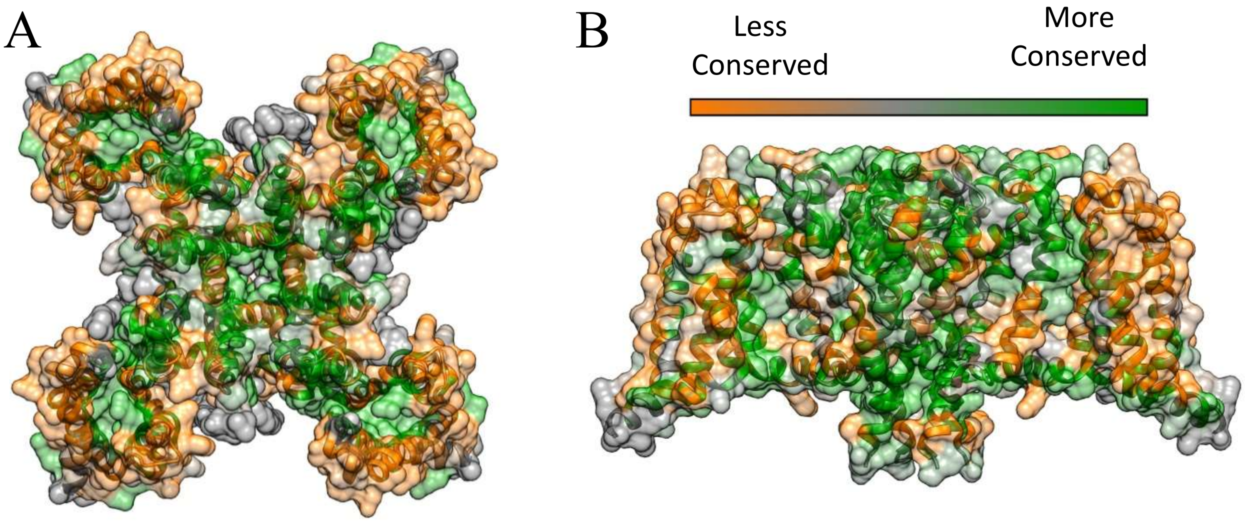

Figure 2.1 Sequence conservation of prokaryotic channels mapped onto NaVAb.
Colors represent the conservation score of each residue and range from least-conserved (orange) to most-conserved (green). The ribbon model and surface reconstruction are shown (A) from the extracellular surface and (B) from the side, parallel to the membrane. In (B), the two VSDs on the z axis were removed for clarity. Conservation scores were calculated in UCSF Chimera using AL2CO (Pei et al, 2001) independent counts as the frequency estimation method. The conservation measure was variance-based using an averaging window of 1 and a gap-fraction of 0.5. Delineations from red to gray to blue were placed approximately at ¼, ½, and ¾ of the total residue count along the conservation measure histogram. Sequences were acquired by performing a pblast search confided to the Prokaryota taxa, and sequences were aligned with Clustal Omega.

The redundancy of four VSDs in eukaryotic sodium channels may have initially permitted increases in variation at positions that are not crucial to overall function (Zakon, 2012). As random mutations occurred and accumulated, several subtypes of sodium channels emerged, each with slightly different voltage-dependent properties, cellular localization, and ability to be modified by signaling cascades within the cell (Olivera et al., 1991; Zakon, 2012). Metabolites and venoms produced for defensive or predatory purposes often alter the function of ion channels, and indeed often evolved alongside the channel to maintain its function as mutations in the channel accumulated (Safo et al., 2000; Xu et al., 2019).

There is no greater example of this than venom toxins produced by predatory spiders, scorpions, and cone snails. In the venom of any one of these organisms, thousands of small, tightly folded peptide toxins can be found. Many of these peptides, when purified, are shown to bind to voltage-gated ion channels in a highly specific manner – often to only one of four VSDs in only a few subtypes of channels – and the association can have extremely high affinity (Campos et al., 2007a; Catterall et al., 2007). There are several examples of venom toxins which modify the voltage sensitivity of the channel by preventing the voltage-dependent movement of the voltage sensing S4 itself. These are called gating modifier toxins, and they tend to bind and stabilize a specific structural state of the VSD that they target (Cestèle et al., 1998).

Some, like beta-scorpion toxin, bind and stabilize the activated state of the VSD. This toxin binds to the VSD upon depolarization and increases the energetic barrier of voltage sensor movement by stabilizing an intermediate state in the VSD activation pathway(Cestèle et al., 1998). A larger amount of force is then needed to return the S4 to the resting state, and the normal hyperpolarized membrane potential of the cell is not sufficient to bring it back to rest in the same amount of time, which shifts the voltage-dependence or opening to more negative potential and alters the equilibrium to stabilize an inactivated state at the resting potential (Sokolov et al., 2008). Conversely, a peptide from the Chinese bird spider, ProToxin-II, binds to and stabilizes the resting state of domain II VSD of Na_V 1.7. and 1.2 with lower affinity. The channel is unable to open without the activation of the DII VSD, and the energetic barrier conferred by the binding of this toxin is sufficient to inhibit the channel’s activation in response to all but the strongest depolarizations (Schmalhofer et al., 2008) The affinity for the Na_V1.7 is 100 times higher (0.3 nM) than any other sodium channel isoform, and the toxin preferentially binds the DII VSD of that channel, making it one of the most potent and selective sodium channel inhibitors ever studied (Ahuja et al., 2015).

In diseases where aberrant Na$^+$ current causes a pathological increase in electrical excitability such as epilepsy, cardiac arrhythmia, and peripheral pain disorders, effective treatment aims to decrease the excitability of the nerve or muscle cells. As sodium channels contribute to the upstroke of action potentials, they are logical potential drug targets for these disorders, but all sodium channel inhibitors currently prescribed bind to and occlude the pore, often in a state-dependent manner, with the overall effect being a decreased sodium conductance due to stabilization of an inactivated state of the channel as the primary mechanism (Emery et al., 2016). Because the pore has a high level of sequence conservation, these drugs typically do not have strong subtype selectivity between the 9 sodium isoforms expressed in various tissues throughout the body, which can lead to serious complications from off target effects (Herzog et al., 2003).

NaV1.7 was identified as a contributor to chronic pain disorders when a gain-of-function mutation in the gene was found to cause an extreme pain syndrome called primary erythermalgia (Cummins et al., 2004; Yang et al., 2004). A few months later it was reported that a conditional knockout mouse that lacked NaV1.7 in peripheral sensory neurons had drastically reduced inflammatory pain responses (Nassar et al., 2004). An autosomal recessive disorder that resulted in the complete inability to feel pain in humans was then shown to be caused by a loss-of-function mutation in NaV1.7 (Cox et al., 2006). With this mounting evidence, it became clear that the intrinsic activity of this channel was tightly linked to the sensation of pain.

Three human sodium channel isoforms are preferentially expressed in peripheral pain fibers: NaV1.7, NaV1.8, and NaV1.9, and they have been implicated as modulators of pain sensation by many loss-of-function and gain-of-function mutations that eliminate or enhance nociception in patients, respectively. Nav1.7 produces rapidly activating and inactivating currents, and it progresses to closed-state inactivation more slowly than other sodium channels (Tang et al., 2015). This allows the channel to respond to small and repetitive depolarizations at voltage ranges that are close to the resting potentials of the pain fibers. For these reasons Nav1.7 channels can behave as an amplifier of subtle depolarizations and subsequently escalate the depolarization of the membrane towards the activation threshold of Nav1.8 channels, which are the main charge-carrying component of nociceptive action potentials (Rajamani et al., 2017). Several studies of gating properties in syndromes associated with mutations of Na$_V$1.7 have shown that alterations in these very subtle voltage-dependent changes in membrane potential can have monumental effects on the experience of pain sensation, with gain of function mutations causing a wide array of neuropathic pain disorders which are often unresponsive to standard analgesics (Rajamani et al., 2017). For these reasons, Na$_V$1.7 has been a promising drug target for new pain medications, and information regarding the specific structural changes that occur in the VSD during gating could aid in the development of non-addictive, safe, and selective alternatives for chronic pain.

2.2 Construction and Analysis of Na$_V$1.7/Na$_V$Ab Chimeras

In order to better understand these structural changes, we created a chimera of the homotetrameric bacterial sodium channel Na$_V$Ab which contained the extracellular residues of the human Nav 1.7 DII VSD in place of the bacterial residues. This served to recreate the binding site of ProTx-II on all four subunits of the channel (Rajamani et al., 2017), and we hoped this would facilitate structural determination of the resting state via co-crystallization of the chimera and the toxin. We tested several constructs containing varying degrees of humanization of the residues, each of which had distinct voltage-dependent properties.

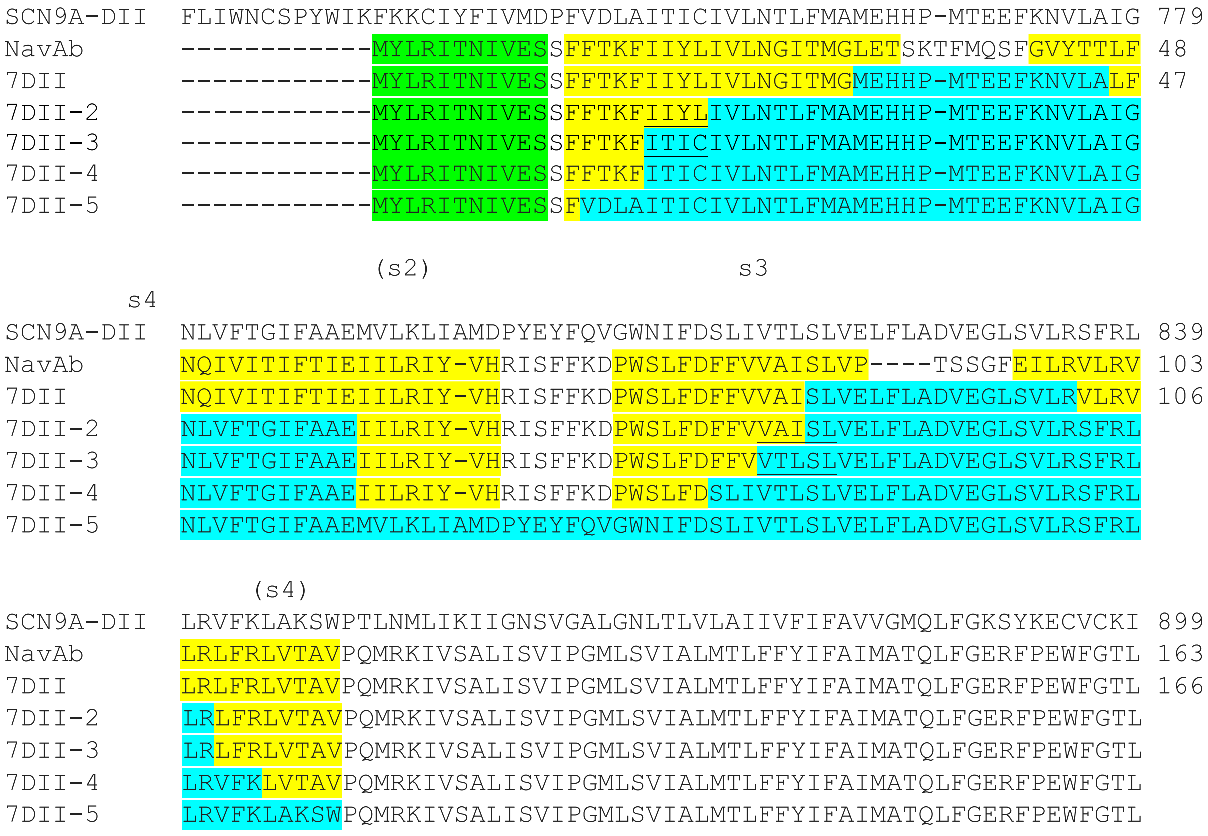

```
SCN9A-DII  FLIWNCSPYWIKFKKCIYFIVMDPFVDLAITICIVLNTLFMAMEHHP-MTEEFKNVLAIG 779
NavAb      -------------MYLRITNIVESSFFTKFIIYLIVLNGITMGLETSKTFMQSFGVYTTLF 48
7DII       -------------MYLRITNIVESSFFTKFIIYLIVLNGITMGMEHHP-MTEEFKNVLALF 47
7DII-2     -------------MYLRITNIVESSFFTKFIIYLIVLNTLFMAMEHHP-MTEEFKNVLAIG
7DII-3     -------------MYLRITNIVESSFFTKFITICIVLNTLFMAMEHHP-MTEEFKNVLAIG
7DII-4     -------------MYLRITNIVESSFFTKFITICIVLNTLFMAMEHHP-MTEEFKNVLAIG
7DII-5     -------------MYLRITNIVESSFVDLAITICIVLNTLFMAMEHHP-MTEEFKNVLAIG

                       (s2)                   s3
        s4
SCN9A-DII  NLVFTGIFAAEMVLKLIAMDPYEYFQVGWNIFDSLIVTLSLVELFLADVEGLSVLRSFRL 839
NavAb      NQIVITIFTIEIILRIY-VHRISFFKDPWSLFDFFVVAISLVP----TSSGFEILRVLRV 103
7DII       NQIVITIFTIEIILRIY-VHRISFFKDPWSLFDFFVVAISLVELFLADVEGLSVLRVLRV 106
7DII-2     NLVFTGIFAAEIILRIY-VHRISFFKDPWSLFDFFVVAISLVELFLADVEGLSVLRSFRL
7DII-3     NLVFTGIFAAEIILRIY-VHRISFFKDPWSLFDFFVVTLSLVELFLADVEGLSVLRSFRL
7DII-4     NLVFTGIFAAEIILRIY-VHRISFFKDPWSLFDSLIVTLSLVELFLADVEGLSVLRSFRL
7DII-5     NLVFTGIFAAEMVLKLIAMDPYEYFQVGWNIFDSLIVTLSLVELFLADVEGLSVLRSFRL

               (s4)
SCN9A-DII  LRVFKLAKSWPTLNMLIKIIGNSVGALGNLTLVLAIIVFIFAVVGMQLFGKSYKECVCKI 899
NavAb      LRLFRLVTAVPQMRKIVSALISVIPGMLSVIALMTLFFYIFAIMATQLFGERFPEWFGTL 163
7DII       LRLFRLVTAVPQMRKIVSALISVIPGMLSVIALMTLFFYIFAIMATQLFGERFPEWFGTL 166
7DII-2     LRLFRLVTAVPQMRKIVSALISVIPGMLSVIALMTLFFYIFAIMATQLFGERFPEWFGTL
7DII-3     LRLFRLVTAVPQMRKIVSALISVIPGMLSVIALMTLFFYIFAIMATQLFGERFPEWFGTL
7DII-4     LRVFKLVTAVPQMRKIVSALISVIPGMLSVIALMTLFFYIFAIMATQLFGERFPEWFGTL
7DII-5     LRVFKLAKSWPQMRKIVSALISVIPGMLSVIALMTLFFYIFAIMATQLFGERFPEWFGTL
```

Figure 2.2 Sequence alignment of $hNa_V1.7$-DII, Na_VAb WT, and the five chimeras. Yellow highlighting indicated helices S1-S4 as labeled. Blue highlighting indicates human residues transplanted onto Na_VAb to create the named chimeras. 7DII-2 and -3 indicate the potential sequence identity of the chimera used in Rajmani et al. The wording of Rajamani et al was self-conflicting, and the residues in question are underlined. Given the published alignments, it is unclear if the construct studied contained the most human residues possible, the least, or somewhere in between.

The first chimera we created, called 7DII, contained the extracellular residues of the human $Na_V1.7$ DII VSD, starting roughly one helical turn down on each helix (Figure 2.3 B). This shortened the S1-S2 liker by one residue and lengthened the S3-S4 linker by 4 residues, resulting in a net gain of 3 residues for the channel. All mutations characterized in this project were first studied in this chimera construct.

The primary means of studying the voltage dependence of activation in a sodium channel is to measure the peak current amplitude in response to a voltage stimulation at a range of voltages. Using whole-cell voltage clamp, cells expressing the channels are held at a negative voltage and then the membrane potential is briefly increased and returned to the holding potential, and the current flowing through open channels during this voltage pulse is recorded. This is repeated at more and more positive potentials, and the resultant peak current amplitudes are plotted as a function of the stimulation voltage. The effect of the driving force of sodium on the amplitudes of these currents varies with voltage, and to normalize for this, the current values are divided by the driving force for each voltage, which is equivalent to the sodium equilibrium potential subtracted from the voltage of each pulse. This gives a measure of sodium conductance rather than current, and when normalized to values between 0 and 1, the conductance vs voltage (G/V) curves can be easily compared by describing the voltage where the curve is at a relative conductance of 0.5, which indicates that half of the channels are open. When the curve is fit with a 2 state Boltzmann distribution, this value (called the $V_{1/2}$) is calculated as well as a slope factor, k (mV), which equals 25.6 divided by the apparent number of gating charges moved in the transition, z_{app}, at room temperature. As the G/V curve becomes steeper, more charges are involved in the transition. These values describe how voltage influences channel opening (Hille, 2001).

In channels that do not inactivate after opening and have slow deactivation rates, the effect of driving force can be eliminated by measuring the instantaneous current (called a tail current) that occurs when the membrane returns to rest (or another voltage). The resulting current amplitude values can be plotted as a function of the test voltage applied before the tail and fit with a Boltzmann as above. Sodium channels display inactivation during the stimulation pulse resulting in a channels transitioning the inactivated state shortly after opening, so any attempt to measure instantaneous current would not accurately represent the percentage of channels that had opened in response to the pulse since they would be inactivated at the time of tail current measurement. When current is flowing at the end of a test pulse and the membrane is hyperpolarized, a tail current with amplitude equal to the conductance multiplied by the driving force of the new membrane potential should be seen, however in channels with very fast deactivation rates (transition from open to close), the current may be so short lived that it cannot be measured due to the limitations of the equipment. This indicates a stable closed or resting state of the channel, and the magnitude of the tail currents compared to the residual current is a rough indicator of the favorability of the transition from open to rest at that voltage (Hoshi et al., 1994).

When examining the current families produced by the voltage protocol that generates the G/V curve, we can also learn about the kinetics of channel opening. A single exponential can be fit to the onset of the current, and from that fit we get the time constant of the transition. The inverse of this time constant is the rate (expressed in events per second), which is a helpful tool for comparing how fast the channels respond as a group to the voltage change. Smaller rates indicate the opening transition of the channel is not as temporally coupled to voltage dependent changes that cause the final transition to opening (Almog et al., 2018; Islas and Sigworth, 1999; Schoppa and Sigworth, 1998). The y-intercept of this exponential fit is the delay to current onset (delay, measured in seconds), which gives a clue as to how many closed states the channel must transition through before opening, where a very short delay is indicative of fewer transition states between rest and open (Cole and Moore, 1960).

There is also a way to measure the movement of the S4 gating charges themselves, by recording gating currents and constructing a charge-voltage (Q/V) relationship. To measure gating currents, all permeant cations must be removed from the recording solutions and replaced with a large positively charged molecule that cannot fit through the pore (e.g. N-methyl-D-glucamine, NMDG+). When the density of channels in the cell membrane is very high, it is possible to then measure the movement of the gating charges as they move through the membrane electric field by integrating the current response to voltage and subtracting the linear capacitance (Armstrong and Bezanilla, 1977). We can then plot the value (in coulombs) as a function of voltage and normalize the values from 0 to 1. As with G/V curves, the $V_{1/2}$ and k parameters can be calculated with a fit of the curve to a two-state Boltzmann (Armstrong, 1981; Sigworth, 1995).

7DII had voltage-dependent properties that are slightly more negatively shifted than Na_VAb WT, with a $V_{1/2}$ of -118 mV (Figure 2.3). The use-dependent and “late slow” inactivation observed in Na_VAb WT were still present in 7DII and possibly more pronounced, as evidenced by the inability of the channel to recover from inactivation even after several minutes at -180 mV (data not shown). Four additional chimeras were subsequently made which contained a larger portion of human residues, and their voltage-dependent properties were studied. The two most humanized constructs, wherein human residues extend to the level of the INC or encompass the full S1-S4 of the VSD, were not able to pass a sodium current at the measured voltages, and they are likely nonfunctional.

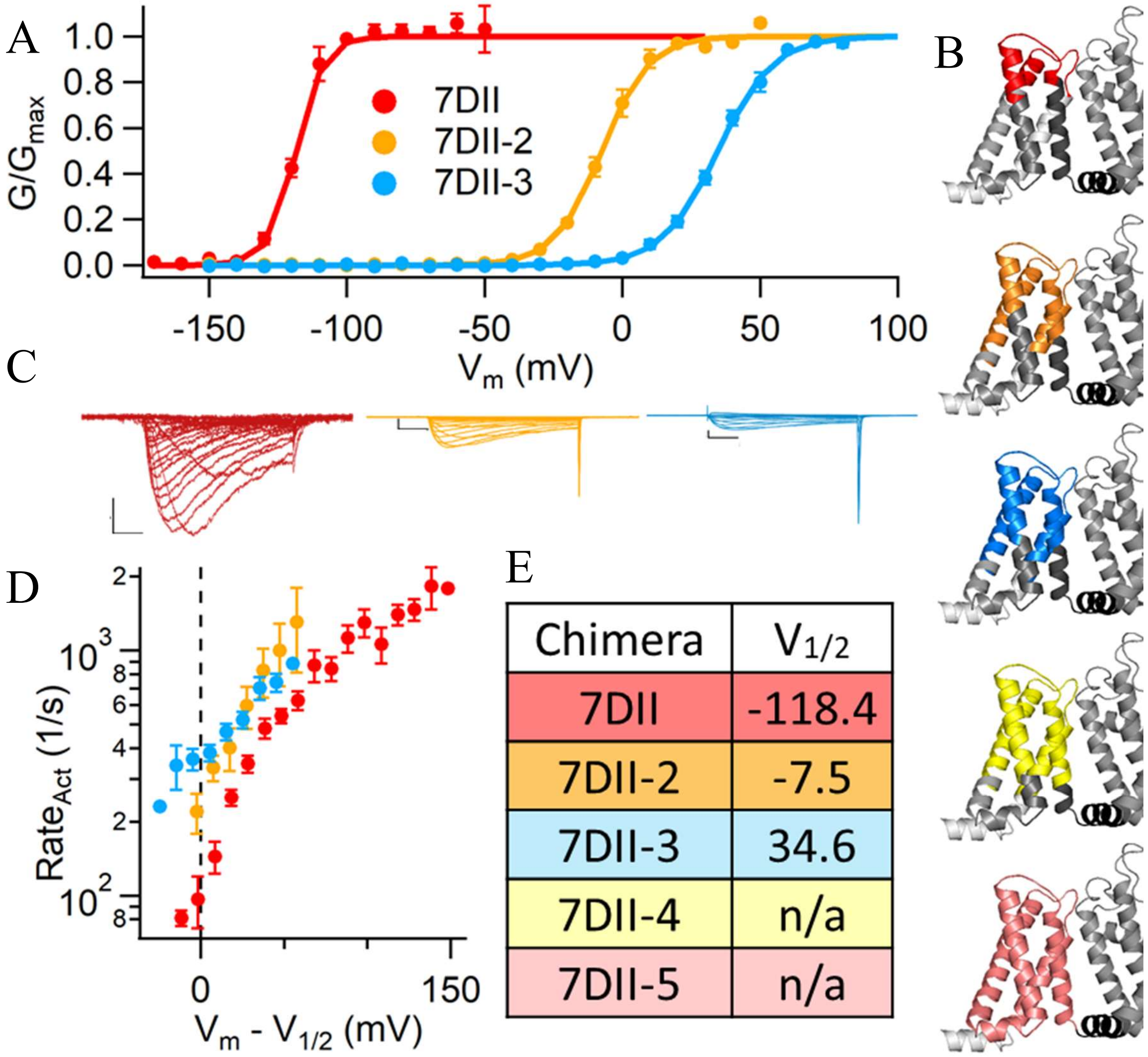

Chimera	$V_{1/2}$
7DII	-118.4
7DII-2	-7.5
7DII-3	34.6
7DII-4	n/a
7DII-5	n/a

Figure 2.3 Chimeras and Functional Summary.

A) Conductance-voltage relationships of three chimeras containing increasing numbers of human Na$_V$1.7 DII residues as the $V_{1/2}$ shifts to more positive values. B) A Homology Model (Swiss-Model, 5X0M template (Shen et al., 2017), Domain II) was made to highlight the extent of humanization of five chimeric human-bacterial sodium channels created by replacing Na$_V$Ab residues with those of human Na$_V$1.7 DII. The S1-S4 segments are colored from light to dark gray, with the S4-S5 linker in black. The colored portion indicates human residues, while native Na$_V$Ab residues are in varying shades of gray. The colors correspond to the different chimeric channels. The channels are arranged in order from least to most humanized. Red: 7DII, orange: 7DII-2, Blue: 7DII-3, Yellow: 7DII-4, and Pink: 7DII-5. C) Current families of the three chimeras, with corresponding colors and positioning to A. D) The rate of activation (inverse tau) of the rising phase of the exponential growth of the current. A single exponential (1+exp(-(x-x_0)/tau)) was fit to the trace, and the tau value was divided by one to get the rate of transition. The x-values are normalized to the $V_{1/2}$ of the activation curve of the specific construct to allow for comparison across a wide range of voltage-dependencies. All values are mean +- sem. E) A table summarizing the chimera effects. 7DII-4 and 7DII-5 did not conduct current that could be classified as I_{Na}, as no inward instantaneous current was observed at membrane potentials below the reversal potential of sodium. The colors in the table correspond to the structural models. All calibrators represent 1 nA by 10 us.

These more humanized chimeras displayed enormous positive shifts in the $V_{1/2}$ of activation compared to 7DII (Figure 2.3.A). For 7DII-2, the activation voltage shifted 101 mV to a $V_{1/2}$ of -7 mV, and 7DII-3 produced a further *positive* shift of 42 mV to a final $V_{1/2}$ of +35 mV. This additional shift was due to human residues substituted for Na_VAb residues over one helical turn of the S1 and S3. If the effect of additional human substitutions was additive, it was not measurable. Further humanized chimeras were not functional (Figure 2.3.E). 7DII-2 and 7DII-3 both had faster rates of opening than the less humanized WT. While no confirmed sodium current was measured for the last two chimera constructs, the possibility that this was due to insufficiently positive voltage of activation cannot be ruled out. It is clear that the effect of replacing bacterial residues with human ones can have large effects on the voltage dependent properties, even when all necessary components for gating are still present.

Table 1 - Activation parameters of human Na_V1.7 – Na_VAb VSD chimeras

Chimera	Act $V_{1/2}$	k	z_{app}	n
7DII	-118.43 ± 0.89	5.01 ± 0.35	5.13 ± 0.39	7
7DII-2	34.59 ± 1.36	10 ± 0.46	2.51 ± 0.12	6
7DII-3	-7.52 ± 1.72	8.46 ± 0.61	2.95 ± 0.21	2

The half maximal voltage, slope factor, and apparent charge movement. Mean ± SEM

2.3 COMPARISON WITH OTHER NA$_V$1.7/NA$_V$AB CHIMERAS

As is often the case during long projects, since the start of this endeavor, other labs have reported the results of similar experiments as my work was in progress. In 2017, Rajamani et. al. published a study in Molecular Pharmacology wherein they created a chimeric human-bacterial sodium channel which binds to ProToxin-II and HuwenToxin-IV with similar affinities to those reported in the intact human channel (Rajamani et al., 2017). Electrophysiological studies of this chimeric channel show that the voltage-dependence of activation shifts to more positive potentials in the presence of low concentrations of ProToxin-II, as has been shown for Na$_V$1.7 and 1.2 (Schmalhofer, 2008; Sokolov, 2008), indicating that ProToxin-II is acting as a gating modifier and stabilizing the resting state for this chimeric channel as well. Multiple preparations and procedures were used to show the channel retains the high affinity binding site in its purified form (at 0 mV).

We wanted to replicate these measurements of voltage-dependent activation (Figure 2.3.A), which necessitated generating four new chimeras, of which two are discussed here (7DII-2 and 7DII-3), as the reference sequence was unclear (Clairfeuille et al., 2019; methods vs S1).They differed by one helical turn on S1 and S3, and after electrophysiological characterization, 7DII-3 appeared to be the construct that they used. The $V_{1/2}$ reported in the manuscript was +51.8 mV, which is more similar to the 7DII-3 $V_{1/2}$ of +34.6 mV than the 7DII-2 $V_{1/2}$ of -7.5 mV (Table 1). They describe the channel as non-inactivating, which justified their use of tail currents to generate the G/V curve for the chimera, although the data do not support that assumption.

They likely used the tail current method rather than plot the peak current amplitude and adjust for driving force because their recording solutions placed the sodium reversal potential around +45 mV, which would make conductance calculations noisier in crucial areas of the activation curve. A method for remedying this issue is utilized in this thesis project, where NMDG-

Cl is substituted for NaCl in the recording solutions at concentrations necessary to move the equilibrium potential without altering the overall concentration of cations in the solutions. Additionally, the amplitude of the tail currents combined with the series resistance compensation that they used could produce voltage errors of up to 75 mV based on their representative current family, which is likely the reason for the discrepancy between the $V_{1/2}$ of activation in the two projects. See Figure 4.8 for a summary of how 7DII-3 was used in the current work.

A study published earlier this year used an even more humanized chimeric channel, which was nearly identical to the nonfunctional 7DII-4 described above, to obtain cryo-EM structures of ProTx-II bound to the activated and deactivated VSD of this chimera (Payandeh et al., 2012). The paper only included electrophysiology data from the full-length human $Na_V1.7$, not the chimeric channel for which the structure was determined, because the chimera was nonfunctional like 7DII-4. Compared to the activated state with only one gating charge (R4) below the HCS, the deactivated state had two gating charges (R3 and R4) clearly below the HCS, with R2 forming a salt bridge with an extracellular negative cluster residue in spite of its close proximity to the HCS phenylalanine on S2. It is predicted that the resting state of this channel should have three gating charges (R2-R4) clearly below the HCS. A similar finding was reported for alpha scorpion toxin binding to domain IV of a chimeric cockroach sodium channel (Gamal El-Din et al., 2017). The DIV S4 contains several more gating charges than the other domains, and the difference between the toxin bound and unbound structures showed the complete movement of two charges through the HCS. The channel used for structural determination was also nonfunctional, however, and it could not be experimentally determined whether these two charges represented the full translocation of the S4 that occurs during voltage-induced VSD activation or inactivation. These findings together suggest that these gating modifier toxins may stabilize an intermediate state of the VSD activation pathway, described as a deactivated state in both studies. In spite of these impressive advances, an unambiguous resting state structure confirmed by electrophysiological recordings still remained to be determined.

Chapter 3. SINGLE RESIDUE SUBSTITUTIONS

3.1 BACKGROUND

Unlike eukaryotic sodium channels, Na_VAb has been shown to possess no Hodgkin-Huxley type fast inactivation but three distinct kinetic phases of slow inactivation: two that are easily reversible by hyperpolarization, and one "late phase" that reverses very slowly and is caused by repetitive pulses which open the channels (Blanchet and Chahine, 2007; Gamal El-Din et al., 2013; Pavlov et al., 2005). Each subsequent pulse results in fewer channels available to open in the next pulse. This current rundown makes stable recordings of various voltage-dependent properties of the channels practically impossible. As more depolarizations during experimental protocols cause a higher proportion of channels to inactivate, less current is possible in subsequent tests of that cell. Even successive sweeps in a single experiment experience this effect, and thus the effect of voltage on channel opening is artificially augmented when peak current is plotted as a function of voltage. The addition of the well-studied N49K (N48K in the chimera), had the predicted effect on voltage-dependence of activation as it positively shifted the $V_{1/2}$ by the same magnitude of voltage as in Na_VAb and NaChBac (Lacroix et al., 2014; Zagotta and Aldrich, 1990), and it eliminated late slow inactivation.

This led us to ask whether other residues which alter the voltage-dependence of activation could also be substituted onto the chimera and achieve similar results. We endeavored to use point mutations with the goal of altering the energetic landscape of the protein at zero mV, which could stabilize a different state of the voltage sensor in structural studies. In theory, this effect can be achieved by lowering the stability of the inactivated and open states, increasing the stability of the resting state, or increasing the activation energy required to leave that state (Bezanilla, 2000).

The G/V curve of a channel approximates the percentage of channels in the closed vs open state during a short period of time at a given voltage (Lacroix et al., 2014). Evidence of the stabilization of a resting state at 0 mV would thus be shown in the form of a G/V curve with a substantial shift to more positive potentials. The lack of channel opening voltage pulses above 0 mV is a good indication that voltage-sensing has been altered in some manner (Lopez et al., 1991). We therefore examined the literature in search of mutations to the VSD that resulted in shifts of the G/V curve to more positive potentials in various types of ion channels.

Many comprehensive studies of channel gating have characterized the effect of mutations on channel opening as well as the gating charge movement (Fernández-Mariño et al., 2018; Kontis et al., 1997; Lopez et al., 1991; Perozo et al., 1994; Perry et al., 2013). These substitutions have been conservative and adventurous in the ways that they push the VSD to behave in very different ways depending on the amino acid side chains present in a given location. In this context, however, conservative refers to substitutions that preserve some of the fundamental properties of the native amino acid such as hydrophobicity or charge (DeCaen et al., 2008; Kontis et al., 1997). Other studies may form disulfide bonds between substituted cysteines (Lacroix et al., 2012), or neutralize the charged residues (Hoshi et al., 1994).

The first three gating charges of Na$_V$Ab, R1-R3, are highly conserved across many taxa, with the equivalent of the R4 position having a higher occurrence of lysine residues than the other three. Positively charged residues at the R1-R3 gating charge positions have been shown to directly interact with the hydrophobic constriction site during the voltage-dependent movement of the S4, (Zagotta et al., 1994b), and thus they must enter the membrane electric field during the gating process. In order to avoid altering the fundamental properties of gating, we searched the literature for mutations in other ion channels that shift the voltage-dependence of activation to more positive potentials with R1-R3 intact.

3.2 SELECTION OF SINGLE VOLTAGE SHIFTING MUTATIONS

The *Drosophila* channel *Shaker* B is perhaps the most thoroughly studied voltage-gated ion channel that exists (Fernández-Mariño et al., 2018; Zagotta et al., 1989, 1994a). Like in $\mathrm{Na_VAb}$, the homotetrameric structure of shaker makes mutagenesis studies less complicated than in heterotetramers, and its robust expression in *Xenopus* oocytes has been utilized for decades to examine the effects of drugs and mutations on voltage-sensitive properties of the channel (Auld et al., 1990; Lopez et al., 1991).

Extensive mutagenesis studies of the *Shaker B* VSD have elucidated the characteristics of conserved residues (hydrophobicity, size, charge, etc.) that are responsible for the functional changes produced by its mutagenesis. Studies in the early 90s revealed that hydrophobic substitutions on the S4 and S4-S5 linker had large shifts on the voltage-dependence of activation and inactivation of the channel (Kontis et al., 1997). The largest shifts were seen with mutations equivalent to position 112 in $\mathrm{Na_VAb}$ directly after R4 and position 119 which begins the S4-S5 linker, using numbering from 7DII. In *Shaker B*, both of these native residues were leucines, and the effect occurred when the former was mutated to an alanine and the latter was mutated to a valine. In 7DII, that would translate to L112A and M119V, respectively (Fig 3.1).

At the same position, L112 in 7DII, an introduced mutation led to a 20-25 mV positive shift in the voltage dependence of activation in the rat neuronal sodium channel subtype II ($Na_V1.2$)). This was caused by a mutation from a leucine to a phenylalanine at this the position corresponding to L112 in DII of the channel (Blanchet and Chahine, 2007). A separate study in this rat neuronal channel found a 10-20 mV positive shift when the fourth gating charge of DIII was mutated from an arginine to a lysine (as is present in DII), while a substitution of a glutamine at the same position produced a comparable *negative* shift (Gamal El-Din et al., 2013).

One specific mutation that has been shown to produce a 75 mV positive-shift of the activation voltage in multiple bacterial sodium channels is N48K (Lacroix and Bezanilla, 2011). This residue is placed in a conserved site on S2 that usually contains an ENC residue to act as a counterbalance to the gating charges. In Na_VAb, the native residue is not charged, and the resting state stabilization provided by its mutation to a charged residue is robust, so it was a promising candidate despite the fact that a fundamental property of the VSD would be altered by changing an uncharged hydrophilic residue to a positive charge.

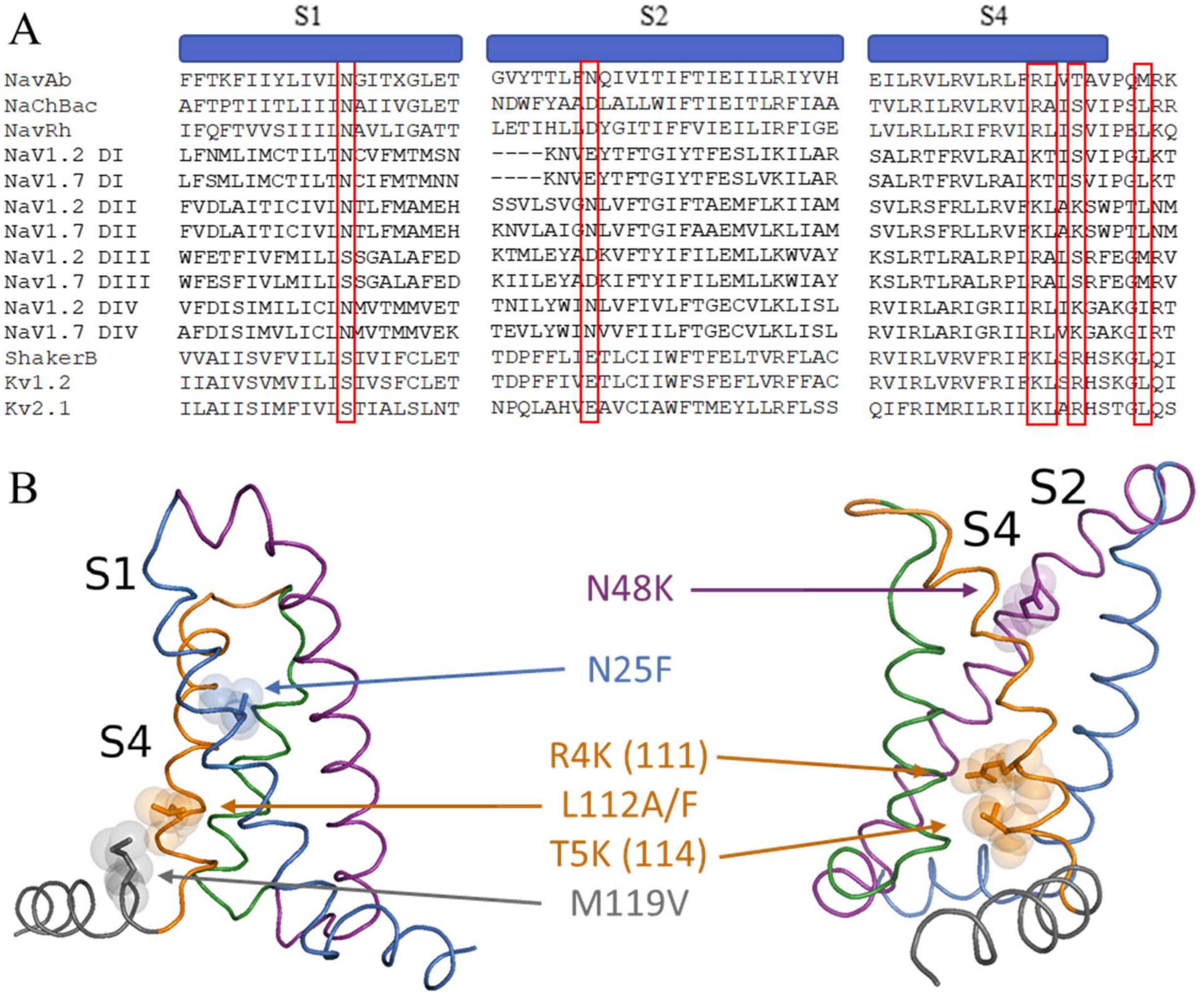

Figure 3.1 Substitutions studied in this project.

A) Sequence alignment (Clustal Omega) of transmembrane segments S1, S2 and S4 of Na_VAb (PDB 4EKW) with bacterial sodium channels NaChBac and NavRh, All four domains of human Na_V1.2 and Na_V1.7, *Drosophila* sodium channel *Shaker B*, and human Kv1.2 and Kv2.1. B) Ribbon representation of the S1-S4 and S4-S5 linker of Na_VAb with the native residues to be substituted colored according to the transmembrane segment on which it is located: S1 – Blue, S2 – Purple, S4 – Orange, and S4-S5 Linker – Grey.

Exhaustive mutagenesis studies by Lacroix et. al. provided valuable insight into effective ways to positively shift the voltage-dependence of activation with point mutations in the VSD (Lacroix et al., 2014). When studying the effects of an array of substitutions at given positions, they examined the voltage-dependent activation of the channel as well as the movement of the S4 itself for many mutations (Lacroix et al., 2014; Lacroix et al., 2012). Several substitutions produced a strongly positively shifted G/V curve while the Q/V curve remained mostly unchanged. In these cases, it seemed that the movement of the charges was split up into separate voltage-dependent events, one at lower voltages and one at voltages that correspond to the opening of the pore (Bezanilla, 2000).

We then focused on those mutations shown to shift of the full Q/V curve of the channel, and not just the second step that controls pore opening. Only two of the Lacroix mutations shifted the $V_{1/2}$ of the full Q/V curve to near 0 mV: N25F and V83S (Serrano et al., 1990). V83S did not create a change in the channel properties of 7DII; however, the N25F substitution shifted the Q/V curve by 50 mV in the positive direction, but the effect on the G/V curve was not reported.

3.3 CONSTRUCTION AND ANALYSIS OF SINGLE VOLTAGE SHIFTING MUTATIONS

In this portion of the project, we constructed and characterized seven single substitutions: N25F, N48K, L112A, L112F, R4K (111), T5K (114), and M119V. Their locations on the S1, S2, and S4/S4-S5 linker are presented in Figure 3.2. Numbering corresponds to 7DII and not the channels of origin.

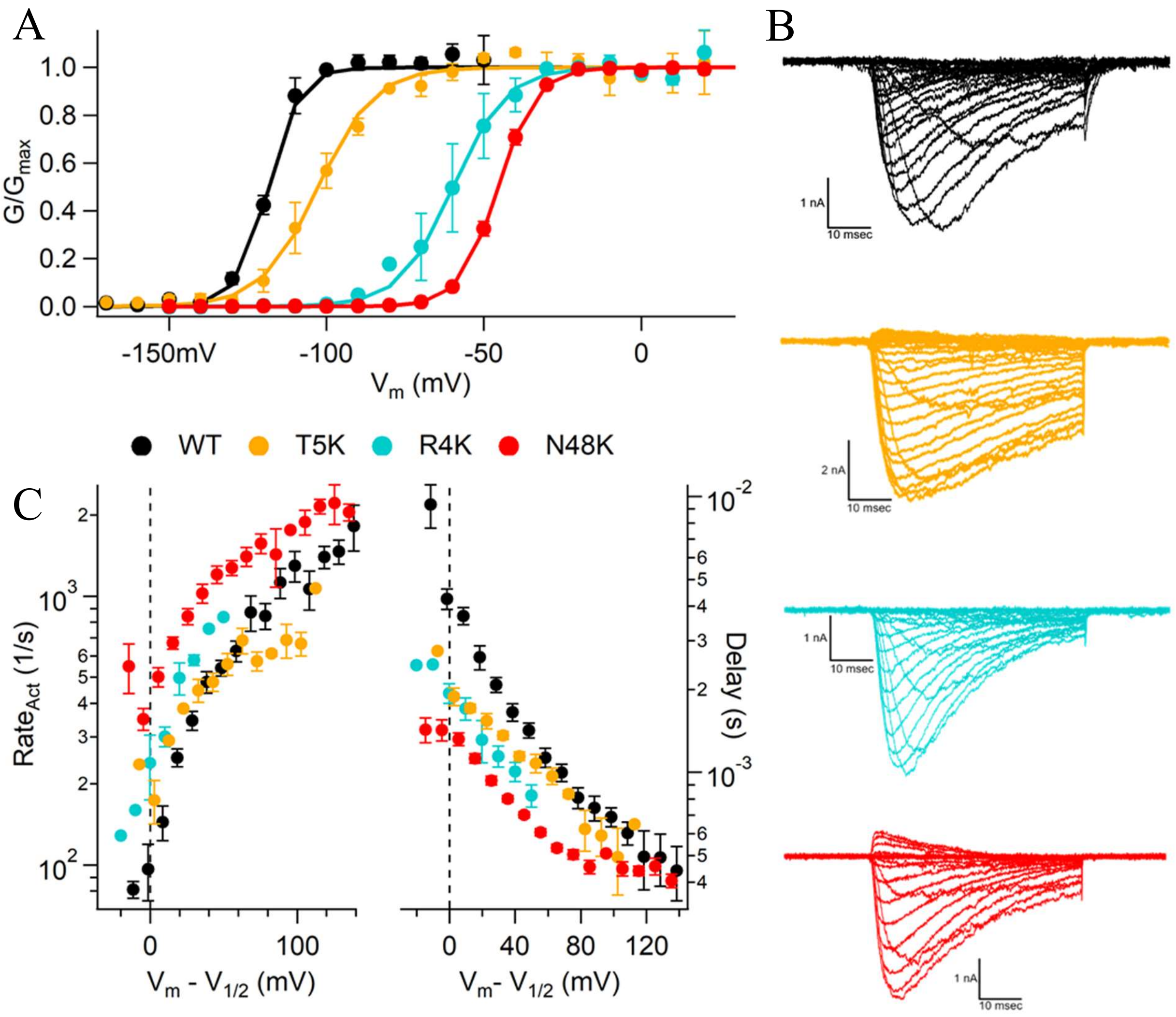

Figure 3.2 Effects of the N48K, R4K, and T5K single substitutions.

A) The conductance voltage (G/V) relationship of 7DII WT and with three individual charged residue substitutions. B) Representative current families of each construct. C) The rate of activation (inverse tau) of the rising phase of the exponential growth of the current. A single exponential (1+exp(-(x-x_0)/tau)) was fit to the trace, and the tau value was divided by one to get the rate of transition. The delay associated with the activation of the channel is represented by the y-intercept of the resulting fit line to the rising phase of the current. The x-values are normalized to the $V_{1/2}$ of the activation curve of the specific construct to allow for comparison across a wide range of voltage-dependencies. All values are mean +- sem.

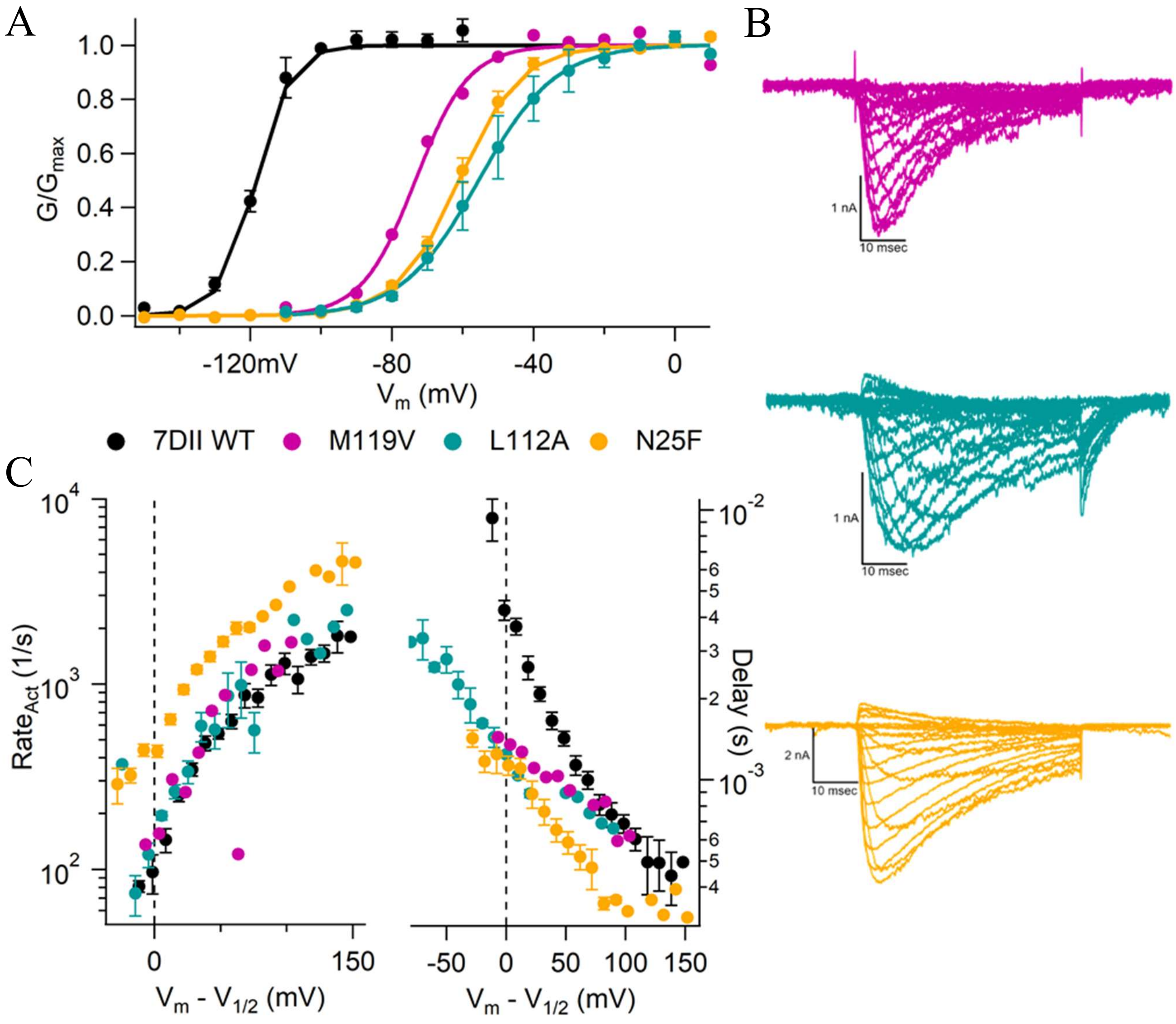

Figure 3.3 The effect of N25F, L112A, and M119V substitutions on activation.

A) The conductance-voltage relationship of Na$_V$Ab with three separate hydrophobic substitutions in the VSD. B) Representative current families of each construct. C) The rate of activation (inverse tau) of the rising phase of the exponential growth of the current. A single exponential (1+exp(-(x-x$_0$)/tau)) was fit to the trace, and the tau value was divided by one to get the rate of transition. The delay associated with the activation of the channel is represented by the y-intercept of the resulting fit line to the rising phase of the current. The x-values are normalized to the V$_{1/2}$ of the activation curve of the specific construct to allow for comparison across a wide range of voltage-dependencies. All values are mean +- sem.

The substitution of the three charged residues studied in 7DII – R4K, T5K, and N48K – all resulted in positive shifts of the voltage dependence of activation of the channel, with T5K causing a 15 mV shift to a $V_{1/2}$ of -103 mV, R4K causing a 59 mV shift to -60 mV, and N48K causing a 73 mV shift to -45 mV (Figure 3.2). The rate of opening was increased the most by the N48K mutation, and this construct also had the shortest delay to opening. The delay values for N48K seem to level off at voltages around 80 mV above $V_{1/2}$ while the other constructs continue to speed up over that range. It is possible that they may converge at one delay value once it is reached, but the recordings did not study voltages high enough to test that in experiments with these constructs. A tail current was not observed upon repolarization in these channels, indicating a fast rate of deactivation in response to a step to -180 mV.

The N25F substitution increased the rate of activation as well as shortened the delay, especially at voltages much higher than $V_{1/2}$ (Figure 3.3). The steepness of the change in rate is not different among the four constructs, but the voltage-dependent effects on the delay of opening are variable: L112A and N25F seem to have the same slope initially in the activation range, and WT is slower to open at all but the highest voltages.

In the initial studies in *Shaker B*, the equivalent of L112A positively shifts to a greater extent than M(L)119V: by 86 and 65 mV, respectively. In 7DII, this shift was smaller. L112A shifted the G/V by 63.4 mV and M119V shifted it by 45 mV. Although we cannot compare the G/V curves of the *Shaker B* and 7D11 N25F substitutions, we see that N25F shifted the $V_{1/2}$ by 57.4 mV, which is greater than the 50 mV shift seen in the Q/V curve of that substitution in *Shaker B*. See Table 2 for more information on the G/V curves of all single substitutions.

Table 2 - Activation parameters for 7DII single substitutions

Mutant	Act $V_{1/2}$	k	z_{app}	n
7DII WT	-118.43 ± 0.89	5.01 ± 0.35	5.13 ± 0.39	7
N25F	-61.02 ± 1.44	8.65 ± 0.48	2.91 ± 0.17	5
N48K	-45.41 ± 0.87	5.98 ± 0.24	4.2 ± 0.16	8
N48K d28	-47.76 ± 1.78	6.87 ± 0.30	3.63 ± 0.15	3
R4K (111)	-59.77 ± 6.63	8.41 ± 0.57	2.96 ± 0.02	2
L112A	-54.96 ± 4.91	10.48 ± 1.65	2.43 ± 0.38	2
T5K (114)	-102.63 ± 2.94	8.95 ± 1.05	2.86 ± 0.36	3
M119V	-73.3604	7.5521	3.29323	1

The half maximal voltage, slope factor, and apparent charge movement. Mean ± SEM

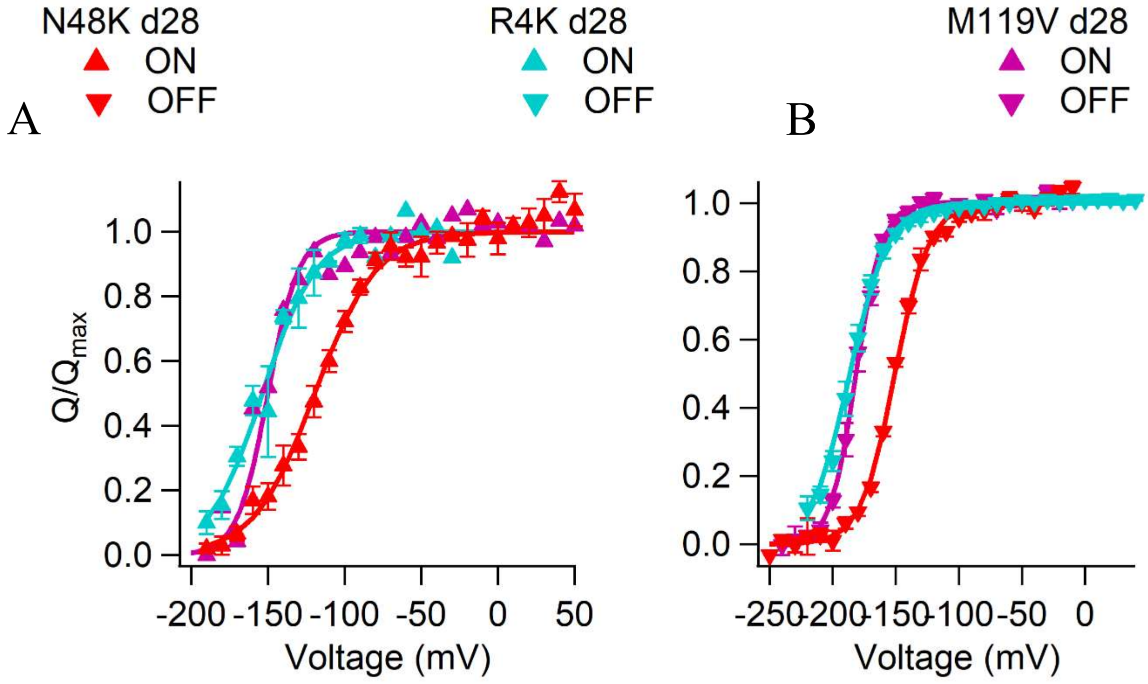

Figure 3.4 The gating charge movement of N48K, R4K and M19V single mutations.

A) On gating charge movement in response to depolarization in media that contained NMDG-Cl substituted for NaCl and CaCl2. Cells were briefly hyperpolarized and then the subsequent current step was increased in 10 mV increments. A P/5 leak subtraction was used at voltages that remained well outside the range of charge movement, either very positive, or very negative. The area under the curve was calculated and plotted as a function of voltage. B) Off gating charge movement in response to hyperpolarization following brief depolarization prepulse.

Table 3 - On and Off gating charge parameters for 7DII single mutants

Mutant	On $V_{1/2}$	k	z_{app}	n
N48K	-119.38 ± 2.88	19.89 ± 1.66	1.26 ± 0.10	4
M119V	-155.36	14.69	1.69	1
R4K	-153.65 ± 4.48	17.32 ± 0.69	1.42 ± 0.06	2
	Off $V_{1/2}$	k	z_{app}	n
N48K	-150.66 ± 0.78	13.35 ± 0.71	1.86 ± 0.09	5
M119V	-179.89 ± 1.96	8.92 ± 1.14	2.97 ± 0.48	4
R4K	-186.56 ± 2.86	15.03 ± 1.07	1.67 ± 0.12	5

The half maximal voltage, slope factor, and apparent charge movement. Mean ± SEM

3.4 EFFECTS OF SINGLE VOLTAGE SHIFTING MUTATIONS ON GATING CHARGE MOVEMENT

The truncation mutation $Na_VAb\Delta28$ (d28) removes the last 28 residues from the C-terminus of the channel (Gamal El-Din et al., 2017; Lenaeus et al., 2017), and it has the effect of increasing the amount of current recorded in similarly transfected cells expressing the full-length channel. It does not change the G/V properties or kinetics of opening of the channel (see Figure 5.1), and it is helpful when a high level of channel expression is needed, as it is in gating charge measurements. We studied a subset of mutations to determine if the shifts in G/V curves were accompanied by similar shifts in the voltage-dependent movement of the gating charges in the $Na_VAb\Delta28$ construct.

The voltage-dependent increase in the outward movement of the S4 gating charges can be measured by integrating the current recorded in response to brief depolarizing steps after a hyperpolarizing prepulse to force all S4 segments to move to the resting state. This protocol is referred to as measuring the “On” gating currents in this study, where ‘On’ refers to S4 movement from the resting to the activated state and ‘Off’ refers to voltage dependent movement in the other direction. The integral of the current gives a measurement of charge, and this can be plotted against voltage, normalized to peak, and fit with a Boltzmann similarly to G/V curves. Similarly, the inward 'Off' measurements are made after a brief depolarization. The $V_{1/2}$ of the On and Off Q/V curves were similar for R4K and M119V, while N48K $V_{1/2}$ was shifted roughly 35 mV more positive than R4K and M119V for both On and Off measurements (Figure 3.5). The slopes indicate a slight difference in the number of charges moved, but this is likely influenced by errors in the normalization process, as evidenced by the R4K proportion of charges moved extending only to 0.2 at the most negative voltages tested. Without gating current recordings of 7DII WT, which were not possible because of its negative voltage dependence, it is difficult to draw conclusions as to the effect of the mutations on gating charge movement. Here we are able to see that the onset of S4 movement is much more negative than the initial conductance measured by the G/V curve. This is to be expected, as channel opening is associated with the final movements of the VSDs to the outward position which occurs at higher voltages (Fernández-Mariño et al., 2018). The difference between the $V_{1/2}$ of the On and Off currents is around 30 mV for all three constructs, which indicates a similar level of VSD trapping occurring due to inactivation during the prepulse. These data begin to paint a picture of small changes to the VSD that can lead to both large and small alterations of S4 movement and pore opening. See table 3.

Chapter 4. COMBINATORIAL MUTATION EFFECTS

4.1 BACKGROUND

The individual mutations gave promising results by showing substantial shifts in the voltage dependence of channel opening and moderate shifts in the gating charge movement, so we were curious if the effects of individual mutations could be combined to further positively shift the voltage-dependence of the channel and tune it to the positive voltage range. A formal method of investigating additivity exists (Chowdhury et al., 2014), but recently consensus has shifted away from doing this analysis on G/V curves (Antala et al., 2015; Perry et al., 2013). As discussed previously, voltage-dependent activation of sodium conductance requires outward gating charge movement, but it does not necessarily track the physical outward movement of the gating charges. Q/V curves are a more precise means of determining whether mutations at different positions physically interact to produce synergistic effects or operate with a mechanism that is independent of the other. Any inferences drawn from mutant cycle analysis of the G/V curve cannot be interpreted as a direct physical interaction, and so it was not used to describe individual versus synergistic effects as a function of Gibbs free energy here. We nonetheless strove to understand how combinations of these single substitutions would affect voltage-dependent gating of the channel, and many combinations of mutations were investigated.

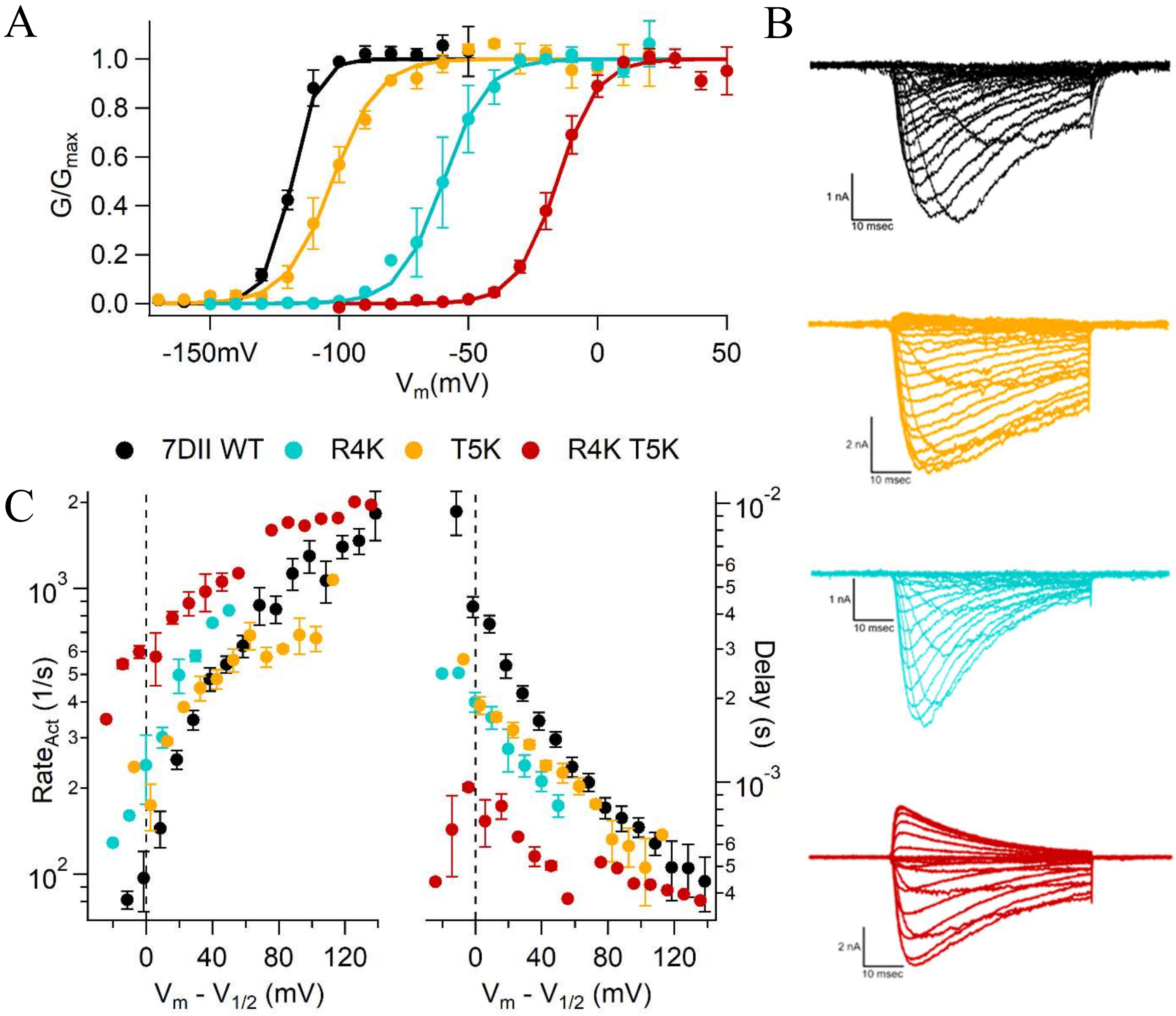

Figure 4.1 Combinatorial effects of R4K and T5K on 7DII

A) The conductance-voltage relationship of Na$_V$Ab R4K alone, T5K alone, and the two in combination. B) Representative current families of each construct. C) The rate of activation (inverse tau) of the rising phase of the exponential growth of the current. A single exponential (1+exp(-(x-x_0)/tau)) was fit to the trace, and the tau value was divided by one to get the rate of transition. The delay associated with the activation of the channel is represented by the y-intercept of the resulting fit line to the rising phase of the current. The x-values are normalized to the $V_{1/2}$ of the activation curve of the specific construct to allow for comparison across a wide range of voltage-dependencies. All values are mean +- sem.

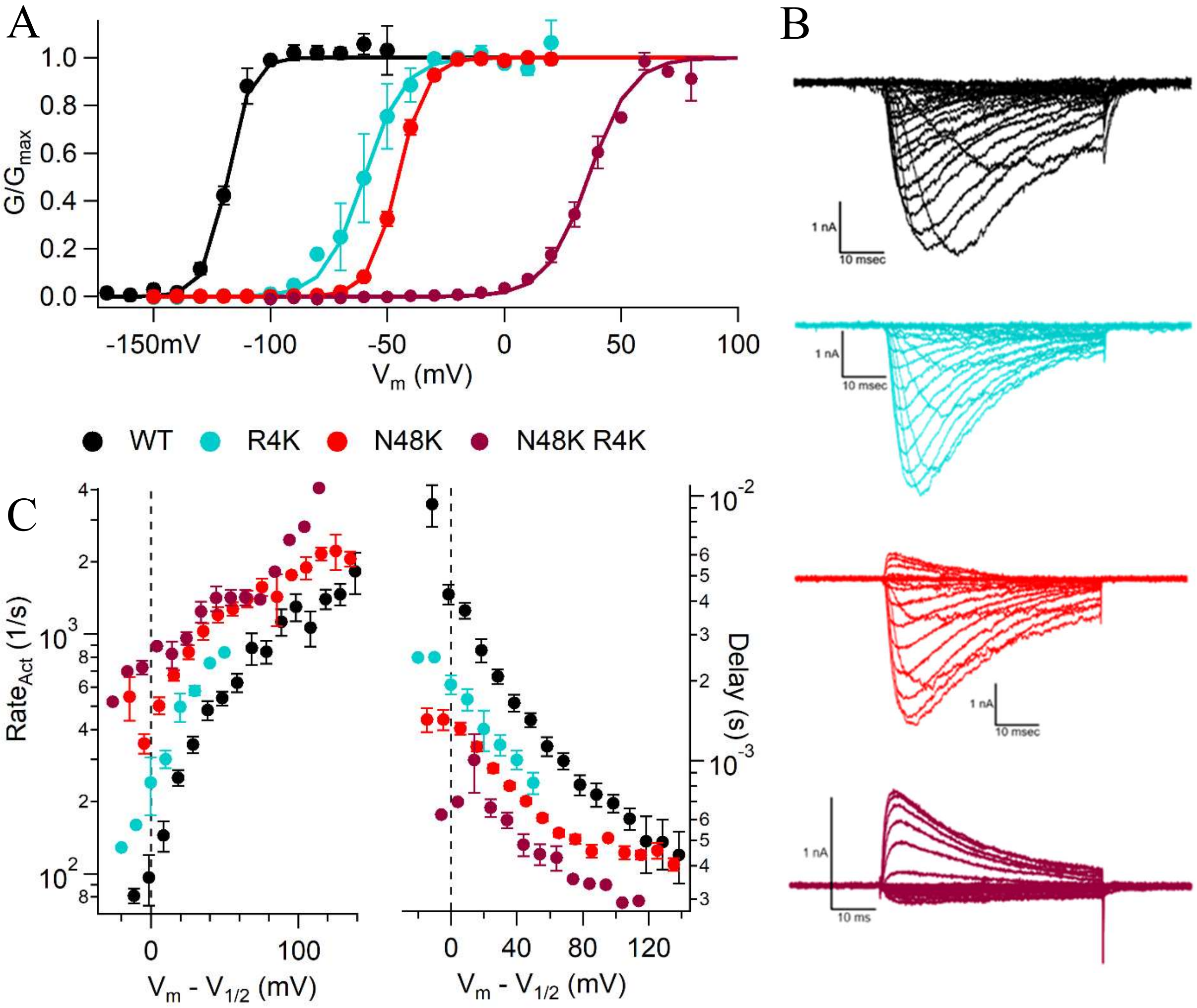

Figure 4.2 Effects of N48K and R4K in combination

A) The conductance-voltage relationship of Na_VAb R4K alone, N48K alone, and the two in combination. B) Representative current families of each construct. C) The rate of activation (inverse tau) of the rising phase of the exponential growth of the current. A single exponential ($1+\exp(-(x-x_0)/tau)$) was fit to the trace, and the tau value was divided by one to get the rate of transition. The delay associated with the activation of the channel is represented by the y-intercept of the resulting fit line to the rising phase of the current. The x-values are normalized to the $V_{1/2}$ of the activation curve of the specific construct to allow for comparison across a wide range of voltage-dependencies. All values are mean +- sem.

4.2 ANALYSIS OF COMBINED VOLTAGE SHIFTING MUTATIONS

The effect of the combination of T5K and R4K were apparently synergistic, as the total shift in voltage of the double mutant (112 mV) was greater than the sum of the two initial shifts (74 mV, Figure 4.1.A, Table 2). The double mutant has a faster opening rate and shorter delay than WT or the single mutants, but the steepness of the voltage-dependent changes in rate and delay was much lower for the double mutant (Figure 4.1.C), which suggests as above that there may be a plateau that is achieved either due to intrinsic properties of the VSD or to the limitations of the voltage-clamp setup. No tails are present in the R5K T5K double mutant either despite a very strong driving force on sodium at -180 mV with a reversal potential of +45 mV, which suggests a very fast deactivation upon hyperpolarization that the amplifier cannot clamp (Figure 4.1.B).

The combinatorial effects of N48K and R4K demonstrate an incremental change in both voltage-dependent activation and speed of opening (Figure 4.2.A, C). The total shift in the $V_{1/2}$ of the double mutant is 154 mV, which is slightly more than the sum of the individual shifts of R4K and N48K alone which is 132 mV (Table 2). The delay to opening is much faster for the double mutant than for any other construct, and the steepness of the voltage dependent effect is similar to that of N48K alone (Figure 4.2.B). The rate of opening of the double mutant overlaps with N48K as well. For this channel we begin to see a tail current, but it is very short lived (Figure 4.2.B).

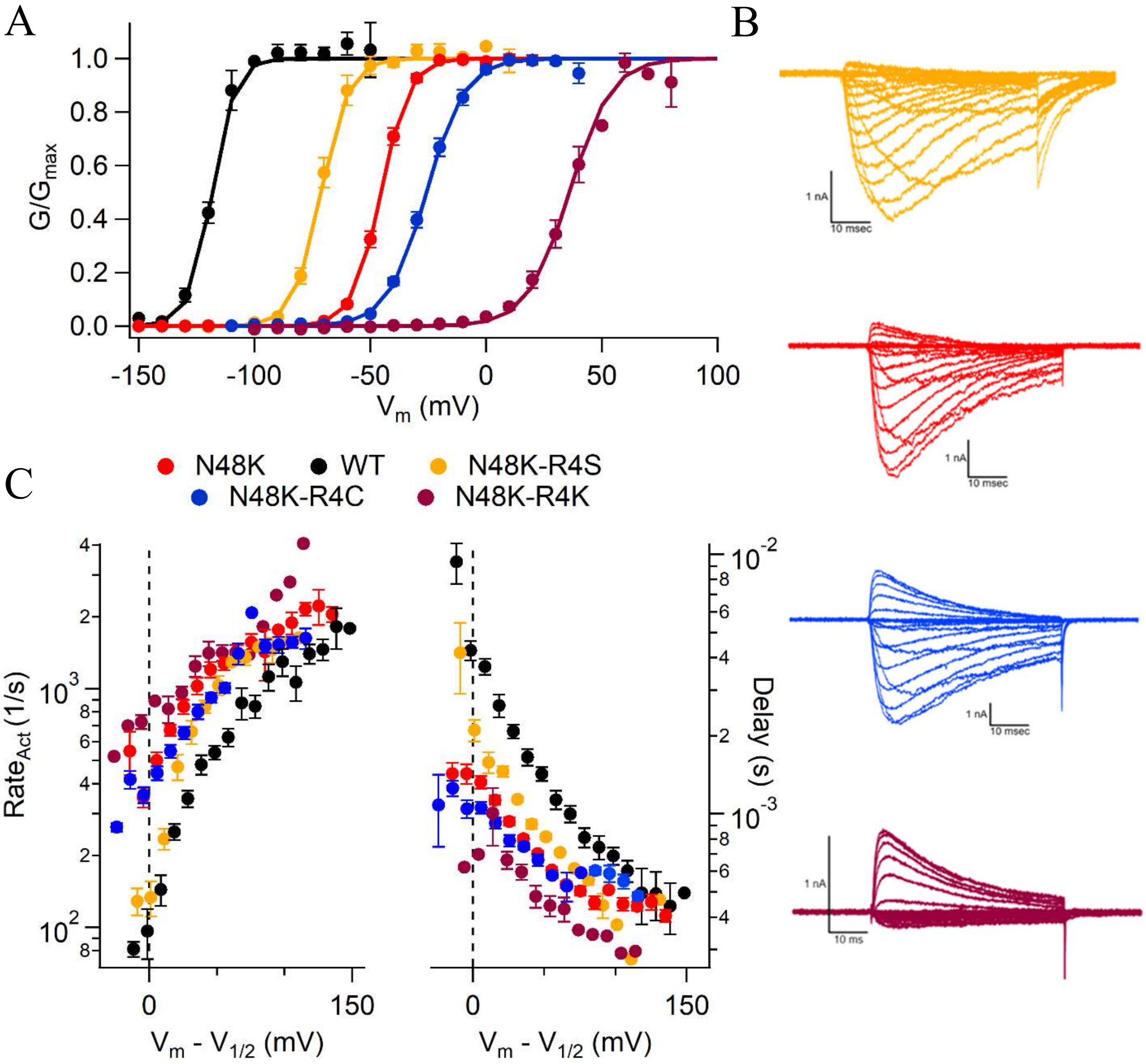

Figure 4.3 Additional R4 substitutions on the background of N48K

A) The conductance-voltage relationship of Na$_V$Ab coupled with R4 substitutions that do not conserve the charge. B) Representative current families of each construct. C) The rate of activation (inverse tau) of the rising phase of the exponential growth of the current. A single exponential $(1+exp(-(x-x_0)/tau))$ was fit to the trace, and the tau value was divided by one to get the rate of transition. The delay associated with the activation of the channel is represented by the y-intercept of the resulting fit line to the rising phase of the current. The x-values are normalized to the V$_{1/2}$ of the activation curve of the specific construct to allow for comparison across a wide range of voltage-dependencies. All values are mean +- sem.

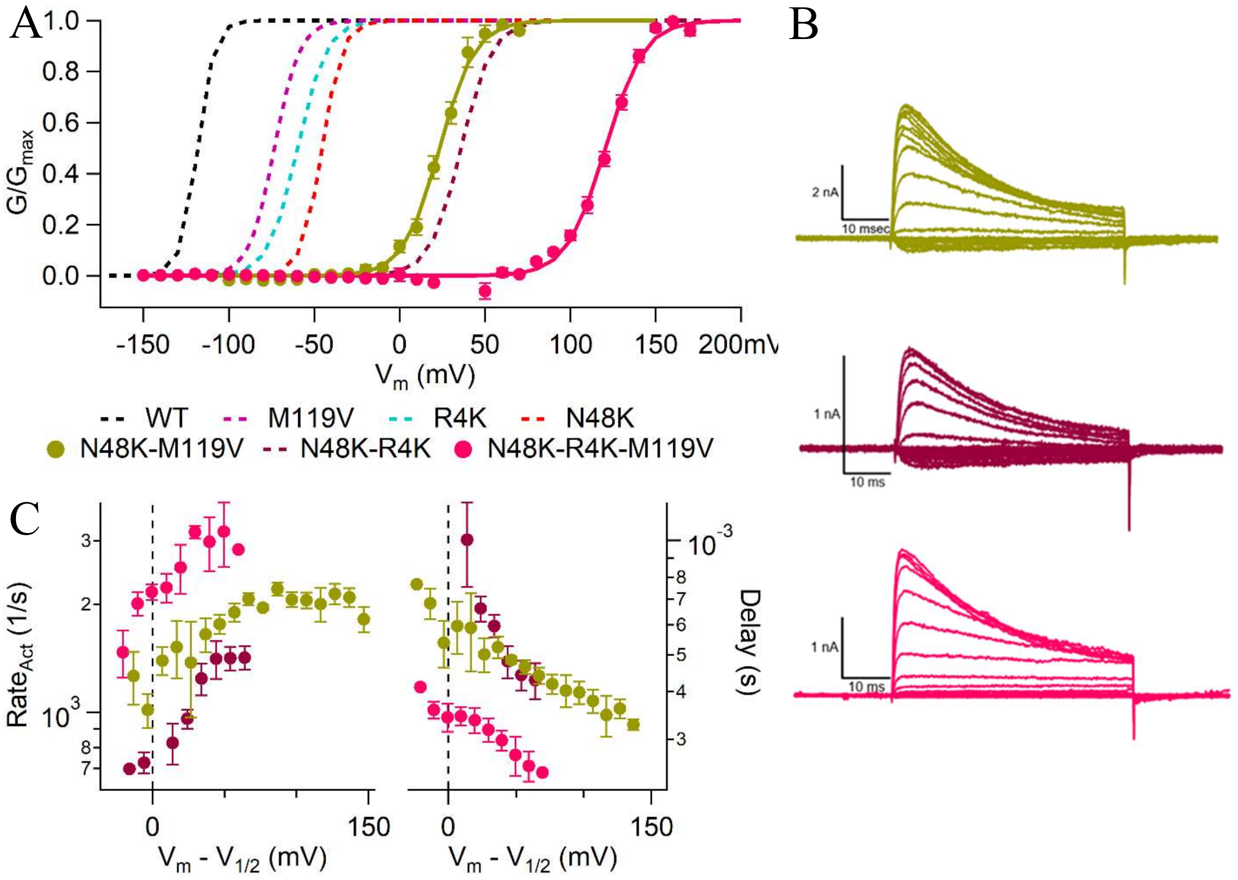

Figure 4.4 Addition of M119V to N48K and R4K combinations produces further shifts. A) The conductance-voltage relationship of Na$_V$Ab N48K when paired with M119V, R4K, and a combination of both. B) Representative current families of each construct. C) The rate of activation (inverse tau) of the rising phase of the exponential growth of the current. A single exponential (1+exp(-(x-x$_0$)/tau)) was fit to the trace, and the tau value was divided by one to get the rate of transition. The delay associated with the activation of the channel is represented by the y-intercept of the resulting fit line to the rising phase of the current. The x-values are normalized to the V$_{1/2}$ of the activation curve of the specific construct to allow for comparison across a wide range of voltage-dependencies. All values are mean +- sem.

Several substitutions of R4 in addition to R4K were tested on the background of N48K in the initial screen: R4C, R4E, R4N, R4Q and R4S. Only two of these, R4C and R4S, resulted in a functional channel. These two substitutions had opposite effects in shifting the V$_{1/2}$ of the G/V curve relative to N48K alone. R4S produced a 25 mV negative shift compared to N48K, resulting in a $V_{1/2}$ intermediate between N48K and WT. R4C produced a 20 mV positive shift in the $V_{1/2}$ to a final value of -25.8 mV Figure 4.3.A). Neither produced as robust of a positive shift as N48K R4K, and likewise neither of their opening rates or delay to opening values were as fast as N48KR4K, but these values for N48KR4C are comparable to N48K alone while R4S slows these processes down (Figure 4.3.C). A tail current with a slow decay back to baseline can also be seen for N48KR4S, which suggests a stabilization of the open state (Figure 4.3.B).

The triple mutant N48K-R4K-M119V produced the largest shift in $V_{1/2}$ of all constructs tested, 240 mV, to give a $V_{1/2}$ value of 121 mV (Figure 4.4.A). The kinetics of opening are also much faster than either N48K-R4K, which was otherwise the construct with the fastest rates and shortest delays of all (Figure 4.4.C). These values indicate that the channel responds very quickly to voltages that are sufficient to activate the VSD, meaning that the movement of the S4 at those voltages is tightly coupled to opening. N48K-M119V has rate of opening values that are intermediate between the other two and similar delay values to N48K-R4K, indicating that the S4 movement is either slowed by an interaction caused by R4 or accelerated by K4, the translation of this movement to pore opening is affected by the substitution, or both. The voltage dependence of the changes in rate and delay do not appear to level off for any of these constructs. See Table 6.

Because of this large shift in the G/V curve, it was important that we investigate the Q/V curves for similar changes, but no such effects were found for the double-mutants tested. The $V_{1/2}$ of the On Q/V were seen at substantially more negative voltages than the G/V curves (Figure 4.5.A). The off gating currents were further shifted in the negative direction, as can be expected (Figure 4.5.B), and the full range of voltages for the N48K-R4K Q/V could not be tested. The Off Q/V curves for N48K-M119V and R4K-M119V almost completely overlap. See Table 4.

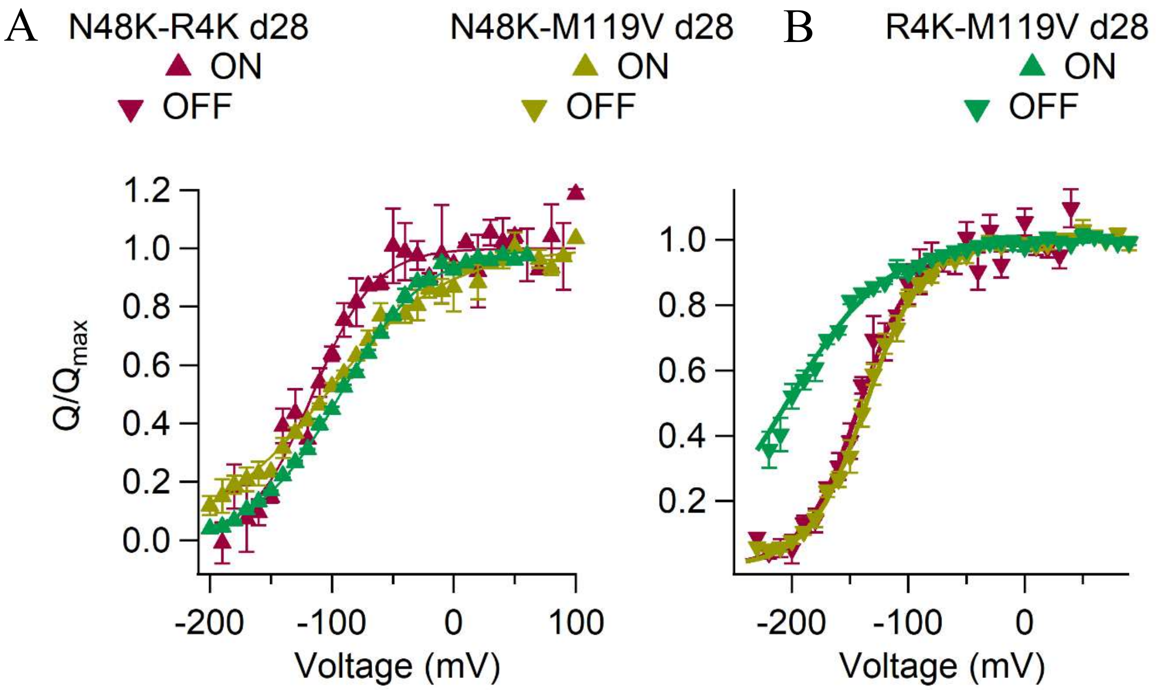

Figure 4.5 Gating charge measurement of N48K, R4K, and M112V combinations

A) On gating charge movement in response to depolarization in media that contained NMDG-Cl substituted for NaCl and CaCl2. Cells were briefly hyperpolarized and then the subsequent current step was increased in 10 mV increments. A P/5 leak subtraction was used at voltages that remained well outside the range of charge movement, either very positive, or very negative. The area under the curve was calculated and plotted as a function of voltage. B) Off gating charge movement in response to hyperpolarization following brief depolarization prepulse. All values represent mean ± SEM.

Table 4 - On and Off gating current parameters for 7DII double mutants

Mutant	On $V_{1/2}$	k	z_{app}	n
N48K R4K	-115.832 ± 1.54	25.26 ± 1.48	0.98 ± 0.06	2
N48K M119V	-92.99 ± 0.50	35.10 ± 0.23	0.704 ± 0.01	2
R4K M119V	-104.85 ± 2.69	49.14 ± 7.23	0.51 ± 0.08	2

	Off $V_{1/2}$	k	z_{app}	n
N48K R4K	-141.40 ± 3.18	24.08 ± 3.89	1.09 ± 0.14	4
N48K M119V	-136.25 ± 3.25	24.73 ± 1.16	1.00 ± 0.46	5
R4K M119V	-204.45 ± 7.23	43.10 ± 5.46	0.59 ± 0.08	3

The half maximal voltage, slope factor, and apparent charge movement. Mean ± SEM

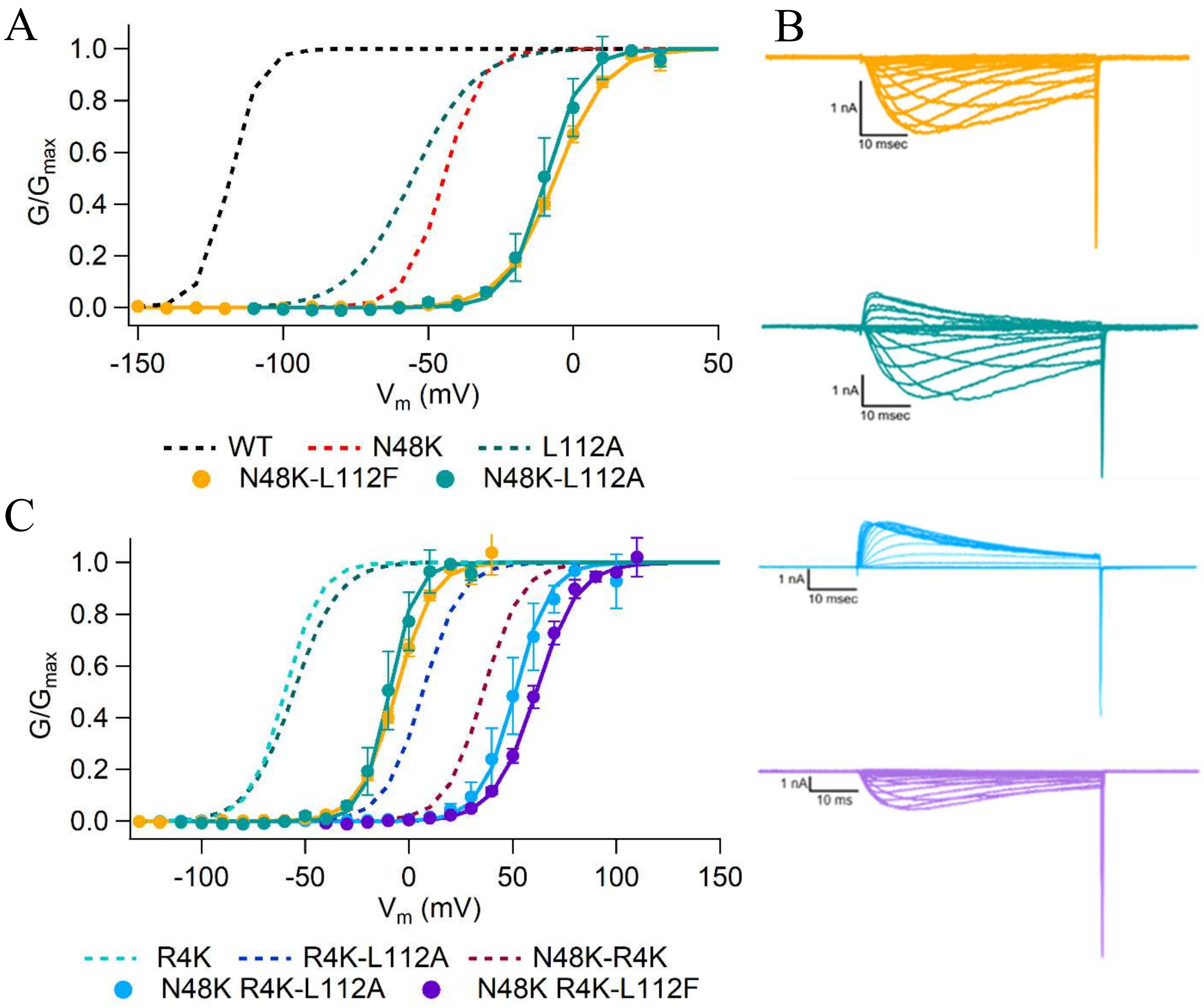

Figure 4.6 Similar effects of L112A and L112F on activation properties
The conductance-voltage relationship of NaVAb R4K alone, T5K alone, and the two in combination. B) Representative current families of each construct. C) The conductance-voltage relationship of the above constructs compared to NaVAb N48K-R4K-L112A and N48K-R4K-L112F. All values are mean +- sem.

At residue L112, substitutions of an alanine and a phenylalanine were studied in combination with N48K and R4K together. When combined with N48K, L112A and L112F had similar $V_{1/2}$ values at -9 and -6 mV, respectively (Figure 4.6.A), and the positive shift from N48K alone was an average of 40 mV. With the further addition of R4K, the two triple mutants again had similar $V_{1/2}$ values at +51 mV for N8K-R4K-L112A and +61 mV for N48K-R4K-L112F (Figure 4.6.C). The shift between N48K and N48K-R4K was 81 mV in the positive direction, and when R4K was added to N48K-L112A and N48K-L112F, the shift was much smaller at 41.8 mV and 55 mV, respectively, suggesting that there is an interaction between R4K and the L112 substitutions. This is not unreasonable, since L112 is the position immediately after R4K. All of these constructs had substantial tail currents (Figure 4.6.C) when none of the corresponding mutants without a substitution at L112 (N48K, R4K, and N48K-R4K; Figure 4.2.B) displayed a significant tail current, which indicates that both substitutions produce an effect on deactivation that is not reduced by R4K, despite its proximity and apparent interaction as indicated by the G/V shift.

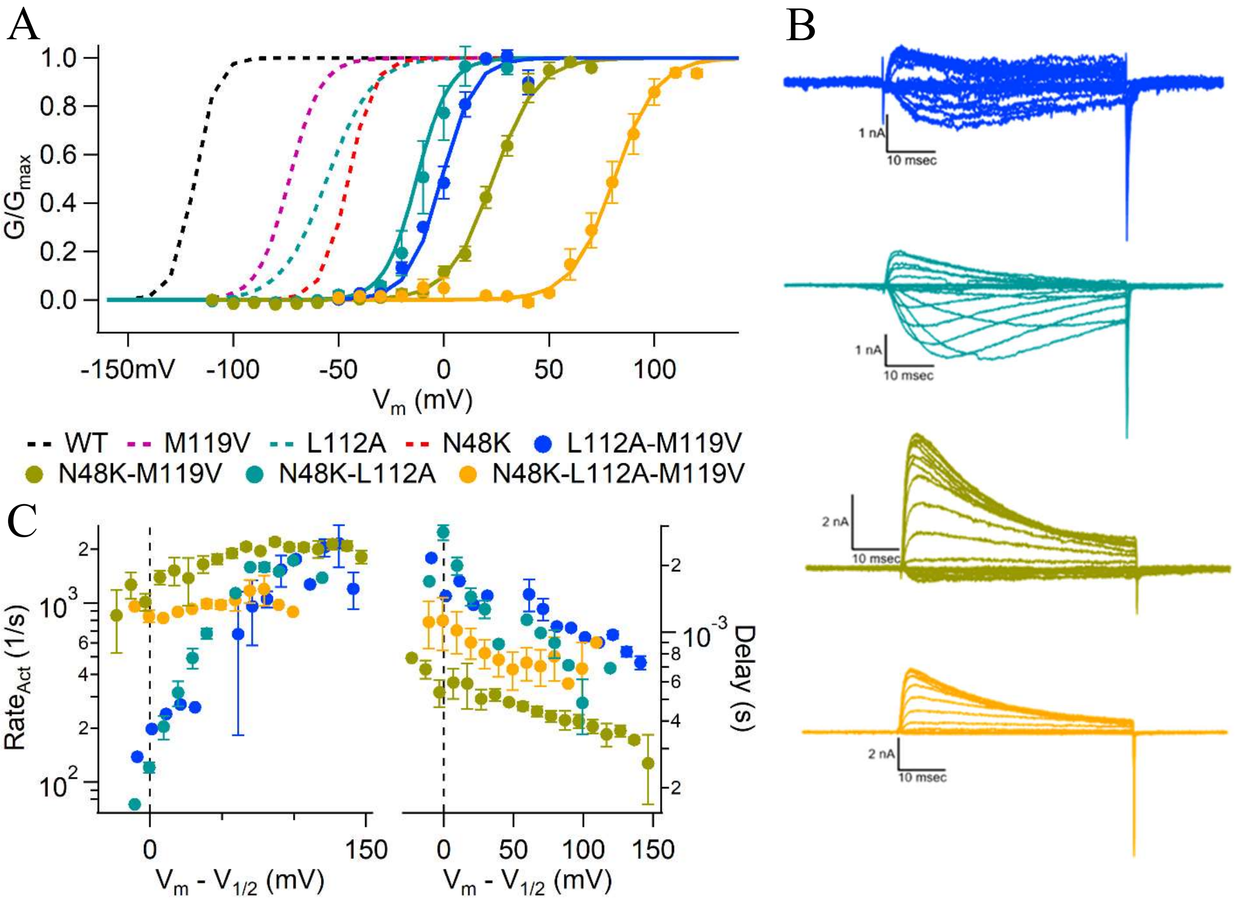

Figure 4.7 Combinations of N48K, L112A, and M119V (KAV)

A) The conductance-voltage relationship of Na$_V$Ab with N48K, M119V, L112A, and the effect of all three together. B) Representative current families of each construct. C) The rate of activation (inverse tau) of the rising phase of the exponential growth of the current. A single exponential (1+exp(-(x-x$_0$)/tau)) was fit to the trace, and the tau value was divided by one to get the rate of transition. The delay associated with the activation of the channel is represented by the y-intercept of the resulting fit line to the rising phase of the current. The x-values are normalized to the V$_{1/2}$ of the activation curve of the specific construct to allow for comparison across a wide range of voltage-dependencies. All values are mean +- sem.

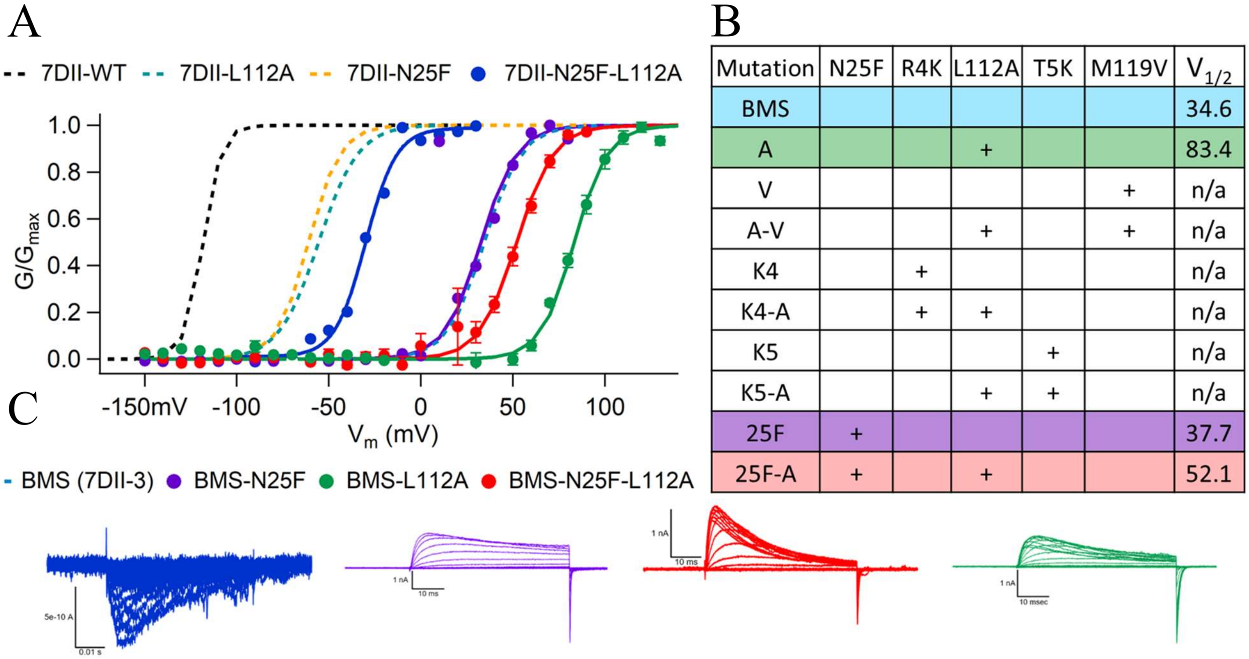

Mutation	N25F	R4K	L112A	T5K	M119V	$V_{1/2}$
BMS						34.6
A			+			83.4
V					+	n/a
A-V			+		+	n/a
K4		+				n/a
K4-A		+	+			n/a
K5				+		n/a
K5-A			+	+		n/a
25F	+					37.7
25F-A	+		+			52.1

Figure 4.8 L112A and N25F effects on 7DII-3 chimera

A) The effect on the conductance voltage relationship of L112A and N25F alone and in combination on the background of 7DII and the more humanized 7DII-3 (BMS) channel. B) A chart highlighting the effect of single and double substitutions described above on the 7DII-3 background on the $V_{1/2}$ of channel activation, where n/a denotes a channel which did not pass a sodium current at voltages that could be measured. C) Representative current families of each construct. All values are mean +- sem.

The L112A substitution was also combined with N48K and M119V to produce a triple-mutant channel with a voltage-dependent activation $V_{1/2}$ (Figure 4.7.A) of 81 mV and opening kinetics intermediate to the fast N48K-M119V and the slow L112A-M119V and N48K-L112A. The rate of opening for N48K-L112A and L112A-M119V as well as the delay to opening showed a near complete overlap (Figure 4.7.C), and these values were very similar to the L112A single mutant, as well (Figure 3.2.C). This suggests that the effect of L112A to slow opening kinetics can counteract the increase in these values when M119V or N48K is present. Only when all three substitutions were combined to produce N48K-L112A-M119V (KAV) did the rate of opening increase. The tail current, however, was still observed, again indicating that the effect of these L112 substitutions on deactivation rates was not substantially altered by N48K or M119V (Figure 4.7.B). See table 6 for a comparison of all 7DII combinatorial mutations.

The addition of positive-shifting mutations to the more humanized 7DII chimera from Ramkumar et. al. (listed as 7DII-3 in Chapter 2 and BMS in figure 4.8 to prevent confusion) resulted in similarities and differences regarding the effects of the substitutions on voltage-dependent activation properties. Introducing the positive-shifting mutations often resulted in a nonfunctional channel (Figure 4.8.B). Only two of the substitutions studied above produced a sodium channel that retained its function: L112A and N25F. While L112A caused a positive shift in the G/V curve of around 50 mV, N25F was nearly indistinguishable when compared to 7DII-3 alone (Figure 4.8.A). In 7DII, the shift caused by L112A was 63 mV, and for N25F it was 57 mV (Table 2). When the two residues were mutated in combination, the channel was still functional, but the addition of N25F to L112A caused a negative shift of 30 mV in the $V_{1/2}$ compared to L112A alone (Figure 4.8.A). In the 7DII background, the double mutant was more positively shifted than either of the two single mutants, but the effects were clearly not additive (Figure 4.8.A, left). See Table 5.

The two substitutions that were studied in the L112 position, alanine and phenylalanine, are drastically different from one another in size, and both are hydrophobic. At physiological pH, however, leucine is less hydrophobic than phenylalanine and more hydrophobic than alanine, and yet their effects on voltage-dependent activation in combinatorial substitutions with N48K and R4K are nearly identical (Figure 4.6). These two substitutions are also the only ones that dependably produce tail currents upon repolarization of the membrane following test pulses, which implies that a similar interaction with the two substitutions facilitates the generation of these tail currents, presumably due to a slowing of the conformational change that occurs during deactivation. It is a challenge to predict a potential mechanism for this interaction, as it can be induced by large and small residues and it does not occur with the native residue that is intermediate in both size and hydrophobicity compared to the other two. It's possible that they could be interacting with a lipid to produce this effect, but how lipids contribute to activation gating in bacterial sodium channels is not well understood.

A study in Kv11.1 determined that the hydrophobic interactions of the analogous residue at position 112 (V535) were important in determining the inactivation gating properties (Irie et al., 2018). The effects on activation caused by a wide array of substitutions at this residue do not have the same results in Kv11.1 that we see here, however the alanine substitution V535A caused a 75 mV positive shift in the $V_{1/2}$ of activation, which is not far from the 63 mV shift in 7DII (Table 2). In contrast, a phenylalanine at this position only shifted the $V_{1/2}$ by 6 mV. Other substitutions that produced large positive shifts at this position were tyrosine (52 mV) and asparagine (58 mV). Since the native residue in this study is valine instead of leucine, it can be expected that different results will be seen for substitutions. It is compelling that such a strong effect of the alanine substitution is seen in yet another channel. If the mechanism through which this occurs is reproducibly effective in a wide range of VSDs, a global property of the VSD could be identified.

Table 5 - The activation parameters of 7DII-3 and substitutions

Mutant	Act $V_{1/2}$	k	z_{app}	n
7DII-3	34.59 ± 1.36	10 ± 0.46	2.51 ± 0.12	6
L112A	83.37 ± 0.93	9.11 ± 0.55	2.74 ± 0.16	2
N25F	32.71	9.86	2.52	1
N25F L112A	52.08 ± 2.53	10.02 ± 0.75	2.52 ± 0.20	4

The half maximal voltage, slope factor, and apparent charge movement. Mean ± SEM

Table 6 - The activation parameters of 7DII and combinations of substitutions

Mutant	Act $V_{1/2}$	k	z_{app}	n
7DII WT	-118.43 ± 0.89	5.01 ± 0.35	5.13 ± 0.39	7
7D2N25FM119V*	14.26 ± 0.17	12.39 ± 0.11	2.01 ± 0.2	2
7D2N48KL112F	-6.25 ± 1.08	8.74 ± 02.4	2.85 ± 0.08	5
7D2N48KL112A	54.96 ± 4.91	10.48 ± 1.64	2.43 ± 0.38	2
7D2N48KM119V	23.31 ± 1.91	10.42 ± 0.34	2.4 ±0.07	4
7D2N48KR4C	-25.78 ± 1.23	8.37 ± 0.31	3.02 ± 0.11	12
7D2N48KR4K	38.44 ± 1.94	10.51 ± 0.6	2.36 ± 0.15	3
7D2N48KR4S	-71.13 ± 1.48	5.91 ± 0.60	4.34 ± 0.4	4
7D2L112AM119V	1.08 ± 1.25	7.86 ± 0.87	2.60 ± 0.18	3
7D2R4KL112A	6.70 ± 1.48	9.14 ± 0.68	2.73 ± 0.20	2
7D2R4KT5K	-15.66 ± 2.62	7.79 ± 0.51	3.22 ± 0.22	3
7D2N25FR4KL112A*	21.92 ± 0.7	6.17 ± 0.86	4.11 ± 0.57	2
7D2N48KL112FM119V*	49.38 ± 2.06	6.85 ± 1.21	3.93 ± 0.84	3
7D2N48KL112AM119V	80.83 ± 3.98	10.14 ± 0.54	2.47 ± 0.12	4
7D2N48KR4KL112F	6.31 ± 9.95	10.10 ± 0.49	2.48 ± 0.12	6
7D2N48KR4KL112A	51.21 ± 5.67	8.34 ± 0.50	3.00 ± 0.18	3
7D2N48KR4KM119V	120.50 ± 1.79	11.26 ± 0.55	2.22 ± 0.11	3

The half maximal voltage, slope factor, and apparent charge movement. Mean ± SEM *data not shown

With combinatorial mutations, we succeeded in shifting the $V_{1/2}$ of activation almost 250 mV in this chimeric channel (Table 2, 6). Further investigations should measure the gating charge movement of N48K-R4K-M119V, the triple mutant with the largest shift, as an important next step towards understanding the movement of the VSD that translates to such a large effect on the voltage-dependent activation of this channel.

We have demonstrated that the shifts in voltage-dependent gating caused by an array of VSD residue substitutions are also observed in ion channels that span a large range of evolutionary space. Combinations of these substitutions produced channels with a wide range of voltage sensitivities, and this information could be used to develop methods of dialing in a desired voltage sensitivity in a potentially broad field of ion channels. The creation of a toolkit of this nature may enhance the development of state-specific drug screens, expand the possibilities of synthetic biology, and it can be utilized to stabilize specific voltage-dependent conformational states in structural biology. We focused on the latter as an application of the above findings.

Chapter 5. STABILIZING THE RESTING STATE AND DETERMINING ITS STRUCTURE

5.1 BACKGROUND

Since the combination of N48K, L112A, and M119V caused a substantial positive-shift in the voltage-dependence of activation of the human bacterial chimera Na$_V$Ab-7DII, these same mutations (KAV) were introduced into the background of the fully bacterial channel Na$_V$Ab with three aims in mind. First, I wished to determine whether these mutations would be sufficient to shift the voltage dependence of activation of Na$_V$Ab. Second, I used these constructs to make a more complete characterization of gating currents in a truncated Na$_V$Ab channel because higher expression allowed more accurate determination of gating currents. Third, I collaborated with colleagues to use these mutations to aid in stabilization of the resting state for structural determination. The effects of the KAV mutations on the background of NaVAb were first investigated to verify that the effect was not specific to the 7DII chimera.

5.2 MUTATIONS SHIFTING VOLTAGE DEPENDENCE OF ACTIVATION OF IN NA$_V$AB

The KAV substitutions shifted the voltage-dependence of activation substantially on the Na$_V$Ab background (Figure 5.1). The N48/49K mutation alone caused roughly a 75 mV shift in the voltage dependence of activation in both backgrounds. Na$_V$Ab KAV is positively-shifted compared WT, with a $V_{1/2}$ of +60 mV (Table 6). The shift caused by the addition of “AV” to N49K, however, did not produce a voltage shift of the same magnitude as in 7DII (81 vs 120 mV, respectively) (Figure 5.1).

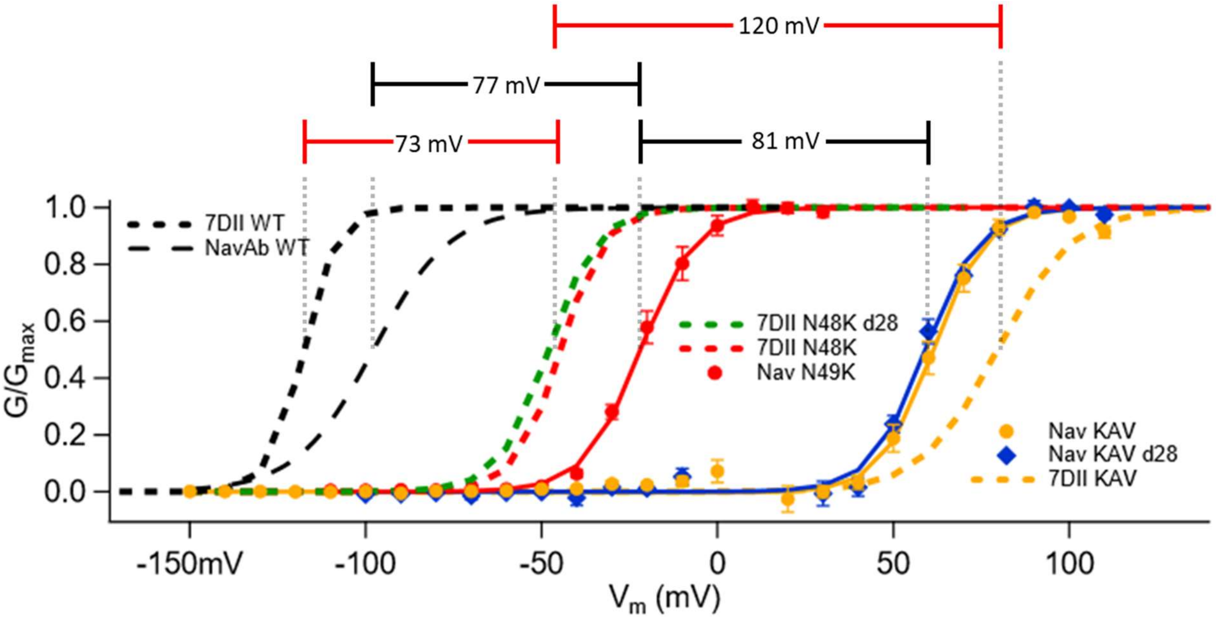

Figure 5.1 Comparison of the effects of KAV mutations on $V_{1/2}$ in Na$_V$Ab and 7DII.
Below- G/V relationships of each of the constructs studied. NavAb was not tested for individual contributions of residue substitutions. The KAV mutations were introduced into the full length channel was studied as well as a 28 residues (d28) c-terminal truncation. Above – a comparison of the magnitude of voltage shifts in the activation $V_{1/2}$ produced by the addition of N48/49K and the L112A-M119V in addition. On the left is the contribution of N48/49K alone, and on the right the contribution of AV on the N48/49K. Black bars measure the shifts in $V_{1/2}$ for the Na$_V$Ab background, and red indicates 7DII.

5.3 DISULFIDE LOCKING THE RESTING STATE OF NA$_V$AB

When the KAV residues were placed into Na$_V$Ab, a cysteine scan of the S3-S4 linker revealed that different residues were interacting with the outside of the pore adjacent to the VSD in the KAV mutant compared to WT or N49K alone. By utilizing the domain- swapped nature of sodium channels, we could crosslink a residue on the S4 to Q150C on the S5 of the neighboring subunit. Q150 faces the VSD and interacts with the V100 in the activated structure of the channel. When run on a western blot, monomers crosslinked together in this way would appear as higher molecular weight band on an SDS PAGE gel, and if bands four times the molecular weight of the monomer are seen in abundance for a given S4 cystine substitution, it will give clues as to the position of the S4 along the gating pathway at 0 mV. V100 and Q150 readily crosslink and migrate as tetramers on the background of Na$_V$Ab WT (data not shown) and N49K. When KAV was present instead, the residue that preferentially crosslinked with Q150C was G94C (Figure 5.2.B), which is a full two helical turns away from V100 out on the S3-S4 linker (Figure 5.2.A and C). We believed that this could only occur if the S4 was naturally occupying a resting state at 0 mV, and therefore KAV must be stabilizing the voltage sensor in a conformation where the S4 has not moved much if at all from the resting state.

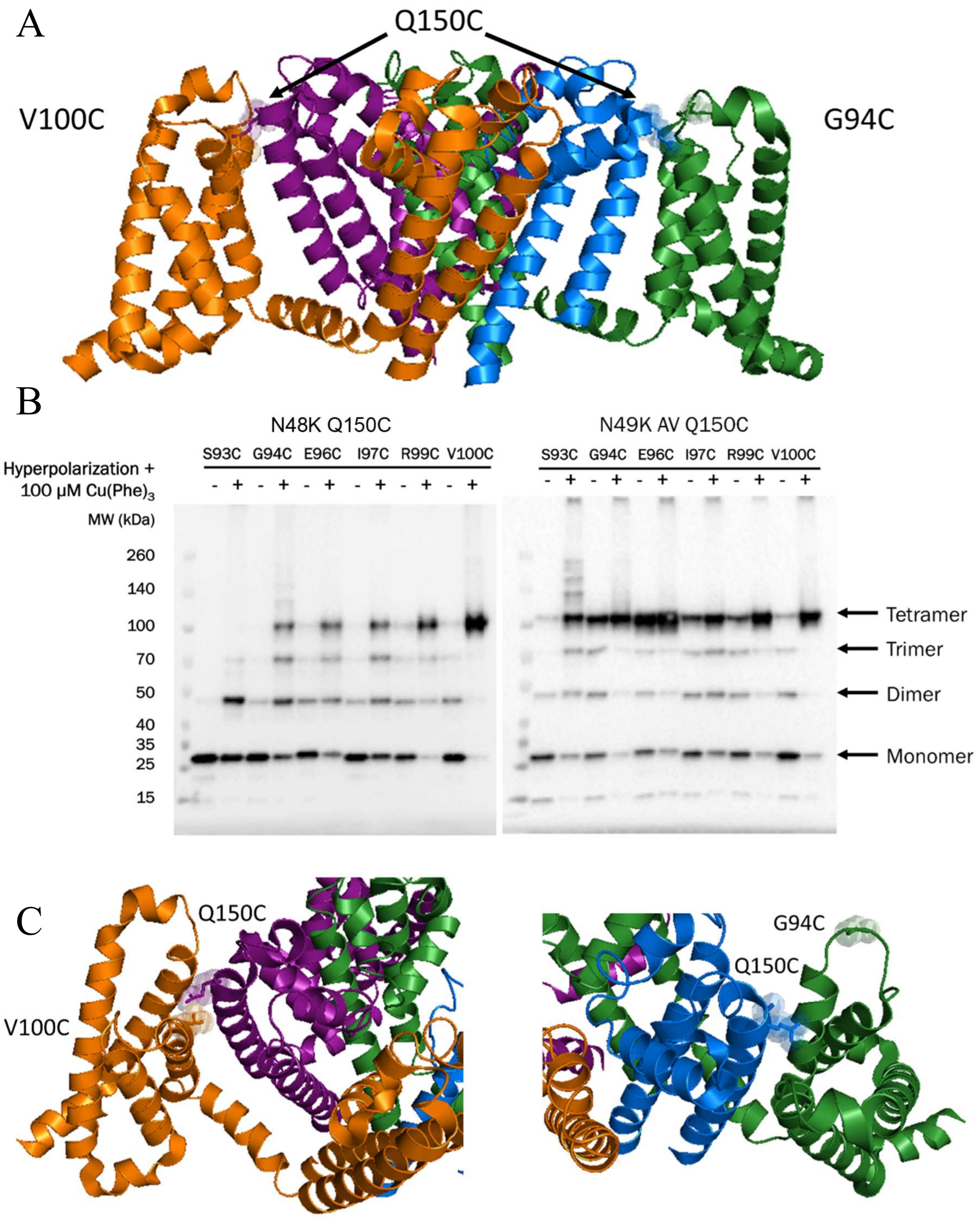

Figure 5.2 Intersubunit disulfide crosslinking of the VSD of Na$_V$Ab.

The crosslinking of one subunit of Na$_V$Ab to its domain swapped neighbor allows for visualization of crosslinking efficiency by western blot as evidenced by the amount of tetramer visible on SDS PAGE compared to total signal. A) side view of Na$_V$Ab indicating the location of two residues, V100C and G94C on the S4, that crosslink to a third, Q150C on the S5, in the active and resting state, respectively. B) Western blots showing the amount of stable tetramers formed by disulfide crosslinking. When the channel only contains the N49K mutation, residues on the more extracellular side of the S4 tend to crosslink, even when the membrane is hyperpolarized by copper phenanthroline. When the AV residues are added, a clear external shift is seen in the location of the residues that crosslink, supporting the conclusion that the S4 is moving inward more, and thus these residues are coming in close enough contact to crosslink. C) Top view of A.

It was possible that substitution of these two residues, G94 and Q100, for cysteines may cause the channel to adopt an unnatural conformation, especially if the native residues serve an integral structural purpose. One way to estimate the likelihood that a specific residue is important for normal protein function is to calculate the conservation score of that residue when compared across similar proteins from many organisms.

Using Na$_V$Ab as bait, a pblast search confined to the Prokaryota kingdom was used to generate a multiple sequence alignment (MSA) of voltage sensitive channels with a hit score above 95%. The alignment was modified to remove gaps and only compare residues that are present in Na$_V$Ab for easy interpretation, and a weblogo was created to visualize the relative abundance of different amino acids at equivalent positions in Na$_V$Ab. The results indicated that G94 and Q150 are not well conserved among prokaryotic ion channels (Figure 5.3.A). A subsequent search with broader parameters examined a vast evolutionary space to create a similar MSA and weblogo (Gamal El-Din et al., 2013), and it was still evident that these residues are not conserved (Figure 5.3 B).

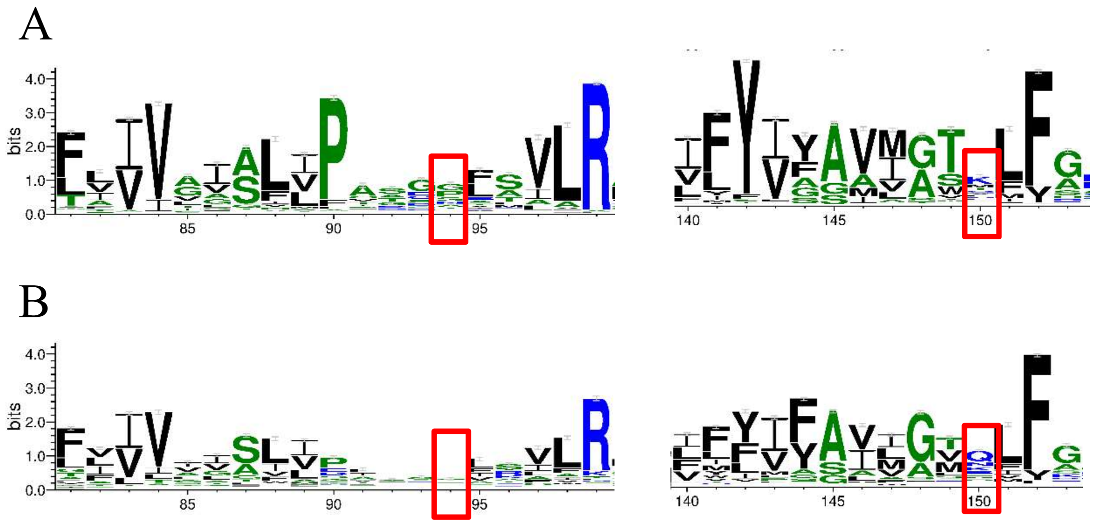

Figure 5.3 G94 and Q150 are not well conserved.

A) – sequence conservation information shown in a logo format for the aligned sequences found in a pblast search using Na$_V$Ab as bait and limiting it to sequences from Bacteria and Archea. B) same as above, except the aligned sequences came from a search of the large GREMLIN metagenomic database provided by David Baker's Lab. Red boxes encircle G94 to the left and Q150 to the right.

5.4 Functional Properties of Na$_V$Ab Constructs Used for Structure Determination

In order to achieve expression levels high enough for good recordings, the d28 truncation mutation was added to the channel, as this has been anecdotally found in the lab to drastically increase the current density of transfected cells. It is not known if this is due to a change in trafficking, a post-translational modification, or an increase in the single channel conductance. A comparison of truncated and full length KAV and KAV/Q150C channels was possible because they had better expression than those containing G94C. There was no difference in the voltage-dependent properties of activation of the channel between full length and truncated channels (Figure 5.4).

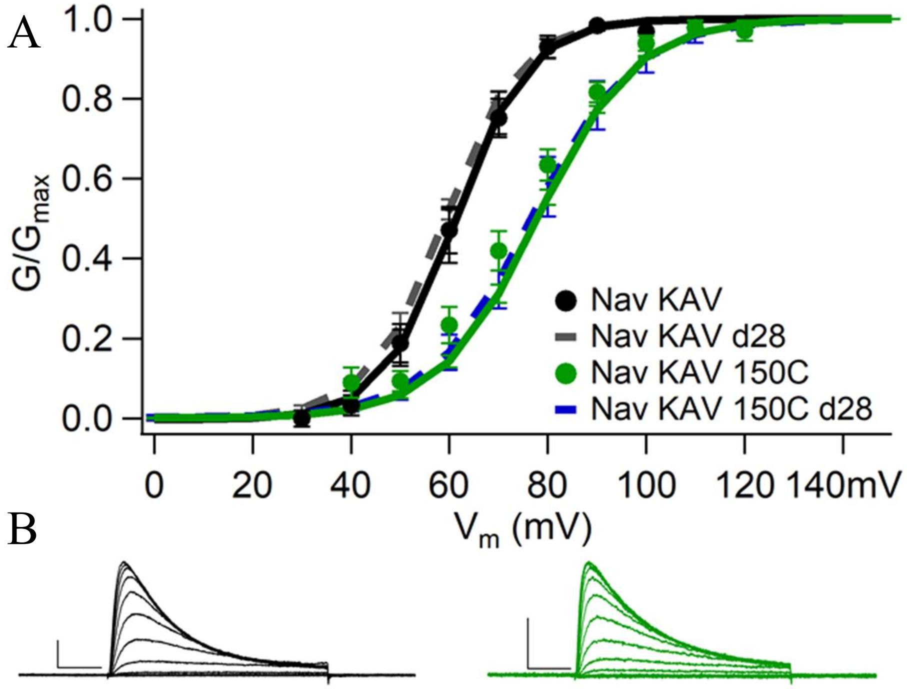

Figure 5.4 The truncation mutation Δ28 has no effect on KAV activation gating.

(A) Normalized conductance-voltage (G/V) relationships and Boltzmann fits for full-length (FL) compared to C-terminal truncated (Δ28) channels. Due to decreased current density in cells expressing channels containing G94C, the C-terminal truncation mutation Δ28 was added to all constructs for electrophysiological recordings to increase total signal, Dashed (FL) and solid (Δ28) curves = 1/(1+e^(($V_{1/2}$-Vm)/k)). Half activation ($V_{1/2}$) and slope (k) values are averages of individual fits. Data points within 15 mV of Vrev were omitted to reduce noise. Markers and error bars represent average G/Gmax ± SEM. (B) Representative current families of Na$_V$Ab/KAV (black) and Na$_V$Ab/KAV/Q150C (green) full length. Transiently transfected Sf9 cells were held at -150 mV and stimulated for 50 ms to depolarized voltages in 10 mV increments. Scale bars represent 10 msec x 1 nAmp.

Given that the native residues are not crucial to normal channel function, we were surprised to find that these substitutions caused further positive shifts in the voltage dependence of channel opening. The cysteine mutations pushed the $V_{1/2}$ of the G/V curve to even more positive values than KAV alone (Figure 5.5): G94C and Q150C shifted the voltage dependence of activation of Na$_V$Ab/KAV positively to $V_{1/2}$ = +88 mV and +77 mV, respectively. The double mutant in reducing conditions exhibited a total shift from WT of 203 mV to a $V_{1/2}$ of +106. Importantly, the channels do not open at 0 mV, but the question of whether their voltage sensors have moved at that point remained to be addressed.

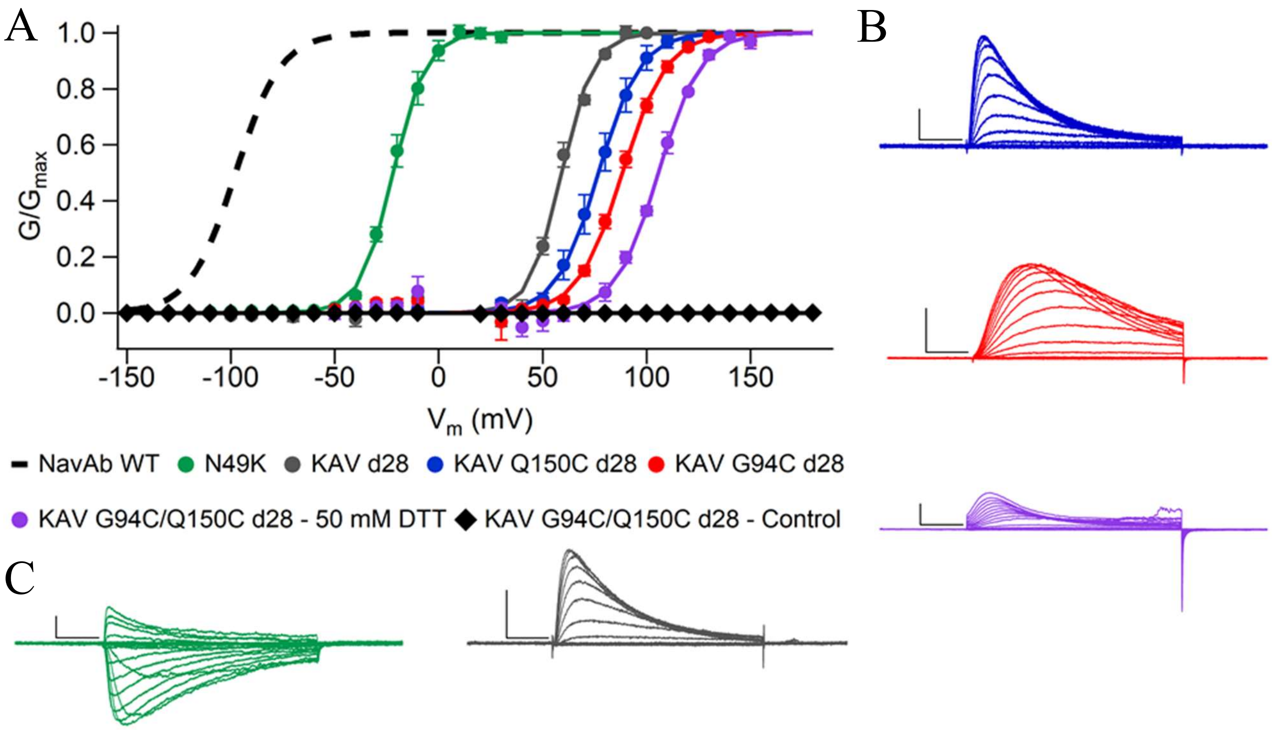

Figure 5.5 Single and double cysteine substitutions on the Na$_V$Ab/KAV background.
A) Normalized conductance-voltage (G/V) relationships and Boltzmann fits for each mutant. Sf9 cells expressing Na$_V$Ab KAV Δ28 mutants were stimulated with 50 ms pulses from 0-150 mV in 10 mV increments from a holding potential of -150 mV. Markers and error bars represent average G/Gmax ± standard error of the mean (SEM). Half activation ($V_{1/2}$) and slope (k) values are averages of individual fits ± SEM. Curves = 1/(1+e^(($V_{1/2}$-Vm)/k)). Data points within 15 mV of Vrev were omitted to reduce noise. B and C) Representative current families of the above named constructs in corresponding colors.

Table 7 - Activation parameters of Na_VAb N49K and KAV constructs

Na_VAb	Act $V_{1/2}$	k	z_{app}	n
N49K	-21.83 ± 1.78	7.88 ± 0.96	3.23 ± 0.32	4
KAV	61.28 ± 2.08	7.21 ± 0.43	3.44 ± 0.22	3
KAV d28	59.15 ± 0.82	7.69 ± 0.77	3.26 ± 0.33	3
KAV G94C d28	88.37 ± 1.08	10.55 ± 0.42	2.34 ± 0.1	3
KAV Q150C	77.83 ± 0.84	9.87 ± 0.27	2.50 ± 0.71	3
KAV Q150C d28	76.83 ± 3.13	9.98 ± 0.86	2.50 ± 0.22	4
KAV G94C Q150C d28	105.67 ± 0.78	10.18 ± 0.24	2.42 ± 0.59	3

The half maximal voltage, slope factor, and apparent charge movement. Mean ± SEM

5.5 GATING CHARGE MOVEMENT IN CONSTRUCTS FOR STRUCTURE DETERMINATION

Add a few sentences of introduction here. By measuring the outward (On) movement of the S4 gating charges in response to incremental voltage increases from a very negative initial membrane potential, we determined that measurable charge movement did not occur until voltages above the putative resting membrane potential (-45 mV) in the VSD of Na_VAb KAV/G94C d28, while N49K d28 alone and KAV d28 showed significant movement at those voltages (Figure 5.6.A). The $V_{1/2}$ of the On Q/V curve for these constructs was, -83.1 mV for N48K d28, -21.5 mV for KAV d28, and +77.3 mV for KAV/G94C d28, representing a positive shift of 62 mV with the addition of the 'AV' mutations to N49K, and 99 mV for the subsequent addition of G94C, for a total Q/V shift of 160 mV in the positive direction. For comparison, the same substitutions shifted the G/V curve by only 110 mV in total (Table 7). Thus, these results add an important element to interpretation of our structural data, because they show that both gating charge movement and channel activation are prevented at 0 mV in the cysteine mutants used for structural studies.

The Off gating charge movement occurred at lower potentials for all constructs, as is expected do to charge immobilization during inactivation. The $V_{1/2}$ of the Q/V curve for Na_VAb-N49K d28 was -152 mV, and the addition of ‘AV’ increased this by 77 mV to a $V_{1/2}$ of -75 mV. The further addition of G94C resulted in a 96 mV shift of the $V_{1/2}$ to +21.4 mV, representing a total shift of 173 mV. No gating charge movement was observed for KAV/G94C/Q150C (n=4, data not shown), which supports our findings that disulfide locking of G94C to Q150C prevents S4 translocation.

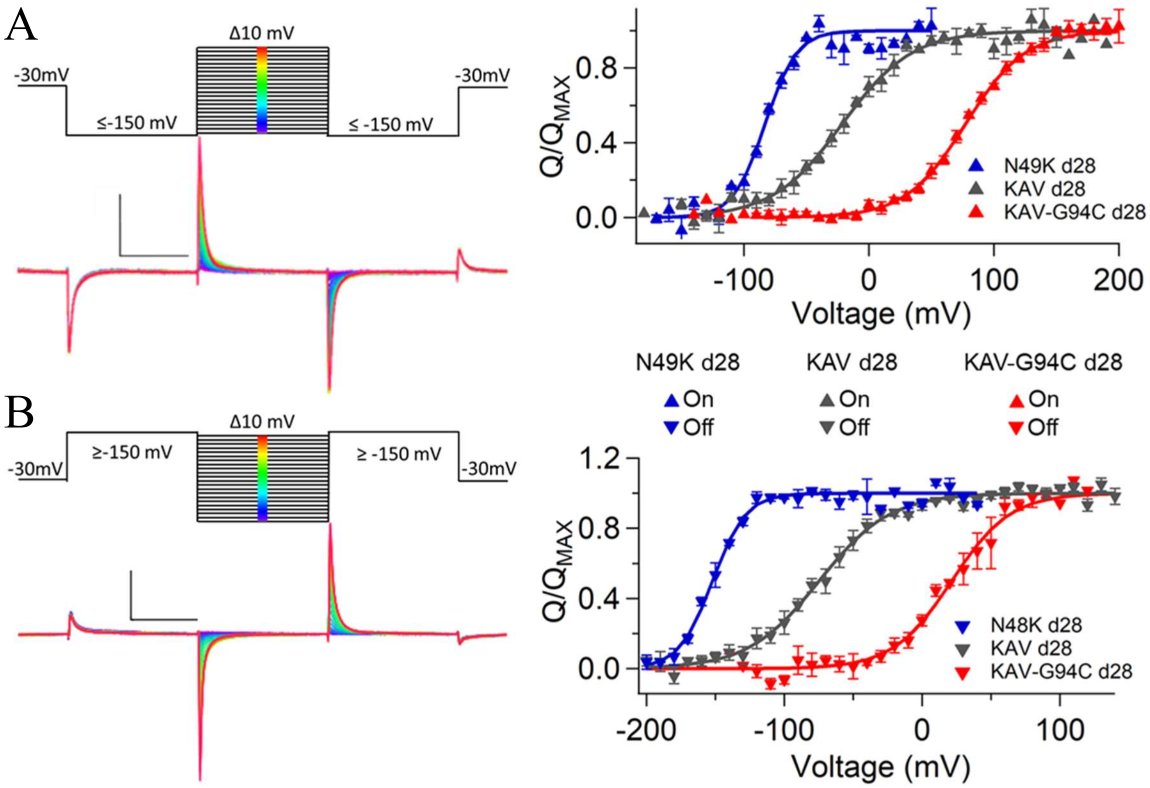

Figure 5.6 On and Off gating charge movement in Na$_V$Ab d28 constructs.

A) On charges in response to depolarization in media that contained NMDG-Cl substituted for Na-Cl and CaCl2. Cells were briefly hyperpolarized and then the subsequent current step was increased in 10 mV increments. B) Off gating charge movement in response to hyperpolarization following brief depolarization prepulse. A P/5 leak subtraction was used at voltages that remained well outside the range of charge movement, either very positive, or very negative. The area under the curve was calculated and plotted as a function of voltage. To the right of each are voltage protocols and representative traces of NavKAV d28 that were baseline corrected to the current remaining at the end of the pulse.

Table 8 – On and Off gating charge parameters of Na_VAb K49K and KAV mutants

Mutant	On $V_{1/2}$	k	z_{app}	n
N49K d28	-83.09 ± 0.74	12.54 ± 0.07	1.96 0.01	2
KAV d28	-21.46 ± 3.67	27.76 ± 2.5	0.91 0.85	4
KAV G94C	77.25 ± 0.39	23.69 ± 2.27	1.07 ± 0.11	4
	Off $V_{1/2}$	k	z_{app}	n
N49K d28	-152.09 ± 0.63	12.14 ± 0.5	2.03 0.01	2
KAV d28	-74.72 ± 6.05	25.63 ± 2.13	0.98 0.08	4
KAV G94C	21.43 ± 3.30	21.14 ± 3.78	1.46 ± 0.27	3
KAV Q150C*	-54.03 ± 4.74	37.62 ± 4.09	0.66 ± 0.7	2

The half maximal voltage, slope factor, and apparent charge movement. Mean ± SEM *data not shown

The slope factors for the two-state Boltzmann fits of the On gating currents were 12.6, 27.8, and 23.7, for Na_VAb N49K, KAV, and KAV- G94C, respectively (Table 8). This corresponds to the movement of roughly 2 gating charges per monomer for N49K and 1 for the KAV constructs. While it is possible that a single gating charge in KAV moves at potential too negative to measure, the structural information described in the next section conflicts with this conclusion. Two gating charges clearly move through the hydrophobic constriction site in the activated versus resting VSD structure.

While the leading theory for many years stated that voltage sensors move all of their charges in a single "shot" movement across the membrane electric field (Bezanilla and Stefani, 1994; Chanda and Bezanilla, 2002), the knowledge of the structure of the VSD along with careful mutagenesis studies around the gating charge permeation pathway has called this assumption into question (Lacroix et al., 2012). Structurally, the existence of several gating charges, negative clusters, and hydrophobic barriers to overcome has led to a colloquial description of sequential gating charges moving one helical turn up or down as moving one "click". In contrast to his earlier methods, Francisco Bezanila, one of the first to ever study gating charge movement, now warns that a two-state Boltzmann can often be well-fit to Q/V data representing multiple transitions, and using the slope value of the fit to calculate the total number of charges moved during the gating transition can lead to an underestimation by a factor of as great as 4 (Bezanilla & Villalba-Galea, 2013) if the same number of charges move in each transition. For this reason, as we have surely impeded the progress of the gating charges through the sensor, it may be reasonable to predict multiple states of transition exist in the KAV constructs and therefore $z = 1$ is an underestimate of the total charge moved per VSD.

5.6 STRUCTURAL DETERMINATION OF THE RESTING STATE OF NA$_V$AB

The Na$_V$Ab KAV-G94C-Q150C channel would not form crystals despite a large screen of crystallization conditions, suggesting that the channel is in a drastically different conformation than the WT channel. The logical next step to obtain structural information about the construct was cryo-electron microscopy (cryo-EM). Na$_V$Ab alone is too small for the technique to be used because the signal to noise ratio would be too low when analyzing images and trying to locate individual channel particles. By creating a channel whose n-terminus is fused to the C-terminal alpha helix of maltose binding protein (MBP), the molecular weight of the protein was increased from 130 to 290 kDa, and the particles of purified protein were large enough for cryo-EM structural determination.

We were able to refine the structure of the crosslinked resting state of Na$_V$Ab KAV-G94C-Q150C to an average resolution of 3.9 Å. In the pore region, the resolution of the map is between 3.0 and 3.9 Å, and the S3, S4, and S4-S5 linker has a resolution of 3.9 Å or better. The density map of the S1 and S2, however, has a resolution between 4-5 Å, so there are limitations to what information can be accurately gained from an examination of the potential structural mechanism of the N25F and N49K effects on voltage-shifting as they reside on those segments. The biochemistry and structural data collection and processing were carried out by George Wisedchaisri and Lige Tonggu.

Three distinct structural changes were observed when comparing the resting state to the activated state of Na_VAb: the S3-S4 linker and extracellular portion of the S4 form a new fold, the S4 moves inward by 11.5 Å, and the S4-S5 linker forms an acute angled bend at the bottom of the pore.

When the S4 moves intracellularly in the resting state, the S3-S4 extracellular loop is pulled down, and part of it becomes the n-terminal segment of the resting S4. This process narrows the extracellular aqueous cleft that is created by the extracellular VSD linkers, and the potential binding site for voltage-modifying toxins and drugs undergoes a rearrangement which would create new interfaces and opportunities for resting-state specific binding while simultaneously eliminating potential interfaces that created high-affinity interactions between ligands and the activated VSD.

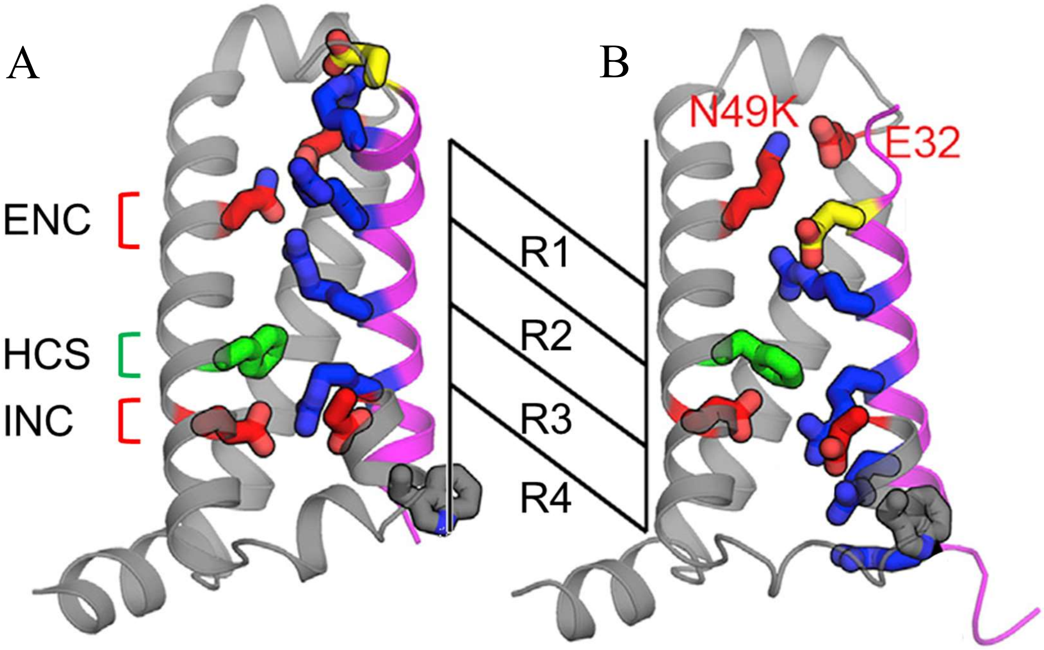

Figure 5.7 Rearrangement of gating charges during the VSD activation transition
Adapted from (Wisedchaisri et al., 2019). The extracellular negative cluster (ENC) including N49K and E32 and the intracellular negative cluster (INC) residues are shown in red, while the hydrophobic constriction site phenylalanine is shown in green. E96 is shown in yellow. Gating charges are in blue along the S4 which is bright purple.

The S4 helix adopts a 3_{10} conformation in the resting state that spans 5 helical turns from G94C to R108 (R4), which results in E96, R99 (R1), R102 (R2), R105 (R3), and R109 (R4) being situated in a line along the same face of the S4 helix for the span of the VSD pore. The phenylalanine which forms the HCS is located between R1 and R2 as compared to its position between R3 and R4 in the activated conformation (Figure 5.7). This means that two gating charges have fully traversed the membrane electric field by passing completely through the HCS during VSD activation. R2 and R3 form charge-pair interactions with E59 and E80, respectively, in the INC, which translates to two “clicks” of the S4, or a total of 11.5 Å linear inward movement between the activated and resting states.

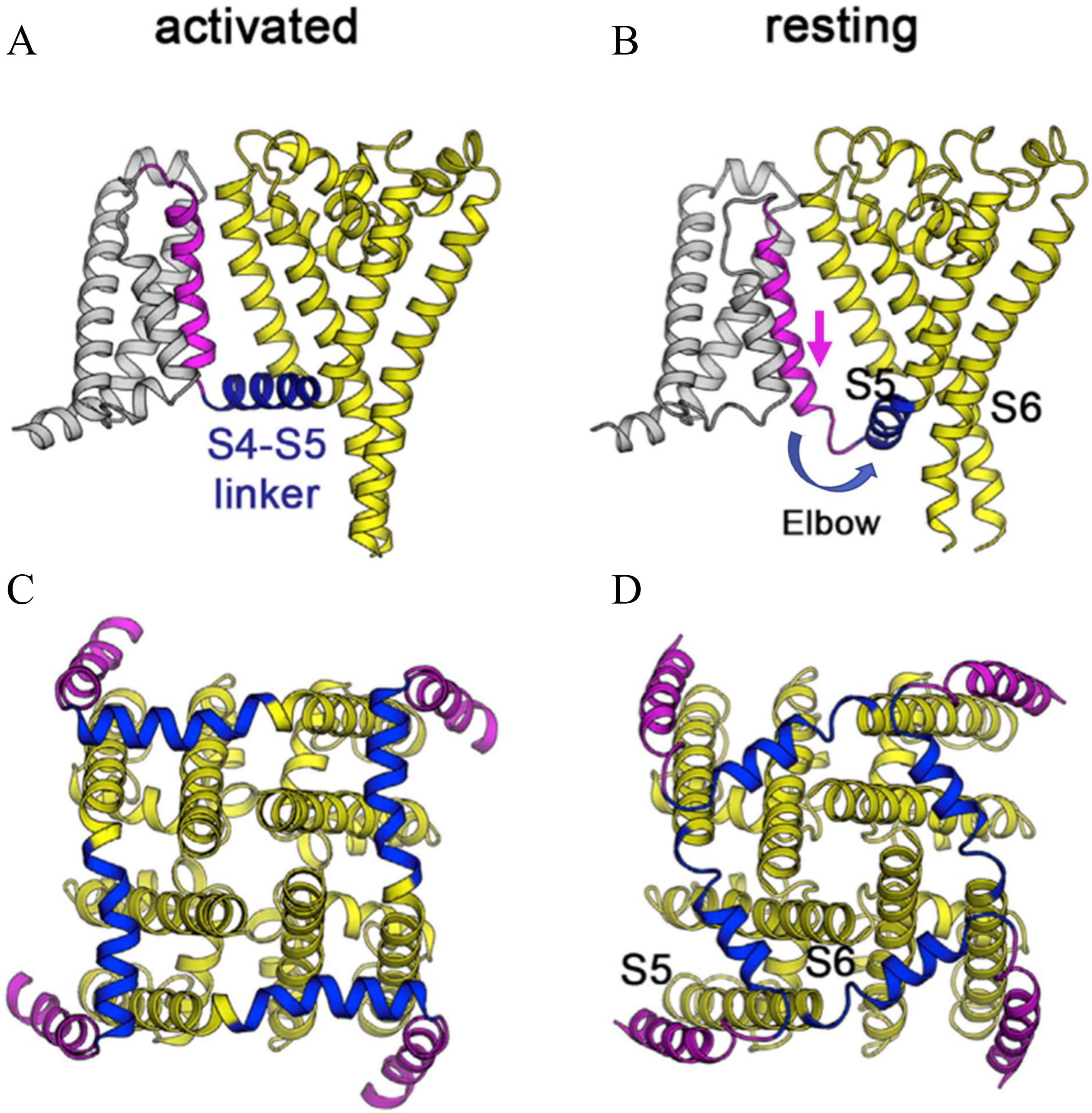

Figure 5.8 Conformational changes of the S4-S5 linker during VSD activation
Adapted from (Wisedchaisri et al., 2019) A and B) One subunit is shown with the VSD in gray and the pore in yellow. The S4 segment is colored bright purple and the S4-S5 linker is blue.

With the S4 protruding this far into the cytoplasm of the cell, the S4-S5 linker undergoes a conformational change wherein it angles down and towards the neck of the pore like an “elbow”.

The effect of all four S4-S5 linkers adopting this conformation is a constriction of the pore by forming a tight collar around the S6 helices, and this prevents the opening of the activation gate of the pore. This collar must be loosened by outward movement of the S4 before the bottom of the pore could open wide enough to allow ions to pass through. We are unable to determine if the resting VSD and S4-S5 linker physically pushes the pore closed with the aid of negative voltage or if the activation of the VSD pulls it open through a favorable association. If the S4 and S4-S5 linker are holding a pore closed at rest that otherwise would be open on its own due to steric forces inside the pore, the extremely rapid gating that occurs during sodium channel activation could be due to both voltage-sensitive S4 movement and the facilitation of that movement by the outward force of the pore opening.

Although precise measurements can't be made due to the limits of the resolution in these areas, in our resting state structure, K49 may be close enough to form a salt bridge with E32 as was seen in the N49K-containing activated state structure (Irie et al., 2018). The S1 and S2 backbone carbons to not vary significantly between our resting and activated states, but the S3 tilts slightly in the direction of the S4. In the model the distances between the K49 amine and the E32 oxygen are 3.1, 3.2, 3.7, and 4.4 Å in the four subunits as compared to 2.7 Å in $\mathrm{Na_VAb}$-N49K (PDB: 5YUC). There were no differences between subunits in residues on or proximal to the S4-S5 linker. It is not unreasonable to predict that the interaction between K49 and E32 remains between this pair of residues in the resting state, but this cannot be said conclusively. There are no other charged residues on the S4 or S3-S4 linker in proximity on to either K49 or E32 in the resting state, as R1 is two helical turns down from its activated position, a total displacement of 11.5 Å.

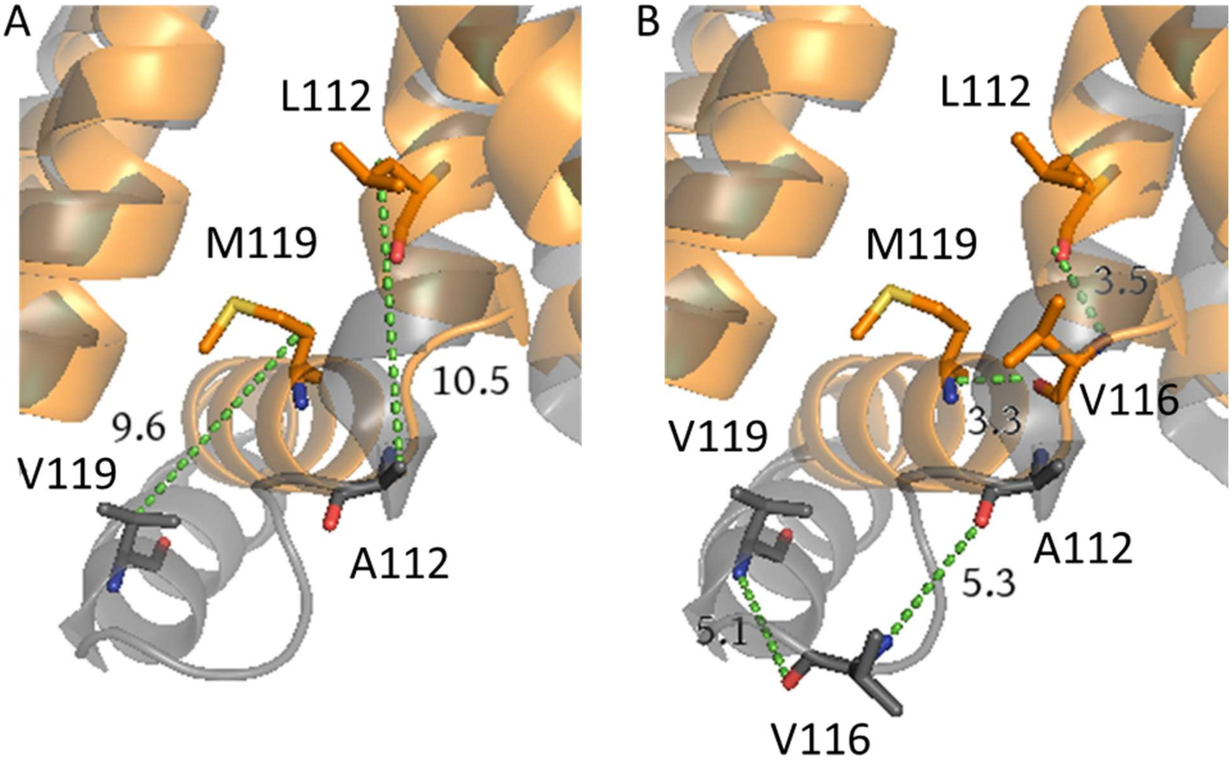

Figure 5.9 Structural environment of positions 112 and 119 in active and resting VSD
A) The distance in angstroms of the alpha carbon displacement between the resting KAV (Grey, PDB:6P6W) and activated state (Orange, PDB:5YUC) of the S4-S5 linker. B) Interaction of these two positions with the intermediate V116. Numbering is based on 7DII for easier comparison with the above work in the chimeras. Measurements were made in PyMol. Hydrogen bonding was predicted by the software.

When examining the changes that occurred at the mutated residues L112A and M119V (using 7DII numbering for easy association with the previous chapters) at the level of the S4-S5 linker in the two states, we see that the alpha carbon of L112 moves intracellularly by 10.5 Å. This decrease in the total movement compared to that of R1 is likely due to a relaxation of the 3_{10} helix to an alpha helix at the bottom of the S4. The M119 alpha carbon moves a total of 9.6 Å, and this decrease is expected due to the “elbow” movement of the S4-S5 linker to constrict the pore (Figure 5.9.A).

The structural interactions that these residues make is also altered in this transition. In the activated VSD, the L112 backbone carbonyl forms a hydrogen bond with V116 below it. The backbone amine group of M119 hydrogen bonds to the carbonyl of that same residue V116, and these interactions may serve to stabilize the rigid right-angle position of the "elbow" when it is up (Figure 5.9.B). In the resting state, the backbone amines and carbonyls of these three residues are too far apart to hydrogen bond due to the stretched nature of the S4 near the elbow (Figure 5.9.B). In this resting orientation, however, the backbone carbonyl of A112 and the amine of V119 are free to stabilize the end of the alpha helices which they are immediately adjacent to.

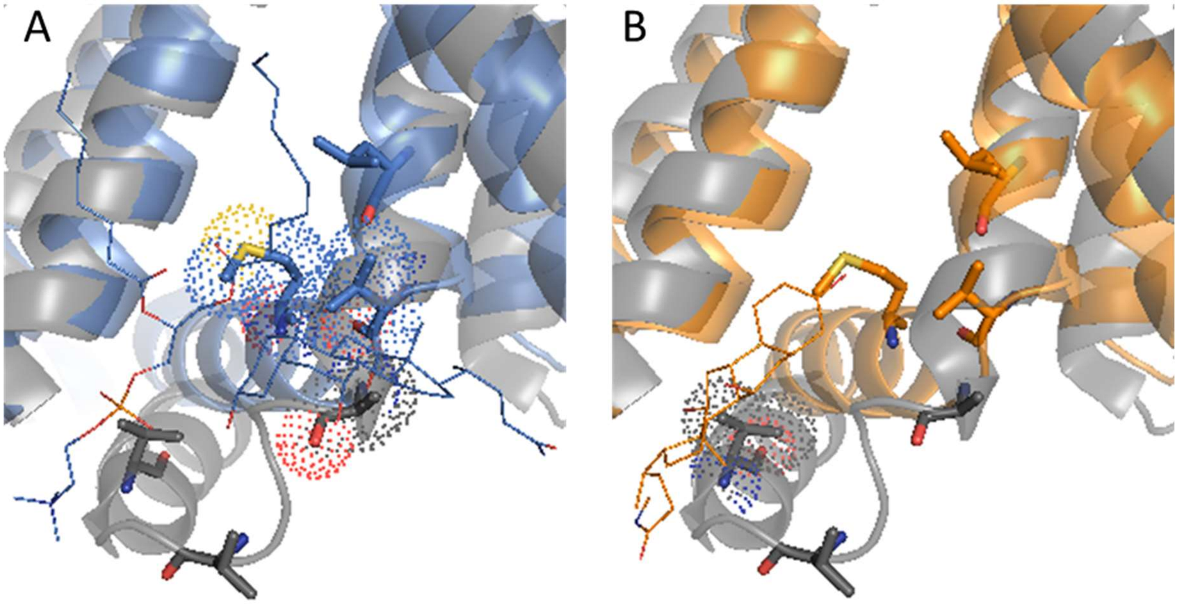

Figure 5.10 Potential lipid environment of the S4-S5 linker

A) One lipid and one CHAPS molecules present in the activated (reduced) Na_VAb V94C/Q150C crystal structure (Blue lines, PDB: 6P6X) are within 4 angstroms of the S4-S5 liker. The resting state structure is overlaid in Grey (6P9W). B) One CHAPSO molecule is present near the S4-S5 linker in the activated Na_VAb N49K (Orange lines, 5YUC) structure. All residues from the previous figure are shown, and dots surrounding them indicate a 4 Å proximity to lipid or detergent. More residues are in this proximity range, but only the three discussed above, at positions 112, 116 and 119 (sticks) are examined. These residues overlap completely when the 6P6X and 5YUC are overlaid. Proximity was determined using the "around" function in PyMol limited to 4 Å.

The R groups of the mutations themselves may not contribute significantly to this interaction between the backbone residues, which leaves little explanation for how L112A and M119V can have such a drastic effect on gating. The R groups are hydrophobic, however, so a reasonable explanation for the effects of the L112A and M119V mutations may then be favorable interactions with lipids near the S4-S5 linker which serves to reinforce the inward push of the S4-S5 linker 'elbow' into the base of the pore. Lipid and detergent densities around the S4-S5 linker could be resolved in our crystal structure of Na$_V$Ab-G94C-Q150C in reducing conditions, and a single detergent molecule is also found near this structure in the N49K activated structure (5YUC; Irie et al., 2018).

When the structures are overlaid, and residues within 4 Å of a specific lipid or detergent molecule are highlighted, we are able to investigate any Van der Waals interactions are occurring with them. While several residues in the area are capable these interactions, we focus on those made with positions 112, 119, and 116 in the activated and resting states. We do not have information about the densities of lipids or detergents in the resting state structure, and as this examination cannot account for their movement after the transition to rest, potential interactions with these residues are identified under the assumption that the lipid and detergent molecules have not moved. In the G94C/Q150C activated structure, M119 and V116 interact with the lipid, but not the CHAPS molecule (Blue, Figure 5.10.A), while A112 potentially interacts with both molecules in the resting state (Grey, Figure 5.10.A). When comparing the resting state to 5YUC, of the residues of interest, only V119 in the resting state is close enough to potentially interact as it swings down in response to hyperpolarization.

More structures with high resolution models that include lipids are needed to investigate these interactions in greater detail. The detergent molecules are only an approximation of the potential position of lipids that would be present near the protein in the plasma membrane. Many ion channels are modulated by the presence of specific lipids in well conserved pockets of the protein transmembrane regions (Poveda et al., 2014), and be they interactions with head groups on the intracellular surface or hydrophobic tails, the residues of the amphipathic S4-S5 linker helix and the intracellular side of the S4 are certainly interacting with phospholipid components in the gating process, and mutations that alter these interactions could impact the ease with which the S4 exits the VSD pore into the cytoplasmic side of the membrane and pulls the S4-S5 linker with it.

5.7 SUMMARY

Through the course of this project, we were able to alter the properties of a sodium channel VSD such that it moves in response to voltage changes across a wide range of voltages. By shifting the voltage dependence activation in this manner, the channel could be used a means to better understand the structural features that control voltage sensing. A combination of mutations (KAV) were shown to drastically shift the voltage dependence of S4 movement, and when coupled with the substituted pair of cysteines G94C/Q150C, stabilized the resting state of the channel and led to a cryo-EM structure at 3.9 Å resolution. Without the positive-shifting KAV mutations, crosslinking between these two cysteine residues does not occur, and an activated state is instead captured in the crystal structure of G94C/Q150C alone (Wisedchaisri et al., 2019). This finding marks a momentous step forward in our understanding of the structural basis of voltage-sensing, and the field of ion channel study will have much work to do to make the most of its interpretation.

Chapter 6. DISCUSSION

6.1 COMPARISON TO EXISTING STRUCTURES

Our structure shows the full transition of two gating charges through the hydrophobic constriction site, whereas recent structures of domain II chimeras bound to gating modifier toxins show one full transition and one partial movement of the gating charges through the hydrophobic constriction site (Clairfeuille et. al., 2019; Xu et.al., 2019). Structural information provided by the ProToxin-II- bound structure reveals a mechanism for the high apparent affinity of this toxin to the channel by a state-independent association of several tryptophan residues with the plasma membrane, anchoring it nearby at the ready to bind once the resting VSD binding site is revealed. The information provided by the details of these target-ligand interactions - which are strong enough to hold the VSD in a deactivated state despite strong resistance from the S4 - will surely prove valuable for future drug design.

Importantly, these toxin binding studies provide clues as to a stable intermediate state that the toxin is able to trap. Holding the channel in this conformation prevents activation of the VSD at physiological potentials. This will help to understand how the energetic landscape of the VSD changes upon depolarization of the membrane, and it may provide clues as to low energy transition states can be stabilized with drugs to achieve a particular functional outcome of the channel.

Some information was previously known about the structural basis of voltage-shifting mutations in Na_VAb (Gamal El-Din et al., 2013), and our work builds on this knowledge. Irie et al studied the structural differences between Na_VAb WT, N49K, and E32Q in higher pH conditions than the original crystal structures, but the pH (8.2 vs 4.5) did not alter the VSD structure on its own. These two residues are highly conserved in prokaryotes, and both are defined as residues included in the extracellular negative cluster (ENC). In NavAb WT, N49 on

S2 is close enough to hydrogen bond with R3, and that interaction is eliminated when the residue is substituted for a lysine, as K49 forms a salt bridge with the negative residue E32 on S1, thereby sequestering both residues away from the gating charges.

In the WT structure, E32 forms a weak salt bridge with R1, and when it is mutated to a glutamine, it no longer interacts with any gating charges, but N49 maintains its association with R3. The overall result of the N49K mutation was interpreted to be an energetic separation of the S1 and S2 from the S4 helix, causing the VSD to require a larger depolarization to activate. This agrees well with Gamal El Din et al (2103) which finds that interactions between N49 and R3 are important for late slow inactivation. When that interaction is abolished by the N49K substitution, stabilization of the pore could occur, thereby preventing the asymmetrical collapse seen in the crystal structure of the inactivated state vs the pre-open state where N49 is further away from R3. Physical separation of R3 and N49 would naturally also occur upon hyperpolarization when the S4 is pulled fully downward, and the resulting elimination of inactivation at rest could be due to a similar stabilization of the pore.

It is possible that a holding potential of -180 mV is not enough to pull R3 far enough away from N49 to allow this stabilization in NavAb WT. Electrophysiological recordings that accompanied the N49K activated state showed that this late slow inactivation can be reversed completely with a sufficiently negative holding potential of -240 mV (Irie et. al., 2017). Even a short 100 ms prepulse to this potential was enough to restore the current of the channel completely upon subsequent stimulations. This brief pulse was necessary, as the insect cells in which the channels are expressed do not tolerate such negative membrane potentials for extended periods of time. It is reasonable to assume that *Archobacter butzleri* maintains a membrane potential of that magnitude, as many bacteria have very negative resting membrane potentials

(Hirota and Imae, 2011), and therefore it is unclear if the late slow inactivation is an artifact of insufficient holding potential producing steady-state inactivation through a closed-to-inactivated transition or incomplete recovery of previously opened channels from an inactivated state that was reached via a different energetic transition. It would appear, however that recovery from both inactivated states is possible when the S4 is sufficiently pulled down by hyperpolarization. See 6.4 for further discussion.

6.2 Implications for Pain Research and Treatment

Inflammatory mediators increase the persistent current through Na$_V$1.9 channels in pain fibers, which raises the resting membrane potential and causes hyperexcitability (Maingret et. al. 2008). This can lead to hyperalgesia and pain because it reduces the stimulus required to activate Na$_V$1.7 and subsequently Na$_V$1.8. This makes modification of the voltage-sensitive properties of the “threshold gate” Na$_V$1.7 a very attractive prospect for treatment of inflammatory pain. The potential success of resting-state stabilizing drugs targeting Na$_V$1.7 is increased because studies on resurgent currents have revealed that this channel already has a slow rate of transition from the closed to the inactivated state at intermediate voltages where it does not open (Cummings 1998), so it is reasonable to predict that weaker interactions between the voltage-sensor and a drug would be sufficient to further increase the energetic barrier between a resting and activated voltage sensor in this sodium channel isoform.

Structural information detailing the extracellular surface of VSDs in many intermediate positions along the gating transition pathway could inform countless in silico modeling and docking studies of potential drugs targeting sodium channel VSDs. By selectively employing combinations of these voltage dependence modifying point mutations coupled with disulfide locking, this structural information may be obtained. Further valuable information could be gained from structures of resting- and intermediate state VSD-chimeras with extracellular residues reproducing the environment of the voltage sensors in individual domains of specific sodium channel isoforms. This information has the potential to help in the discovery of highly selective sodium channel modifying drugs with a low probability of off-target effects.

New developments in assays used to screen for sodium channel modifiers in a high-throughput manner are now being utilized. These assays reduce the bias towards nonspecific pore-blocking drugs by eliminating the need calculate the drug binding affinity as a measure of the displacement of a radiolabeled pore blocking drug (Tay et al 2019 PLoS 1, Hai-bo Yu, acta pharmalogica 2015). The possibilities for treatment of a wide array of channelopathies, both inherited and induced, is a promising potential outcome of the results of this effort and other studies which are to come.

6.3 COVARIATION AND CONSERVED COMPONENTS OF VSDS

The diversity of voltage sensing domains that exist in nature evolved over millions of years, resulting in broad expression in both prokaryotes and eukaryotes. The multitude of VSDs found in these organisms also display diversity in tasks they perform for the purpose of cellular and organismal function (Zakon, 2012). Voltage-sensing phosphatases and proton channels contain only a single VSD. The former translates voltage-dependent movement into modulation of an intracellular phosphatase, and the latter contains a permeation path through the VSD to allow protons to pass in and out of the cell at certain voltages. A large multisequence alignment of over 6,000 diverse VSDs (Palovcak et al., 2014) provided a wealth of information about potential contributions of individual amino acids to the gating process. The calculated sequence conservation gives a measure of the necessity of certain amino acids in certain positions of the VSD, and quantification of the covariation of residues identified several potential residue interactions that are not shown to interact in structures of the activated state of the channel. This effectively predicted amino acid contacts of the channel in resting or intermediate states and provided possible interpretations of various experiments which studied the effect of point mutations on VSD function (Lacroix et al., 2014).

The covariation information serves to highlight interactions that are likely counterbalancing each other's effects. It is less likely that strongly covarying pairs of residues would be involved in the subtle differences in voltage-dependency found in the natural diversity of VSDs in different channels and in their individual domains. Interestingly, the two predicted residue interactions with the highest covariation scores were the interaction of both N25 and N49 with E96 in the S3-S4 linker, so it is reasonable to predict that the drastic changes in voltage sensation caused by the N25F and N49K mutations are due to the disruption of local environments in the VSD that are critical for its normal function. It is probable that the range of VSD voltage dependencies that occurs across evolutionary space was slowly expanded by the additive effects of small incremental changes that modified local environments of the VSD which were not critical for its overall function.

6.4 THEMES IN MUTATION EFFECTS

The effects of all the mutations studied here on VSD activation are due to shifts the energetic equilibrium of the channel which stabilizes the resting state at voltages where other conformations were previously more stable. It follows that such a stabilization of the resting state would lead to both a decrease in the necessary hyperpolarization required for voltage sensor deactivation as well as a positive shift in the voltage-dependence of activation, because less energy (in the form of a voltage potential difference across the membrane) must be supplied to the system to achieve the same effect when the resting state is energetically more favorable (Mannuzzu and Isacoff, 2000). Any mutation that eliminates an interaction which would have stabilized a closed or inactivated state would consequently allow the equilibrium of the VSD to shift so that residues involved in resting state stabilization will be favored, and thus more energy will be needed to destabilize these interactions and cause a structural change. This explains why the “late slow” or “late use-dependent” inactivation phenomenon has been seemingly abolished by every single mutation that positively-shifts the voltage dependence of activation of Na$_{v}$ab-7DII, as demonstrated by a lack of current decay in response to a 1 Hz stimulation to peak (data not shown). In essence, the rate of recovery from inactivation (or the rate of return to rest) will been enhanced by any mutation that destabilizes any other state at that membrane potential, provided it doesn’t preferentially stabilize a different inactivated state in the process.

Similarly, mutations that increase energetic barriers between states will also alter the transition rate, but if the energy well for one particular state is lower than the other, over time the equilibrium will favor most stable conformation. Lacroix et al 2014 provide a comprehensive model for how certain mutations alter the VSD movement by stabilization of various states or alterations in energetic barriers. They ascribe the effect of S240 (N25) substitutions as lowering the energy well of the resting state, and this translates to a Q/V curve that is not bimodal and where the $V_{1/2}$ is positively shifted compared to WT. Alternatively, a stepwise movement of the voltage sensor in the Q/V curve is caused by mutations that increase the energetic barrier at voltages where both the deactivated and activated states are similarly favorable (Lacroix et al., 2014).

N25F is one helical turn above the hydrophobic constriction site residue I22 in Na$_V$Ab, so its presence may serve to widen the concentrated membrane electric field in that area by extending the hydrophobic constriction site. Increasing the size of the hydrophobic plug would cause a decrease in the response of gating charges on the S4 because of a decrease in force placed by voltage across a less condensed electric field (Ramírez-SanJuan et al., 2013). Alternatively, if the strength of the hydrophobic constriction site is reinforced, potentially by pi-pi interactions of the aromatic residues, an additional physical impediment of the movement of the gating charges through the center of the VSD would be the cause of the shift. Mutagenesis studies revealed that in *Shaker B*, the size of the substituted residue at that position, and not the hydrophobicity, is the determining factor in the effect of mutations there.

Since N25 (S240) has such a strong covariation history with the charged residue E96 (R362) (Palovcak et al., 2014), and *Shaker B* has an arginine in that equivalent position, it calls into question what an interaction between a glutamic acid and an asparagine has in common with an interaction between a serine and an arginine. Do these two interactions serve the same purpose across voltage sensors globally? It would be very interesting to know if the N25F mutation has the same effect on the Q/V curve of Na$_V$ab as S240F has on the *Shaker B* potassium channel. Differences between the two could shed light on the potential residue interactions specific to each voltage sensor that determine its unique voltage sensitive properties, and similarities may illuminate global truths regarding voltage-sensor structure-function relationships.

6.5 ONGOING OPPORTUNITIES

The results of this project have provided insight into the mechanisms of voltage sensing and gating in voltage-gated sodium channels, and it has produced a set of tools in the form of sodium channels that activate over a wide range of voltages. The future applications are broad, as a new toolset has been developed which will allow for the stabilization, trapping, and structural determination of the intermediate states in the movement of the S4 during VSD activation. Visualizing the druggable surface of a voltage sensor as it completes its entire voltage sensing cycle could prove beneficial to countless *in silico* studies on drug binding. Designer voltage sensors could be used in synthetic biology to facilitate a multitude of cellular programs by creating molecular switches or all-or-nothing responses in a signaling cascade, which would be similar to if:elseif statements and do:while loops computer programming. The potential for new insight and therapeutics is enhanced by this work, and I am excited to see what the field makes of it.

Chapter 7. MATERIALS AND METHODS

7.1 CELL CULTURE

7.1.1 *Microbe strains*

E. coli GC10 competent cells were cultured at 37°C in LB medium supplemented with 100 μg/mL of ampicillin for pfastbacdual plasmid DNA extraction. For pIZT plasmid prep, GC10 cells were grown in low salt LB supplemented with 50 μg/mL Zeocin and cultured as above. *E. coli* BL21(DE3) was cultured in MagicMedia *E. coli* expression medium at 37°C for screening of disulfide-crossliking mutants. *E. coli* DH10Bac was cultured at 37°C in LB medium supplemented with 100 μg/ml of ampicillin for bacmid production.

7.1.2 *Cell lines*

Sf9 (*Spodoptera frugiperda*) insect cells were maintained in Grace's Insect Medium and supplemented with 10% FBS and penicillin/streptomycin at 27°C and passaged at 80-95% confluence for electrophysiology. Sf9 and Hi5 (*Trichoplusia ni*) insect cells were maintained and infected in Grace's Insect Medium supplemented with 7.5% FBS and glutamine/penicillin/streptomycin at 27°C for baculovirus production and protein expression, respectively.

7.1.3 *Baculovirus*

Baculovirus was made using the bac-2-bac system (Invitrogen), wherein the pfastbac2 plasmid containing the channel under the polyhedron promoter was first purified via miniprep from GC10 competent cells (Genesee).

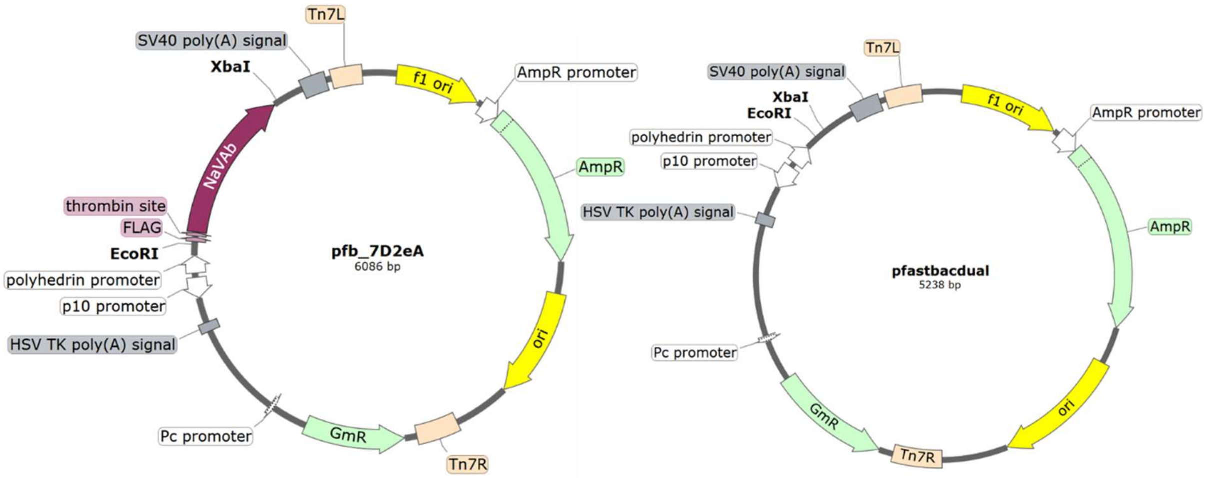

Figure 7.1. Plasmid maps of pfastbacdual before and after Flag_Na$_V$Ab insertion under the very late polyhedron promoter.

The vector backbone pfastbacdual was used to transform DH10Bac competent cells, which undergo a homologous exchange to incorporate the promoter and gene of interest into the viral genome. These were plated onto media containing ampicillin, gentamycin, and kanamycin as well as beta galactose. Colonies that appeared white were used to restreak additional plates to confirm that no blue colonies grew from the original clone. White colonies were then grown in LB containing ampicillin and the bacmid was purified and stored in TE.

To generate the virus, 90% confluent Sf9 cells in 6-well plates were transfected with 1ug of the purified bacmid using cellfectin II. After 48 hours, the supernatant was removed, spun for 5 min at 500g, and added to a 90% confluent 150 mm dish of Sf9 cells with all but 5 mL of media removed. These cells were rocked for 1 hour, rotating 90 degrees after 30 min, and 25 mL of media was added before incubation at 27C for 48 hours. At that time, the supernatants were collected and centrifuged as above to generate the stock of P2 baculovirus. 1 mL of P2 was added to each of two 150 mm dishes of 90% confluent Sf9 cells and rocked as above for one hour before additional media was added and the plates were placed in the incubator. Following a 36 hour incubation, the supernatant was collected and centrifuged as above to generate the stock of P3 baculovirus. Either P2 or P3 was used in experiments where Hi5 or Sf9 cells were infected to produce channels for either electrophysiology or protein purification, as indicated in the results.

7.2 TRANSIENT TRANSFECTION FOR ELECTROPHYSIOLOGY

Optimal success in recording quality was achieved when sf9 cells below passage 25 were transiently transfected in 24-well plates using a 2:4 ratio of µg DNA: µl PolyJet transfection reagent (SignaGen) in unsupplemented Grace's insect media. Cells were replated onto 35 mm dishes or 10 mm glass coverslips 24 hours post-transfection and used for recording for up to 2 weeks post-transfection.

7.3 MOLECULAR BIOLOGY

7.3.1 *DNA Amplification*

Q5 master mix (NEB) was used to amplify portions of DNA from templates using the manufacturers protocols with modification. Touchdown PCR protocols were used in with the annealing temperature is gradually decreased over subsequent cycles. Initially, the annealing temperature is set at 2C above the recommended temperature (NEB Tm Calculator) and stepped down over several cycles. The protocol consists of 2 cycles at +2C, 2 cycles at +1C, and 30 cycles at the suggested annealing temperature.

7.3.2 *Mutagenesis*

To create point mutations or insertion and deletions of up to 6pb, partially overlapping primers were designed such that the nucleotides to be mutated were no less than 8 bp from 3' end and 13 bp from 5'end of primers, with the 5' ends forming the non-overlapping portions, ideally ending in a G or a C. The calculated Tm of the primers were within 3C of each other and above 60C when possible. PCR mutagenesis was performed using pfuUltraII (Fisher) wherein 50 ng of vector template DNA was used in a 50 uL total reaction with 1 uL of the polymerase. The annealing temperature was set to be much lower than the Tm of the primers (usually 50 or 55C), using 68C at the elongation phase instead of the manufacturer recommended 72C for 30 cycles total. The length of elongation was 15-30s per Kb. To degrade template vectors, 2 uL of DpnI (NEB) was added directly to the PCR product, mixed, wrapped in parafilm, and incubated at 37C overnight, spinning down at least once within the first 3 hours.

7.3.3 *Transformation and DNA preparation*

10 uL of the mutagenesis product was used to inoculate 100 uL of GC10 competent cells on ice for 30 minutes. They were then heat shocked at 42C for 45 seconds and returned to ice for 2 minutes, and 75-150 uL was plated onto low-salt LB plates containing Zeocin. Colonies were picked 10-18 hours later and cultured in 5-10 mL low-salt LB containing Zeocin overnight at 37C, shaking 250-300 rpm. When possible, an endonuclease free kit was used to prepare DNA for transfection (E.Z.N.A. Endo-free kit II), otherwise a standard Qiagen or Invitrogen mini prep kit was used according to manufacturer instructions.

7.3.4 *Digestion*

The vector backbone of NavN48KNoGFP-NheI and the linker_GFP PCR product were digested with NdeI (after flag) and XbaI (after c-terminus of Na$_V$Ab) in 80 uL of Cutsmart solution (from concentrate), 3.5 uL of each endnuclease, and 15 ug of vector DNA. For the PCR product, the concentration of the PCR cleanup elution (in molecular biology grade water) was quantified with a nanodrop (1 uL used) to approximate the total DNA mass, and the total remaining volume was used for the digestion as described above.

7.3.5 *Ligation*

The digestion products were run on a 1% agarose gel supplemented with ethidium bromide, and the bands were visualized under IV light and excised. The digestion products were isolated and concentrated by gel purification (for the vector) and pcr cleanup (for linker_GFP). Elutions (in molecular biology grade water) were quantified by measuring the DNA concentration in 1 uL as above. Ligation was then performed using a 1:5 molar ratio of vector to insert and T4 Ligase at 16C for 12-72 hours, ideally in a thermocycler with a lid that is capable of having its heating turned off during the protocol.

7.3.6 *Creation of pIZT/flag_Na$_V$Ab_N49K*

pIZT/V5-His was acquired along with p1 Sf9 cells (InsectSelect Glow Kit, Invitrogen), and flag_Na$_V$Ab was ligated into the multiple cloning site (T4 Ligase, NEB) of pIZT by PCR amplification of the channel DNA from the pfastbacdual vector to create EcoRI and XbaI sites 6 bp from the 3’ and 5’ ends, respectively. Subsequent digestion of the pIZT vector and the PCR product with the above enzymes, purification, and ligation produced the pIZT/flag_Na$_V$Ab vector (see below).

Cells transfected with pIZT/flag_Na$_V$Ab should fluoresce due to the GFP conjugated to the N-terminus of the Zeocin resistance gene, and this fluorescent signal should indicate which cells will have adequate channel expression for recording. The first pIZT plasmid generated did not initially produce enough current for recording, so expression was enhanced by altering the translation initiation site to include a Kozac sequence specifically tailored to give high expression in insect cells lines: GAA TTC ATC AAC ATG (Cavener, 1987; Kozak, 1991).

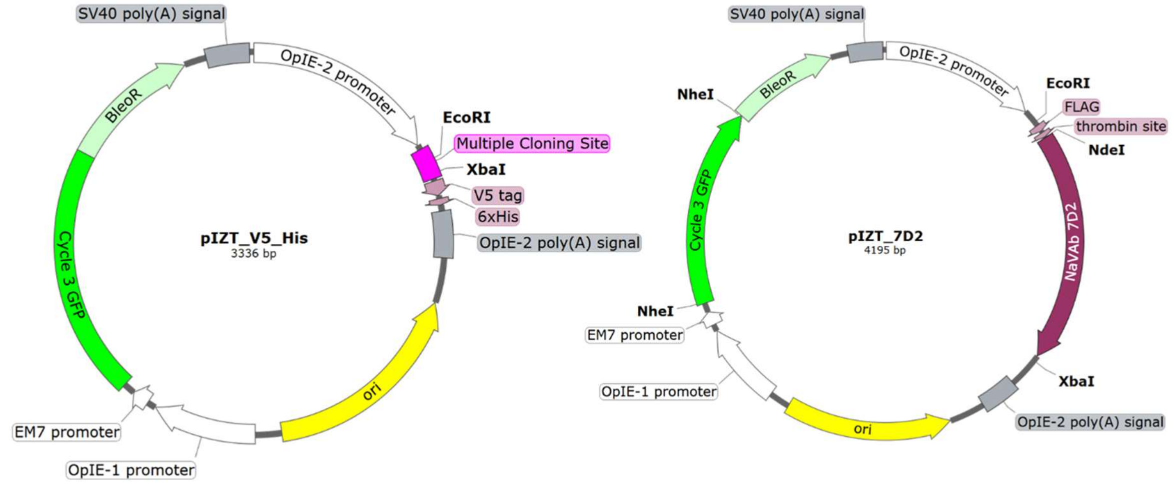

Figure 7.2 Plasmid map of the backbone pIZT/V5_His and pIZT_Na$_V$Ab.

7.3.7 *Creation of pIZT/Na$_V$Ab_linker_GFP and _IRES_GFP*

Expression thereafter was more variable than was conducive to efficient data collection, and this was attributed to the fact that the channel’s expression was under the control of the OPIE2 promoter, while the GFP fluorescence signal was controlled by OPIE1. To create a more predictable system, the vector was modified to move the GFP from its original site to upstream of the channel, connected via a flexible linker or an internal ribosomal reentry site (IRES).

As the GFP in this vector had an NheI cut site directly upstream, its removal was accomplished by mutagenesis to place an additional NheI site between GFP and the Zeocin resistance gene. Excision of the GFP was accomplished by digestion with NheI, followed by gel purification of the backbone vector, and re-ligation to produce pIZT/NavAbN48KNoGFP (see below for instructions). Mutagenesis using partially overlapping primers was used to remove the single remaining NheI site before the Zeocin resistance gene of the resulting vector pIZT/NavAbN48KNoGFP-NheI.

The vector was further modified to contain a GFP with a 3’ linker that would be connected to the C-terminus of the channel. The GFP NheI digestion product was PCR amplified 4 separate times, each adding more bp upstream until it had a linker containing 3’ NdeI+AflII cut sites and a 5’ XbaI site (from reverse primer). The NheI site downstream of GFP was removed during the amplification process, and only NheI site on the plasmid was then found directly upstream of the GFP.

The resulting construct was pIZT/flag_linker_GFPonly. A similar construct was made replacing the linker with an IRES site by digesting pIZT/flag_linker_GFPonly and the IRES insert (ordered as geneblock from IDT) with AflII and NheI, purifying using PCR Cleanup, and ligating with T4 as above to produce pIZT/flag_IRES_GFP

The vectors pIZT/flag_IRES_GFP and pIZT/flag_Linker_GFP were then digested with NdeI/AflII (both placed 6 bp apart between flag and the start of the IRES or linker) along with PCR-amplified Na$_V$Ab_N49K. The digestion products were purified by PCR cleanup, and the channel was ligated into each vector backbone to produce pIZT/Na$_V$Ab_N49K_linker_GFP and pIZT/Na$_V$Ab_N49K_IRES_GFP

7.3.8 *Creation of pIZT/GFP_P2A_Na$_V$Ab*

Neither the IRES site nor the c-terminal GFP worked well in this system. Many small green fluorescent puncta were observed in cells transfected with the C linked GFP, but little current could be measured from them and the fluorescent signal was too dim to be effective. No GFP was observed in cells transfected with the IRES-containing plasmid.

In light of these events, we decided to try a P2A site between the channel and the GFP. This is a self-cleaving peptide that can be placed in between proteins, and upon translation the final proline will be cleaved from the C-terminus of the first protein. In order to construct this, we needed the GFP to be upstream of the channel, so only one amino acid would remain attached to the channel (a proline on the n terminus) and would have little potential effect on channel function. A P2A site from porcine teschovirus-1 (P2A-GSG) was placed between the upstream GFP and the downstream channel, as this was shown to create nearly 1:1 stoichiometry in Sf9 cells (Wang et al., 2015).

To do this, we took advantage of the two SpeI sites flanking Na$_V$Ab and created pIZT/GFPOnly (with no flag-tag) by digesting pIZT/Na$_V$Ab_linker_GFP with SpeI, gel purifying the vector backbone, and religating to create pIZT/Na$_V$Ab_NoGFP. An EcoRI site was then added after the GFP, and the vector was digested with EcoRI and AgeI and purified using PCR cleanup.

Another geneblock was ordered to produce EcoRI_P2A_Flag_NdeI, and after PCR amplification and digestion with EcoRI and NdeI, and PCR purification, the backbone and P2A insert were ligated to produce pIZT/GFP_P2A_Na$_V$Ab

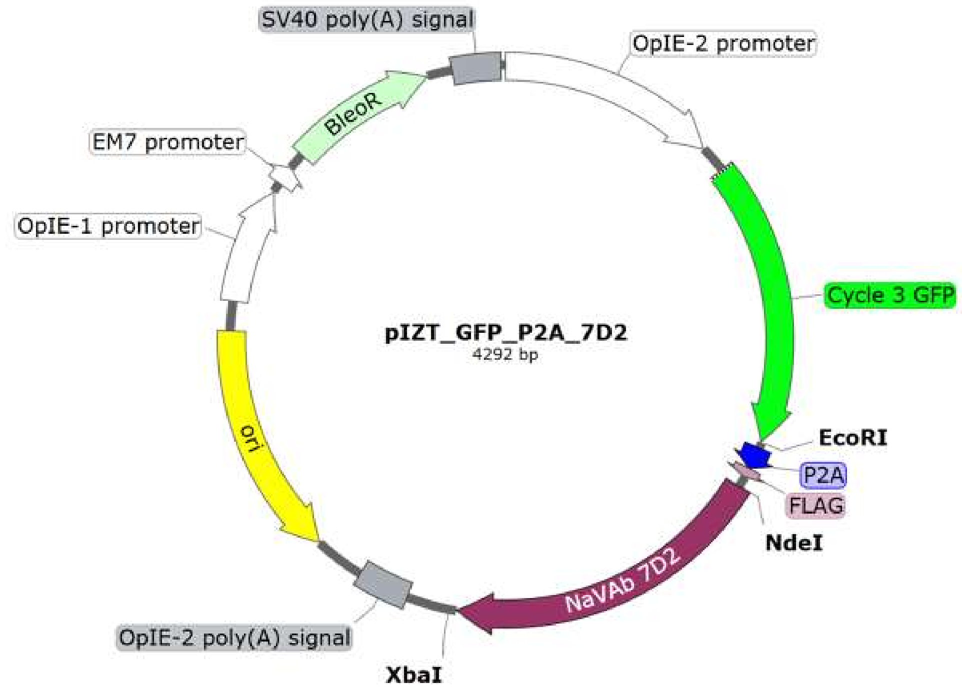

Figure 7.3 Plasmid map of pIZT/GFP_P2A_Na$_V$Ab

7.4 ELECTROPHYSIOLOGICAL DATA ACQUISITION

1.5-3 MΩ glass pipettes were used to patch-clamp fluorescent cells, and currents were recorded via whole-cell voltage clamp (EPC10, Pulse, HEKA), sampled at 250 kHz or 500 kHz, and filtered at 3, 8, or 10 kH. Membrane capacitance ranged from 5-25 pF. Rs was below 10 MΩ, with a 2 µs lag and at least 70% compensation, or else voltage error was kept below 10 mV. A P/4 leak subtraction protocol was used. Standard recording solutions were as follows: Intracellular (in mM); NaCl (35) CsF (105) EGTA (10) HEPES (10). Extracellular solution contained: NaCl (140) $MgCl_2$ (2) $CaCl_2$ (2) HEPES (10). In order to analyze Na$_V$Ab mutants with positively shifted voltage dependence, solutions were designed to result in reversal potentials outside the range of the voltage response. To do this, NMDG-Cl was substituted for NaCl in both solutions at the appropriate concentrations. The pH for both intracellular and extracellular solutions was 7.4, adjusted with CsOH/HCl and NaOH/HCl for solutions that contained no NMDG-Cl, respectively, and NMDG+/HCl for those that did. For gating charge measurements, the intracellular solution contained NMDG-Cl (140) EGTA (10) HEPES (10) $MgCl_2$ (1), and external contained NMDG-Cl (148) HEPES (10) $MgCl_2$ (3). Osmolarity was adjusted with sucrose to match that of the cells' media each day. The measured liquid junction potential was -7 mV for all recordings, and the reported voltages were not adjusted. Na_VAb /N49K, which activates at negative voltages, was studied as previously described (Gamal El-Din et al., 2013). Briefly, Hi5 cells were infected with baculovirus and recordings were made 18-24 hours later. The intracellular solution composition was as above, and the extracellular solution was identical except NaCl concentration was 140 mM, no NMDG was used, and pH was adjusted with NaOH. Current families were generated by holding cells at -150 mV (-120 for Na_VAb/N49K) and stimulating with a series of 50-ms pulses at 10 mV intervals. To determine reversal potential of outward-only current, peak current was elicited by pulsing to an appropriate potential for each construct and decreasing the voltage in 10 mV steps until substantial inward current was seen in the tail currents. The time between the start of the initial voltage step and the subsequent steps was determined for each construct as roughly the time to peak (data not shown). An agar bridge consisting of extracellular solution with 3% Agar was placed between the reference electrode and the bath in experiments utilizing perfusion of extracellular solution containing reducing agents.

7.5 DATA ANALYSIS

Pulse data was analyzed using IGOR Pro (6.37). The 1-5 ms surrounding peak current at each voltage of the current family was averaged and plotted as a function of the stimulus voltage to visualize the current vs voltage (I/V) relationship. When the I/V curves contained only outward current, the reversal potential (Vrev) was determined from the tail currents at peak activation. The instantaneous current of the tail current family was plotted as a function of voltage, fit with a line near 0 mV, and the X intercept was used as Vrev to generate the conductance vs voltage (G/V) curve from the I/V curve by calculating G=I/(Vm-Vrev). The calculated Vrev was near 7 mV for all recordings. Normalized G/V curves were fit with a simple two-state Boltzmann equation $1/(1+\exp(V_{1/2}-Vm)/k)$ in which Vm is the stimulus potential, $V_{1/2}$ is the half-activation voltage, and k is a slope factor. I/V plots of inward currents for Na_VAb/N49K were fit with $(Vm-Vrev)*(Imin/(1+\exp((Vm-V_{1/2})/k))$ to generate the above Boltzmann curve fit to normalized G/V. The rate of activation was calculated by fitting a single exponential $(1+\exp(-(x-x_0)/tau))$ to the rising phase of the exponential growth of the current, and the tau value was divided by one to get the rate of transition. The delay associated with the activation of the channel is represented by the y-intercept of the resulting fit of the rising phase of the current. The x-values are normalized to the $V_{1/2}$ of the activation curve of the specific construct to allow for comparison across a wide range of voltage-dependencies. Q/V curves were generated by integrating underneath the P/N subtracted curve either during the test pulse or after the return to the prepulse voltage. Both methods produced curves with similar parameters, but recovered current was often less noisy. If necessary, due to the issues with clamping large voltage jumps and performing P/N subtraction, the currents were baseline subtracted to the average of the final 2 ms of the pulse or the 2 ms around a cursor placed at location where noise was minimal and decay of current had returned to baseline. This provided a true zero, which was necessary for the integration to be representative of actual charge movement.

BIBLIOGRAPHY

Aggarwal, S.K., and MacKinnon, R. (1996). Contribution of the S4 segment to gating charge in the Shaker potassium channel. Neuron *16*, 1169-1177.

Ahuja, S., Mukund, S., Deng, L., Khakh, K., Chang, E., Ho, H., Shriver, S., Young, C., Lin, S., Johnson, J.P., Jr*., et al.* (2015). Structural basis of Nav1.7 inhibition by an isoform-selective small-molecule antagonist. Science *350*, aac5464.

Almog, M., Barkai, T., Lampert, A., and Korngreen, A. (2018). Voltage-Gated Sodium Channels in Neocortical Pyramidal Neurons Display Cole-Moore Activation Kinetics. Front Cell Neurosci *12*, 187.

Antala, S., Ovchinnikov, S., Kamisetty, H., Baker, D., and Dempski, R.E. (2015). Computation and Functional Studies Provide a Model for the Structure of the Zinc Transporter hZIP4. J Biol Chem *290*, 17796-17805.

Armstrong, C.M. (1981). Sodium channels and gating currents. PhysiolRev *61*, 644-682.

Armstrong, C.M., and Bezanilla, F. (1973). Currents related to movement of the gating particles of the sodium channels. Nature *242*, 459-461.

Armstrong, C.M., and Bezanilla, F. (1977). Inactivation of the sodium channel. II. Gating current experiments. JGenPhysiol *70*, 567-590.

Auld, V.J., Goldin, A.L., Krafte, D.S., Catterall, W.A., Lester, H.A., Davidson, N., and Dunn, R.J. (1990). A neutral amino acid change in segment IIS4 dramatically alters the gating properties of the voltage-dependent sodium channel. Proc Natl Acad Sci USA *87*, 323-327.

Bezanilla, F. (2000). The voltage sensor in voltage-dependent ion channels. Physiol Rev *80*, 555-592.

Bezanilla, F., and Armstrong, C.M. (1977). Inactivation of the sodium channel. I. Sodium current experiments. JGenPhysiol *70*, 549-566.

Bezanilla, F., and Stefani, E. (1994). Voltage-dependent gating of ionic channels. AnnuRevBiophysBiomolStruct *23*, 819-846.

Bezanilla, F., Taylor, R.E., and Fernandez, J.M. (1982). Distribution and kinetics of membrane dielectric polarization. 1. Long- term inactivation of gating currents. J Gen Physiol *79*, 21-40.

Blanchet, J., and Chahine, M. (2007). Accessibility of four arginine residues on the S4 segment of the Bacillus halodurans sodium channel. J Membr Biol *215*, 169-180.

Caldwell, P.C., Hodgkin, A.L., Keynes, R.D., and Shaw, T.L. (1960). The effects of injecting 'energy-rich' phosphate compounds on the active transport of ions in the giant axons of Loligo. J Physiol *152*, 561-590.

Campos, F.V., Chanda, B., Beirão, P.S.L., and Bezanilla, F. (2007a). β-Scorpion Toxin Modifies Gating Transitions in All Four Voltage Sensors of the Sodium Channel. The Journal of General Physiology *130*, 257-268.

Campos, F.V., Chanda, B., Roux, B., and Bezanilla, F. (2007b). Two atomic constraints unambiguously position the S4 segment relative to S1 and S2 segments in the closed state of Shaker K channel. Proc Natl Acad Sci U S A *104*, 7904-7909.

Catterall, W.A. (1984). The molecular basis of neuronal excitability. Science *223*, 653-661.

Catterall, W.A. (1986). Molecular properties of voltage-sensitive sodium channels. AnnuRevBiochem *55*, 953-985.

Catterall, W.A. (2000). From ionic currents to molecular mechanisms: The structure and function of voltage-gated sodium channels. Neuron *26*, 13-25.

Catterall, W.A., Cestele, S., Yarov-Yarovoy, V., Yu, F.H., Konoki, K., and Scheuer, T. (2007). Voltage-gated ion channels and gating modifier toxins. Toxicon *49*, 124-141.

Catterall, W.A., Wisedchaisri, G., and Zheng, N. (2017). The chemical basis for electrical signaling. Nature chemical biology *13*, 455-463.

Cavener, D.R. (1987). Comparison of the consensus sequence flanking translational start sites in Drosophila and vertebrates. Nucleic Acids Res *15*, 1353-1361.

Cestèle, S., Qu, Y., Rogers, J.C., Rochat, H., Scheuer, T., and Catterall, W.A. (1998). Voltage sensor-trapping: Enhanced activation of sodium channels by beta-scorpion toxin bound to the S3-S4 loop in domain II. Neuron *21*, 919-931.

Chanda, B., and Bezanilla, F. (2002). Tracking voltage-dependent conformational changes in skeletal muscle sodium channel during activation. J Gen Physiol *120*, 629-645.

Chowdhury, S., Haehnel, B.M., and Chanda, B. (2014). A self-consistent approach for determining pairwise interactions that underlie channel activation. J Gen Physiol *144*, 441-455.

Clairfeuille, T., Cloake, A., Infield, D.T., Llongueras, J.P., Arthur, C.P., Li, Z.R., Jian, Y., Martin-Eauclaire, M.F., Bougis, P.E., Ciferri, C., *et al.* (2019). Structural basis of alpha-scorpion toxin action on Nav channels. Science *363*.

Cole, K.S., and Moore, J.W. (1960). Potassium ion current in the squid giant axon: dynamic characteristic. Biophys J *1*, 1-14.

Cox, J.J., Reimann, F., Nicholas, A.K., Thornton, G., Roberts, E., Springell, K., Karbani, G., Jafri, H., Mannan, J., Raashid, Y., *et al.* (2006). An SCN9A channelopathy causes congenital inability to experience pain. Nature *444*, 894-898.

Cummins, T.R., Dib-Hajj, S.D., and Waxman, S.G. (2004). Electrophysiological properties of mutant Nav1.7 sodium channels in a painful inherited neuropathy. J Neurosci *24*, 8232-8236.

DeCaen, P.G., Yarov-Yarovoy, V., Sharp, E.M., Scheuer, T., and Catterall, W.A. (2009). Sequential formation of ion pairs during activation of a sodium channel voltage sensor. Proc Natl Acad Sci U S A *106*, 22498-22503.

DeCaen, P.G., Yarov-Yarovoy, V., Zhao, Y., Scheuer, T., and Catterall, W.A. (2008). Disulfide locking a sodium channel voltage sensor reveals ion pair formation during activation. Proc Natl Acad Sci U S A *105*, 15142-15147.

Emery, E.C., Luiz, A.P., and Wood, J.N. (2016). Nav1.7 and other voltage-gated sodium channels as drug targets for pain relief. Expert Opin Ther Targets *20*, 975-983.

Fernández-Mariño, A.I., Harpole, T.J., Oelstrom, K., Delemotte, L., and Chanda, B. (2018). Gating interaction maps reveal a noncanonical electromechanical coupling mode in the Shaker K+ channel. Nature Structural & Molecular Biology *25*, 320-326.

Gamal El-Din, T.M., Lenaeus, M.J., Ramanadane, K., Zheng, N., and Catterall, W.A. (2017). Molecular dissection of multi-phase inactivation of the bacterial sodium channel NavAb. Submitted.

Gamal El-Din, T.M., Martinez, G.Q., Payandeh, J., Scheuer, T., and Catterall, W.A. (2013). A gating charge interaction required for late slow inactivation of the bacterial sodium channel NavAb. J Gen Physiol *142*, 181-190.

George, A.L., Jr. (2005). Inherited disorders of voltage-gated sodium channels. The Journal of clinical investigation *115*, 1990-1999.

Goldschen-Ohm, M.P., Capes, D.L., Oelstrom, K.M., and Chanda, B. (2013). Multiple pore conformations driven by asynchronous movements of voltage sensors in a eukaryotic sodium channel. Nature communications *4*, 1350.

Guy, H.R., and Seetharamulu, P. (1986). Molecular model of the action potential sodium channel. ProcNatlAcadSciUSA *508*, 508-512.

Herzog, R.I., Cummins, T.R., Ghassemi, F., Dib-Hajj, S.D., and Waxman, S.G. (2003). Distinct repriming and closed-state inactivation kinetics of Nav1.6 and Nav1.7 sodium channels in mouse spinal sensory neurons. J Physiol *551*, 741-750.

Hille, B. (2001). Ionic Channels of Excitable Membranes, 3rd Ed (Sunderland, MA: Sinauer Associates Inc.).

Hodgkin, A.L., and Huxley, A.F. (1952a). The components of membrane conductance in the giant axon of Loligo. JPhysiol *116*, 473-496.

Hodgkin, A.L., and Huxley, A.F. (1952b). A quantitative description of membrane current and its application to conduction and excitation in nerve. JPhysiol *117*, 500-544.

Hoshi, T., Zagotta, W.N., and Aldrich, R.W. (1994). Shaker potassium channel gating. I: Transitions near the open state. JGenPhysiol *103*, 249-278.

Irie, K., Haga, Y., Shimomura, T., and Fujiyoshi, Y. (2018). Optimized expression and purification of NavAb provide the structural insight into the voltage dependence. FEBS Lett *592*, 274-283.

Islas, L.D., and Sigworth, F.J. (1999). Voltage sensitivity and gating charge in Shaker and Shab family potassium channels. J Gen Physiol *114*, 723-741.

Jiang, Y., Lee, A., Chen, J., Ruta, V., Cadene, M., Chait, B.T., and MacKinnon, R. (2003a). X-ray structure of a voltage-dependent K^+ channel. Nature *423*, 33-41.

Jiang, Y., Ruta, V., Chen, J., Lee, A., and MacKinnon, R. (2003b). The principle of gating charge movement in a voltage-dependent potassium channel. Nature *423*, 42-48.

Keynes, R.D., and Rojas, E. (1974). Kinetics and steady-state properties of the charged system controlling sodium conductance in the squid giant axon. J Physiol *239*, 393-434.

Kontis, K.J., Rounaghi, A., and Goldin, A.L. (1997). Sodium channel activation gating is affected by substitutions of voltage sensor positive charges in all four domains. JGenPhysiol *110*, 391-401.

Kozak, M. (1991). Structural features in eukaryotic mRNAs that modulate the initiation of translation. JBiolChem *266*, 19867-19870.

Lacroix, J.J., and Bezanilla, F. (2011). Control of a final gating charge transition by a hydrophobic residue in the S2 segment of a K+ channel voltage sensor. Proceedings of the National Academy of Sciences *108*, 6444-6449.

Lacroix, J.J., Hyde, H.C., Campos, F.V., and Bezanilla, F. (2014). Moving gating charges through the gating pore in a Kv channel voltage sensor. Proc Natl Acad Sci U S A *111*, E1950-1959.

Lacroix, J.J., Pless, S.A., Maragliano, L., Campos, F.V., Galpin, J.D., Ahern, C.A., Roux, B., and Bezanilla, F. (2012). Intermediate state trapping of a voltage sensor. J Gen Physiol *140*, 635-652.

Lee, S.Y., Lee, A., Chen, J., and MacKinnon, R. (2005). Structure of the KvAP voltage-dependent K+ channel and its dependence on the lipid membrane. Proc Natl Acad Sci U S A *102*, 15441-15446.

Lenaeus, M.J., Gamal El-Din, T.M., Ing, C., Ramanadane, K., Pomes, R., Zheng, N., and Catterall, W.A. (2017). Structures of closed and open states of a voltage-gated sodium channel. Proc Natl Acad Sci U S A *114*, E3051-E3060.

Long, S.B., Campbell, E.B., and Mackinnon, R. (2005). Crystal structure of a mammalian voltage-dependent Shaker family K^+ channel. Science *309*, 897-903.

Lopez, G.A., Jan, Y.N., and Jan, L.Y. (1991). Hydrophobic substitution mutations in the S4 sequence alter voltage-dependent gating in Shaker K+ channels. Neuron *7*, 327-336.

Mannuzzu, L.M., and Isacoff, E.Y. (2000). Independence and cooperativity in rearrangements of a potassium channel voltage sensor revealed by single subunit fluorescence. J Gen Physiol *115*, 257-268.

McCormack, K., Santos, S., Chapman, M.L., Krafte, D.S., Marron, B.E., West, C.W., Krambis, M.J., Antonio, B.M., Zellmer, S.G., Printzenhoff, D.*, et al.* (2013). Voltage sensor interaction site for selective small molecule inhibitors of voltage-gated sodium channels. Proc Natl Acad Sci U S A *110*, E2724-2732.

Nassar, M.A., Stirling, L.C., Forlani, G., Baker, M.D., Matthews, E.A., Dickenson, A.H., and Wood, J.N. (2004). Nociceptor-specific gene deletion reveals a major role for Nav1.7 (PN1) in acute and inflammatory pain. Proc Natl Acad Sci U S A *101*, 12706-12711.

Noda, M., Shimizu, S., Tanabe, T., Takai, T., Kayano, T., Ikeda, T., Takahashi, H., Nakayama, H., Kanaoka, Y., Minamino, N.*, et al.* (1984). Primary structure of Electrophorus electricus sodium channel deduced from cDNA sequence. Nature *312*, 121-127.

Olivera, B.M., Rivier, J., Scott, J.K., Hillyard, D.R., and Cruz, L.J. (1991). Conotoxins. JBiolChem *266*, 22067-22070.

Palovcak, E., Delemotte, L., Klein, M.L., and Carnevale, V. (2014). Evolutionary imprint of activation: the design principles of VSDs. J Gen Physiol *143*, 145-156.

Papazian, D.M., Shao, X.M., Seoh, S.A., Mock, A.F., Huang, Y., and Wainstock, D.H. (1995). Electrostatic interactions of S4 voltage sensor in *Shaker* K^+ channel. Neuron *14*, 1293-1301.

Pavlov, E., Bladen, C., Winkfein, R., Diao, C., Dhaliwal, P., and French, R.J. (2005). The pore, not cytoplasmic domains, underlies inactivation in a prokaryotic sodium channel. Biophys J *89*, 232-242.

Payandeh, J., Gamal El-Din, T.M., Scheuer, T., Zheng, N., and Catterall, W.A. (2012). Crystal structure of a voltage-gated sodium channel in two potentially inactivated states. Nature *486* 135-139.

Payandeh, J., and Minor, D.L., Jr. (2015). Bacterial voltage-gated sodium channels (BacNavs) from the soil, sea, and salt lakes enlighten molecular mechanisms of electrical signaling and pharmacology in the brain and heart. J Mol Biol *427*, 3-30.

Payandeh, J., Scheuer, T., Zheng, N., and Catterall, W.A. (2011). The crystal structure of a voltage-gated sodium channel. Nature *475*, 353-358.

Perozo, E., Santacruz-Toloza, L., Stefani, E., Bezanilla, F., and Papazian, D.M. (1994). S4 mutations alter gating currents of Shaker K channels. BiophysJ *66*, 345-354.

Perry, M.D., Wong, S., Ng, C.A., and Vandenberg, J.I. (2013). Hydrophobic interactions between the voltage sensor and pore mediate inactivation in Kv11.1 channels. J Gen Physiol *142*, 275-288.

Poveda, J.A., Giudici, A.M., Renart, M.L., Molina, M.L., Montoya, E., Fernandez-Carvajal, A., Fernandez-Ballester, G., Encinar, J.A., and Gonzalez-Ros, J.M. (2014). Lipid modulation of ion channels through specific binding sites. Biochim Biophys Acta *1838*, 1560-1567.

Rajamani, R., Wu, S., Rodrigo, I., Gao, M., Low, S., Megson, L., Wensel, D., Pieschl, R.L., Post-Munson, D.J., Watson, J.*, et al.* (2017). A Functional NaV1.7-NaVAb Chimera with a Reconstituted High-Affinity ProTx-II Binding Site. Molecular Pharmacology *92*, 310-317.

Ramírez-SanJuan, G.R., Minzoni, A.A., and Islas, L.D. (2013). Effects of electrical polarization on the opening rate constant of a voltage-gated ion channel. Physical Review E *88*.

Rogers, J.C., Qu, Y., Tanada, T.N., Scheuer, T., and Catterall, W.A. (1996). Molecular determinants of high affinity binding of alpha-scorpion toxin and sea anemone toxin in the S3-S4 extracellular loop in domain IV of the Na^+ channel alpha subunit. JBiolChem *271*, 15950-15962.

Safo, P., Rosenbaum, T., Shcherbatko, A., Choi, D.Y., Han, E., Toledo-Aral, J.J., Olivera, B.M., Brehm, P., and Mandel, G. (2000). Distinction among neuronal subtypes of voltage-activated sodium channels by mu-conotoxin PIIIA. J Neurosci *20*, 76-80.

Schmalhofer, W.A., Calhoun, J., Burrows, R., Bailey, T., Kohler, M.G., Weinglass, A.B., Kaczorowski, G.J., Garcia, M.L., Koltzenburg, M., and Priest, B.T. (2008). ProTx-II, a selective inhibitor of NaV1.7 sodium channels, blocks action potential propagation in nociceptors. Mol Pharmacol *74*, 1476-1484.

Schoppa, N.E., and Sigworth, F.J. (1998). Activation of shaker potassium channels. I. Characterization of voltage-dependent transitions. J Gen Physiol *111*, 271-294.

Serrano, L., Horovitz, A., Avron, B., Bycroft, M., and Fersht, A.R. (1990). Estimating the contribution of engineered surface electrostatic interactions to protein stability by using double-mutant cycles. Biochemistry *29*, 9343-9352.

Shen, H., Zhou, Q., Pan, X., Li, Z., Wu, J., and Yan, N. (2017). Structure of a eukaryotic voltage-gated sodium channel at near-atomic resolution. Science.

Sigworth, F.J. (1995). Charge movement in the sodium channel. JGenPhysiol *106*, 1047-1051.

Sokolov, S., Kraus, R.L., Scheuer, T., and Catterall, W.A. (2008). Inhibition of sodium channel gating by trapping the domain II voltage sensor with protoxin II. Mol Pharmacol *73*, 1020-1028.

Stuhmer, W., Conti, F., Suzuki, H., Wang, X., Noda, M., Yahadi, N., Kubo, H., and Numa, S. (1989). Structural parts involved in activation and inactivation of the sodium channel. Nature *339*, 597-603.

Takahashi, M., Seagar, M.J., Jones, J.F., Reber, B.F., and Catterall, W.A. (1987). Subunit structure of dihydropyridine-sensitive calcium channels from skeletal muscle. Proc Natl Acad Sci USA *84*, 5478-5482.

Tanabe, T., Takeshima, H., Mikami, A., Flockerzi, V., Takahashi, H., Kangawa, K., Kojima, M., Matsuo, H., Hirose, T., and Numa, S. (1987). Primary structure of the receptor for calcium channel blockers from skeletal muscle. Nature *328*, 313-318.

Tang, Z., Chen, Z., Tang, B., and Jiang, H. (2015). Primary erythromelalgia: a review. Orphanet J Rare Dis *10*, 127.

Tao, X., Lee, A., Limapichat, W., Dougherty, D.A., and MacKinnon, R. (2010). A gating charge transfer center in voltage sensors. Science *328*, 67-73.

Timpe, L.C., Jan, Y.N., and Jan, L.Y. (1988). Four cDNA clones from the Shaker locus of Drosophila induce kinetically distinct A-type potassium currents in Xenopus oocytes. Neuron *1*, 659-667.

Trimmer, J.S., and Agnew, W.S. (1989). Molecular diversity of voltage-sensitive Na channels. AnnuRevPhysiol *51*, 401-418.

Wang, Y., Wang, F., Wang, R., Zhao, P., and Xia, Q. (2015). 2A self-cleaving peptide-based multi-gene expression system in the silkworm Bombyx mori. Sci Rep *5*, 16273.

Wisedchaisri, G., Tonggu, L., McCord, E., Gamal El-Din, T.M., Wang, L., Zheng, N., and Catterall, W.A. (2019). Resting-State Structure and Gating Mechanism of a Voltage-Gated Sodium Channel. Cell *178*, 993-1003 e1012.

Wu, J., Yan, Z., Li, Z., Qian, X., Lu, S., Dong, M., Zhou, Q., and Yan, N. (2016). Structure of the voltage-gated calcium channel Ca$_V$1.1 at 3.6 A resolution. Nature *537*, 191-196.

Xu, H., Li, T., Rohou, A., Arthur, C.P., Tzakoniati, F., Wong, E., Estevez, A., Kugel, C., Franke, Y., Chen, J., *et al.* (2019). Structural Basis of Nav1.7 Inhibition by a Gating-Modifier Spider Toxin. Cell *176*, 702-715.e714.

Yang, N., George, A.L., Jr., and Horn, R. (1996). Molecular basis of charge movement in voltage-gated sodium channels. Neuron *16*, 113-122.

Yang, N., George, A.L., Jr., and Horn, R. (1997). Probing the outer vestibule of a sodium channel voltage sensor. Biophys J *73*, 2260-2268.

Yang, Y., Wang, Y., Li, S., Xu, Z., Li, H., Ma, L., Fan, J., Bu, D., Liu, B., Fan, Z., *et al.* (2004). Mutations in SCN9A, encoding a sodium channel alpha subunit, in patients with primary erythermalgia. J Med Genet *41*, 171-174.

Yarov-Yarovoy, V., Decaen, P.G., Westenbroek, R.E., Pan, C.Y., Scheuer, T., Baker, D., and Catterall, W.A. (2012). Structural basis for gating charge movement in the voltage sensor of a sodium channel. Proc Natl Acad Sci USA *109* E93-E102.

Zagotta, W.N., and Aldrich, R.W. (1990). Voltage-dependent gating of Shaker A-type potassium channels in Drosophila muscle. JGenPhysiol *95*, 29-60.

Zagotta, W.N., Hoshi, T., and Aldrich, R.W. (1989). Gating of single Shaker potassium channels in Drosophila muscle and in Xenopus oocytes injected with Shaker mRNA. ProcNatlAcadSciUSA *86*, 7243-7247.

Zagotta, W.N., Hoshi, T., and Aldrich, R.W. (1994a). Shaker potassium channel gating. III: Evaluation of kinetic models for activation. JGenPhysiol *103*, 321-362.

Zagotta, W.N., Hoshi, T., Dittman, J., and Aldrich, R.W. (1994b). Shaker potassium channel gating. II: Transitions in the activation pathway. JGenPhysiol *103*, 279-319.

Zakon, H.H. (2012). Adaptive evolution of voltage-gated sodium channels: The first 800 million years. Proc Natl Acad Sci U S A.

APPENDIX A

Plasmid Maps of pIZT/GFP P2A Na$_V$Ab Intermediate Constructs

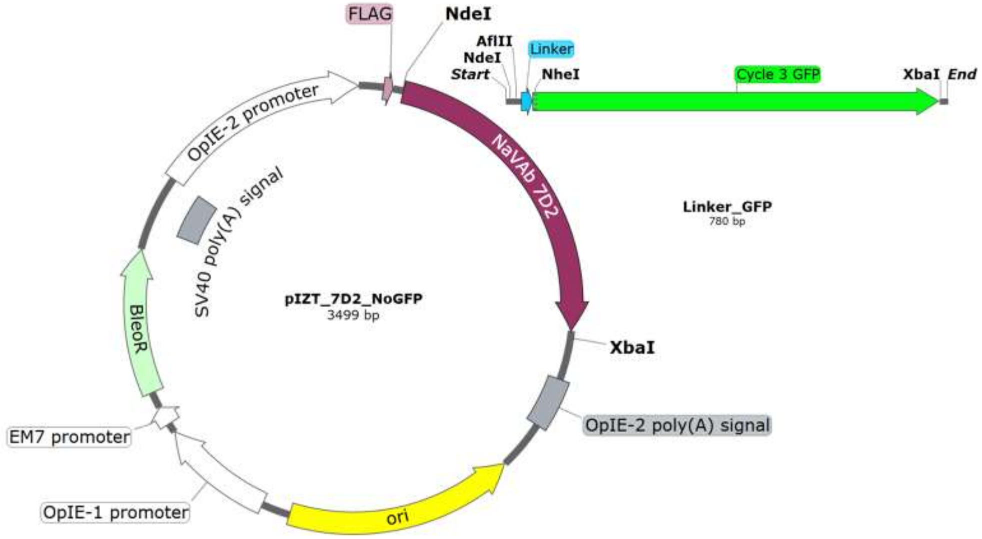

Figure A. 1 Map of pIZT/Na$_V$ab_NoGFP and the linker-GFP insert.

GFP was initially fused to the antibiotic resistance gene BleoR, and its excision produced a plasmid that when transfected whose expression of the channel would remain unchanged, but identification of transfected cells by fluorescence would not be possible. The GFP was amplified from the original pIZT/V5-His template in four successive iterations to incorporate a flexible linker on the n-terminus of GFP found in pVL/GFP: SGAAAAGGS. The final insert and pIZT/Na$_V$Ab_NoGFP were digested with NdeI and XbaI and ligated to replace Na$_V$Ab with the linker-GFP insert, producing a flag tagged GFP with a flexible n-terminus.

Table 9 - Amplification of linker-GFP

Iteration	Direction	Sequence	Tm (°C)	Anneal (°C)
1	Forward	CCGGAGGCAGCCAGAAGGCTAGCAAAGGAGAAG	53 / 75	63 / 70

1	Reverse	GAGCACTCTAGATTATTTGTAGAGCTC ATCCATGCCATGTGTAATCCCAG	60 / 74	
2	Forward	CTGCTGGTTCTCAAAAGATGGCTAG	63/68	58 / 67
2	Reverse	TCTTCTCCTTTGCTAGCCTTCTGGC	57 / 68	
3	Forward	GCTTAAGAATAGTGGTGCTGGTTCTCAAAAG	58 / 68	58 / 67
3	Reverse	TCTTCTCCTTTGCTAGCCTTCTGGC	50 / 69	
4	Forward	AGAGTCCATATGCTTAAGAATAGTGGTGCTG	60 / 69	61 / 67
4	Reverse	TCTTCTCCTTTGCTAGCCTTCTGGC	50 / 69	

*Tm of the overlapping regions of the initial priming region followed by a “/” and then the Tm of the full primer binding. Annealing uses the same denotation for PCR reactions. Each reaction protocol had 34 cycles, with 1-4 using annealing temp 1 and the final 30 using annealing temp 2. Annealing time was 10 seconds with a 15 second extension at 72 °C.

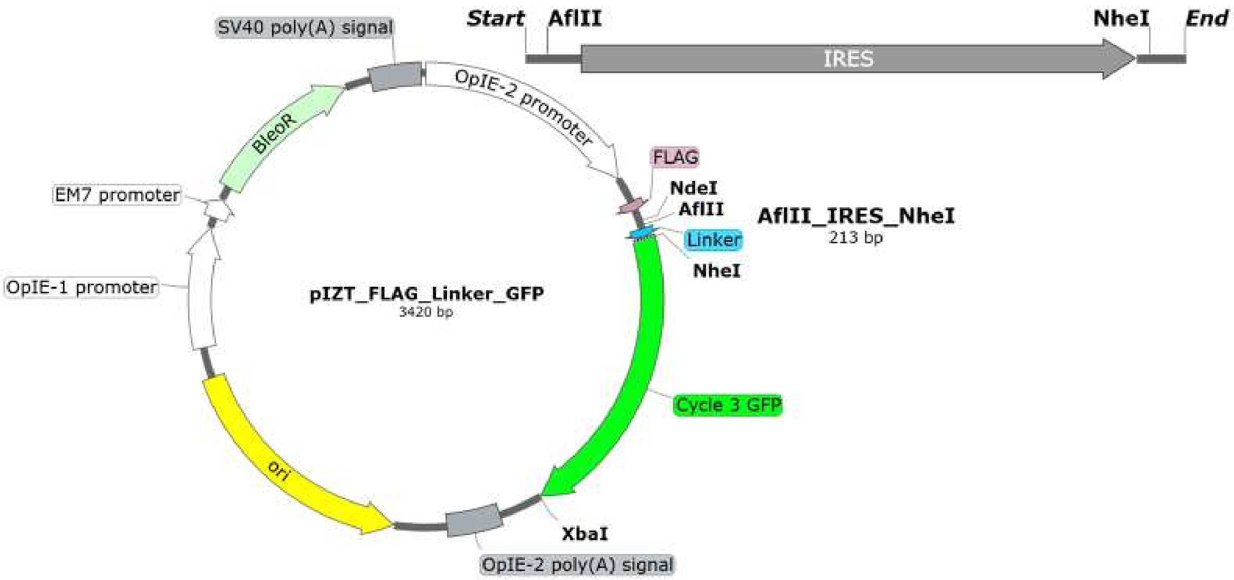

Figure A. 2 Plasmid map of pIZT/flag_linker_GFP and the IRES insert

This was the product of the digestion and ligation described in figure 0.1. To the right is the IRES insert (synthesized). With digestion by AflII and NheI, the IRES was inserted in the place of the linker between the start of GFP and the flag tag to produce pIZT/flag_IRES_GFP. Insertion of the channel could then occur in both constructs by digestion and ligation using the NdeI and AflII cut sites to create pIZT/Na$_V$Ab_linker_GFP and pIZT/Na$_V$Ab_IRES_GFP.

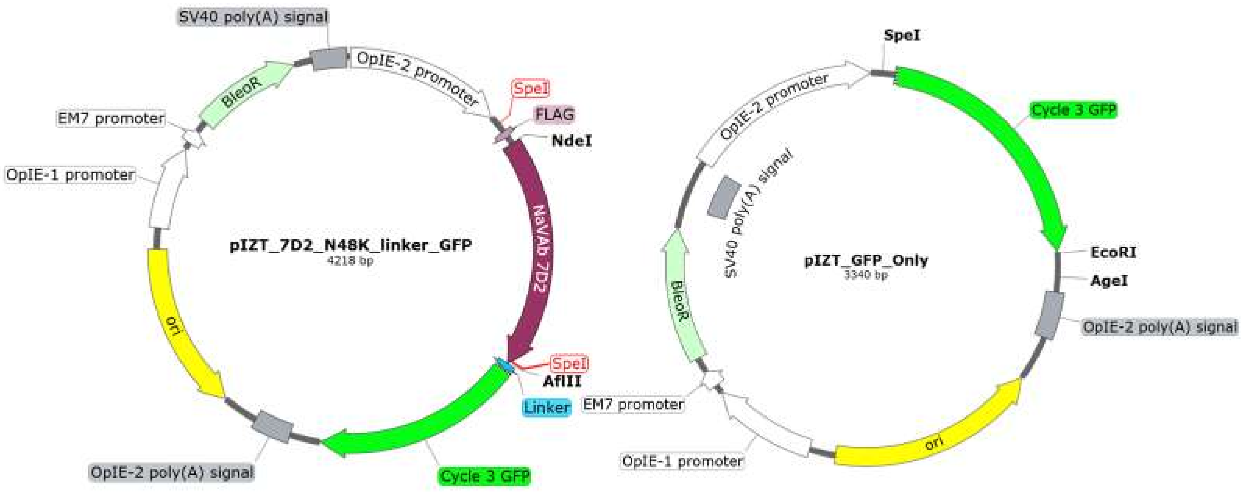

Figure A. 3 Maps of pIZT/Na$_V$Ab_linker_GFP and pIZT/GFP_Only

The construct on the right, pIZT/GFP_Only, was created by excising Na$_V$Ab using flanking SpeI cut sites and re-ligating the backbone. The GFP is not conjugated to a flag tag in this construct. This construct could then be digested with EcoRI and AgeI to reintroduce Na$_V$Ab on the c-terminus of GFP and produce pIZT/GFP_Flag_Na$_V$Ab.

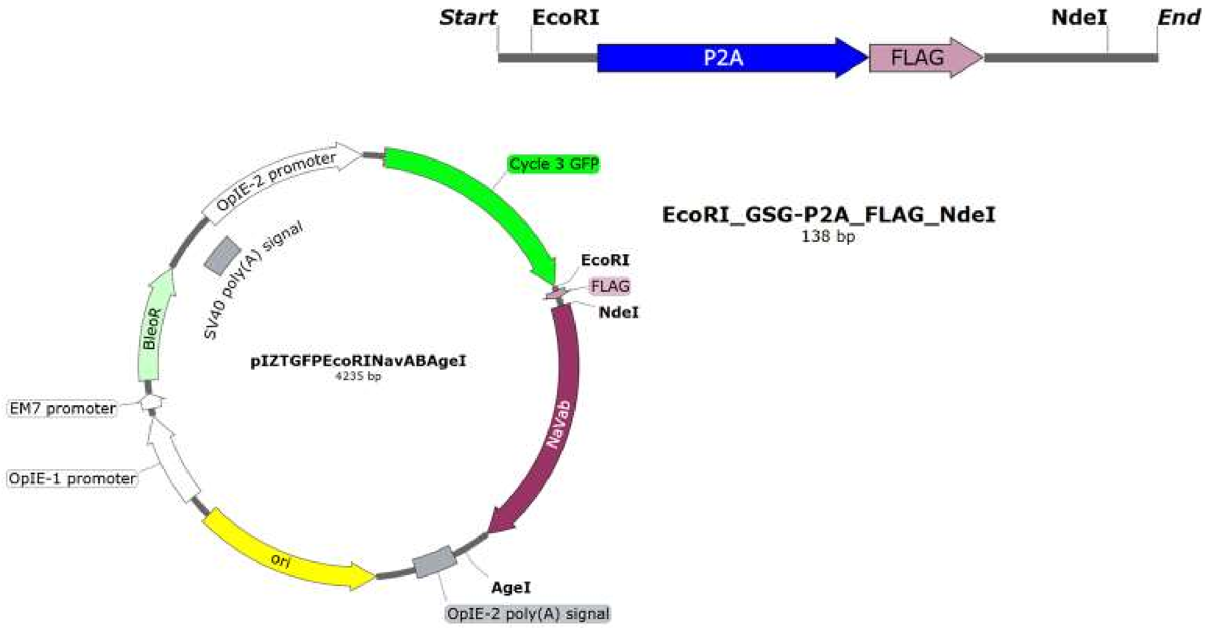

Figure A. 4 Map of pIZT/GFP_Flag_Na$_V$Ab and the P2A-flag insert

The plasmid on the left, pIZT/GFP_Flag_Na$_V$ab expresses a channel that is covalently linked to the c-terminus of GFP, separated by a flag tag. Insertion of P2A was accomplished by digestion of the P2A-flag instert (synthesized) with EcoRI and NdeI. The resulting construct, pIZT/GFP_P2A_Na$_V$Ab was used for all studies beginning in September of 2017.

VITA

Eedann was born and raised in Brenham, Texas, where she excelled in academics and the performing arts. She left the small pond of her high school at 16 to attend the Texas Academy of Mathematics and Science, a selective residential program based at the University of North Texas where she received her diploma after two years of university coursework. She began her lab training during those two summers in the immunology lab of Tonyia Eaves-Pyles at the University of Texas Medical Branch in Galveston as part of the Summer Undergraduate Research Program there.

She received Bachelor of Science degrees in both Biology and Psychology from the University of Texas at Austin in 2010. During her undergraduate and postgraduate time there, she worked evenings and weekends as a technician and stage manager at a local theatre, Austin Playhouse, where she was fortunate to find a supportive community who guided her towards a greater understanding of leadership, project planning, and the satisfaction of a job well done. After graduation, she worked as a technician for two years in the lab of Dan Johnston at the Center for Learning and Memory at UT, where she learned the fundamentals of electrophysiology before joining the University of Washington Pharmacology graduate program in 2013. She joined the Catterall lab in 2014 to study the structure-function relationship in sodium channels.

During her time at the UW, she served as a student representative for the department, helping to coordinate student involvement in graduate admissions and the search for a new Chair. Afterwards, she worked to ensure that the students remained involved in the transition process, and she helped to create plans for moving the department forward in the future. Outside of the university, she was an organizer and stage manager for the Seattle March for Science in both 2017 and 2018, where she strove to provide a platform to amplify marginalized voices in the broader scientific community as well as bring influential politicians to Seattle to speak about the importance of science-based policies in government.